



저작자표시-비영리-변경금지 2.0 대한민국

이용자는 아래의 조건을 따르는 경우에 한하여 자유롭게

- 이 저작물을 복제, 배포, 전송, 전시, 공연 및 방송할 수 있습니다.

다음과 같은 조건을 따라야 합니다:



저작자표시. 귀하는 원저작자를 표시하여야 합니다.



비영리. 귀하는 이 저작물을 영리 목적으로 이용할 수 없습니다.



변경금지. 귀하는 이 저작물을 개작, 변형 또는 가공할 수 없습니다.

- 귀하는, 이 저작물의 재이용이나 배포의 경우, 이 저작물에 적용된 이용허락조건을 명확하게 나타내어야 합니다.
- 저작권자로부터 별도의 허가를 받으면 이러한 조건들은 적용되지 않습니다.

저작권법에 따른 이용자의 권리는 위의 내용에 의하여 영향을 받지 않습니다.

이것은 [이용허락규약\(Legal Code\)](#)을 이해하기 쉽게 요약한 것입니다.

[Disclaimer](#)

공학박사 학위논문

**Improvement of charge injection  
and balance in inverted bottom-  
emission organic light-emitting  
diodes**

역구조 배면발광 유기발광다이오드의  
전하 주입 및 균형 향상

2013년 2월

서울대학교 대학원

공과대학 전기컴퓨터공학부

이 현 구

# Improvement of charge injection and balance in inverted bottom- emission organic light-emitting diodes

지도교수 이 창 희

이 논문을 공학박사 학위논문으로 제출함

2013 년 2 월

서울대학교 대학원

공과대학 전기컴퓨터공학부

이 현 구

이현구의 박사 학위논문을 인준함

2013 년 2 월

위 원 장 \_\_\_\_\_ (인)

부위원장 \_\_\_\_\_ (인)

위 원 \_\_\_\_\_ (인)

위 원 \_\_\_\_\_ (인)

위 원 \_\_\_\_\_ (인)

## **Abstract**

# **Improvement of charge injection and balance in inverted bottom- emission organic light-emitting diodes**

Hyunkoo Lee

School of Electrical Engineering and Computer Science

The Graduate School

Seoul National University

In this thesis, we have investigated the electrical and optical properties of solution-processed zinc oxide (ZnO) and tin dioxide (SnO<sub>2</sub>) nanoparticles (NPs) layers, and the performances of the inverted bottom-emission phosphorescent OLEDs by using these metal oxide NPs layers as electron injection layers (EILs). These metal oxide NPs layers can be simply deposited by using a spin-coating method without additional treatments and they are transparent in visible spectral region. The devices with the metal oxide NPs layers show improved performances compared with the device without the metal oxide NPs layer. The device with the ZnO NPs layer exhibits better

performance than the devices with the SnO<sub>2</sub> NPs layer or the ZnO layer obtained from sol-gel method, due to proper energy level of the ZnO NPs layer for electron injection and higher electron mobility. We estimated the performances of the devices with different thicknesses of metal oxide NPs layers and electron transport layers (ETLs), and with electron transport materials with different lowest-unoccupied-molecular-orbital (LUMO) energy levels. In addition, we have estimated angular dependence of electroluminescence emitted from the devices with the metal oxide NPs layers and found that all devices show a Lambertian emission profile.

Next, we have developed *p*-type doped hole transport layer (HTL) using molybdenum trioxide (MoO<sub>3</sub>) doped di-[4-(*N,N*-ditolyl-amino)-phenyl]cyclohexane (TAPC) layer. We have investigated the electrical and optical properties of MoO<sub>3</sub> doped TAPC layer with different MoO<sub>3</sub> doping concentrations. By applying this *p*-type doped TAPC layer to white OLEDs, we reduce the driving voltage and improve the luminous power efficiency of the device. Furthermore, we have studied the relationship between the hole conductivity of HTL and the performances in the inverted bottom-emission OLEDs. For various hole conductivities of HTL, MoO<sub>3</sub> doped TAPC (high conductivity), undoped TAPC (reference), and 2,9-dimethyl-4,7-diphenyl-1,10-phenanthroline (BCP) doped TAPC (low conductivity) layers were used as HTLs. Inverted bottom-emission white phosphorescent OLEDs with three colors of red, green, and blue are fabricated using these various HTLs. The device with MoO<sub>3</sub> doped TAPC layer shows low driving voltage but low efficiency, whereas the device with BCP doped TAPC layer shows high

efficiency but high driving voltage. The device with BCP doped TAPC layer exhibits the highest external quantum efficiency (EQE) without other optical light extraction techniques or *n*-type doping method in reported value of inverted white OLEDs. This result indicates that electron-hole balance is very important for high efficiency and enhanced electron injection is required for high-performance inverted structure OLEDs.

Finally, we have investigated performance of green and blue OLEDs with common red layers (CRLs). The highest-unoccupied-molecular-orbital (HOMO) energy level differences between hosts and red dye affect the performance of devices. The driving voltages of devices with CRLs are similar or increases compared with those of the devices without CRLs as the HOMO energy level differences are changed, but the efficiencies and the colors of the devices are rarely changed regardless of the insertion of CRLs. As the HOMO energy level difference between hosts and red dye is small, the change of the current and the driving voltage is small. Moreover, we have also fabricated full-color inverted bottom-emission OLEDs employing CRLs. The tendencies of electrical and optical characteristics of the inverted structure device are similar to those of the conventional structure device. The insertion of CRL especially improves the quantum efficiency of the inverted structure device due to enhanced electron-hole balance.

In conclusion, we improved electron and hole injection by using metal oxide NPs as an EIL and *p*-doped HTL, respectively. Enhanced charge injection reduces driving voltage and increases quantum efficiency of the inverted bottom-emission OLEDs. We also found that control of the HTL

conductivity can improve electron-hole balance, resulting in enhanced efficiency of the device. We increased the EQE of the inverted bottom-emission OLEDs using CRLs. In addition, insertion of proper CRL can reduce fabrication cost and TAKT time without performance change in OLEDs. We believe that the fabrication methods and device structures developed in this thesis are helpful for realizing efficient and low-cost optoelectronic devices.

**Keywords: organic light-emitting diodes, OLED, inverted structure, nanoparticle, p-type doping, common red layer**

**Student Number: 2009-30207**

# Contents

<b>Chapter 1. Introduction</b> .....	1
<b>1.1 Organic Light-Emitting Diodes</b> .....	1
<b>1.2 Inverted Structure OLEDs</b> .....	7
<b>1.2.1 Inverted top-emission OLEDs</b> .....	8
<b>1.2.2 Inverted bottom-emission OLEDs</b> .....	8
<b>1.2.3 Inverted transparent OLEDs</b> .....	11
<b>1.3 Outline of Thesis</b> .....	12
<b>Chapter 2. Experimental Methods</b> .....	14
<b>2.1 Materials</b> .....	14
<b>2.1.1 Preparation of ZnO nanoparticles and precursor solution</b> ...	14
<b>2.1.2 Preparation of other materials</b> .....	15
<b>2.1.3 Chemical structures of organic materials</b> .....	16
<b>2.2 Device Fabrication and Characterization Methods</b> .....	19
<b>2.2.1 Device fabrication</b> .....	19
<b>2.2.2 Current-voltage-luminance measurement</b> .....	20
<b>2.2.3 Electroluminescence efficiency calculation</b> .....	24
<b>2.2.4 Angular dependent electroluminescence measurement</b> .....	25

2.2.5	Other characterization methods .....	26
<b>Chapter 3. Inverted Bottom-Emission OLEDs Using</b>		
	<b>Metal Oxide Nanoparticles .....</b>	<b>28</b>
<b>3.1</b>	<b>Properties of Metal Oxide Nanoparticles .....</b>	<b>28</b>
3.1.1	Optical properties of metal oxide nanoparticles .....	28
3.1.2	Electrical properties of metal oxide nanoparticles .....	30
3.1.3	Other properties of metal oxide nanoparticles .....	31
<b>3.2</b>	<b>Inverted Bottom-Emission OLEDs with ZnO Nanoparticles</b> .....	<b>32</b>
3.2.1	Device characteristics depending on ZnO nanoparticles thickness .....	32
3.2.2	Device characteristics depending on ETL thickness .....	39
3.2.3	Device characteristics depending on electron transport material .....	41
3.2.4	Device characteristics depending on types of ZnO .....	43
3.2.5	Angular dependence of the EL spectra in the inverted bottom- emission OLEDs using ZnO nanoparticles .....	49
<b>3.3</b>	<b>Inverted Bottom-Emission OLEDs with SnO<sub>2</sub></b> <b>Nanoparticles.....</b>	<b>51</b>

3.3.1	Device characteristics depending on SnO <sub>2</sub> nanoparticles thickness .....	51
3.3.2	Surface morphology and energy level of SnO <sub>2</sub> NPs layer .....	55
<b>Chapter 4. OLEDs with P-type Doped Hole Transport Layer .....</b>		
	<b>Layer .....</b>	<b>59</b>
4.1	White OLEDs using P-type Doped HTL.....	59
4.1.1	Optical property of MoO <sub>3</sub> doped TAPC layer .....	60
4.1.2	Electrical property of MoO <sub>3</sub> doped TAPC layer .....	61
4.1.3	Phosphorescent white OLEDs using p-type doped HTL .....	64
4.2	Inverted Bottom-Emission White OLEDs Using HTLs with Different Hole Conductivities .....	73
4.2.1	Control of hole conductivity by using doped HTLs .....	73
4.2.2	Inverted bottom-emission white phosphorescent OLEDs using HTLs with different hole conductivities .....	75
<b>Chapter 5 OLEDs with a Common Red Layer .....</b>		
5.1	Full-Color OLEDs with CRLs .....	84
5.1.1	Red phosphorescent OLEDs with different hosts and HTLs	87
5.1.2	Green phosphorescent OLEDs with different HTLs .....	91
5.1.3	Blue phosphorescent OLEDs with different HTLs .....	99

<b>5.2 Full-Color Inverted Bottom-Emission OLEDs with CRLs</b>	107
<b>5.2.1 Inverted bottom-emission red phosphorescent OLEDs with different hosts and HTLs</b>	109
<b>5.2.2 Inverted bottom-emission green phosphorescent OLEDs with different HTLs</b>	113
<b>5.2.3 Inverted bottom-emission blue phosphorescent OLEDs with different HTLs</b>	118
<b>Chapter 6. Conclusion</b>	126
<b>Bibliography</b>	128
<b>Publication</b>	137
<b>초    록</b>	145

## List of Tables

Table 1.1 The status of OLED emitter materials.....	6
Table 4.1 Performance of the phosphorescent white OLEDs with different MoO <sub>3</sub> doping concentrations .....	68
Table 5.1 Performances of devices with different CRLs.....	106
Table 5.2 Performances of inverted structure devices with different CRLs.	125

## List of Figures

Figure 1.1	The main applications of OLEDs. ....	2
Figure 1.2	Schematic of the pixel circuits connected with (a) the conventional structure OLED and (b) the inverted structure OLED.....	8
Figure 2.1	Chemical structures of di-[4-(N,N-ditolyl-amino)-phenyl]cyclohexane (TAPC) and N,N'-di(1-naphthyl)-N,N'-diphenylbenzidine ( $\alpha$ -NPD) as hole transport materials and 2,9-dimethyl-4,7-diphenyl-1,10-phenanthroline (BCP), tris[2,4,6-trimethyl-3-(pyridine-3-yl)phenyl]borane (3TPYMB), and 1,3,5-tri[(3-pyridyl)-phen-3-yl]benzene (TmPyPB) as electron transport materials. ....	16
Figure 2.2	Chemical structures of 4,4'-bis(carbazol-9-yl)biphenyl (CBP), 2,7-bis(carbazol-9-yl)-9,9-spirobifluorene (Spiro-2CBP), 1,3-bis(carbazol-9-yl)benzene (mCP), and 3,6-bis-biphenyl-4-yl-9-[1,1',4,1'']terphenyl-4-yl-9H-carbazole (BBTC) as phosphorescent host materials. ....	17
Figure 2.3	Chemical structures of phosphorescent dopant materials which are bis(3,5-difluoro-2-(2-pyridyl)phenyl-(2-carboxypyridyl)iridium(III) (FIrpic) for blue emitting, tris(2-phenylpyridine)iridium(III) (Ir(ppy) <sub>3</sub> ) and bis(2-phenylpyridine)(acetylacetonate)iridium(III) (Ir(ppy) <sub>2</sub> (acac))	

	for green emitting, bis(2-phenylbenzothiazolato)(acetylacetonate)iridium(III) ( $\text{Ir}(\text{BT})_2(\text{acac})$ ) for orange emitting, and bis(1-phenylisoquinoline)(acetylacetonate)iridium(III) ( $\text{Ir}(\text{piq})_2(\text{acac})$ ) for red emitting.....	18
Figure 2.4	A schematic of the inverted OLEDs fabrication process .....	20
Figure 2.5	Schematic diagrams for the measurement of (a) I-V-L characteristics and (b) EL spectra .....	21
Figure 2.6	The CIE standard observer color matching functions and (b) the CIE 1931 color space chromaticity diagram. The outer curved boundary is the spectral locus, with wavelengths shown in nanometers.....	23
Figure 2.7	A Schematic diagrams of the angular dependent EL measurement set up.....	25
Figure 3.1	Optical absorption spectra of ZnO and SnO <sub>2</sub> NPs films. Inset: Photographs of ZnO and SnO <sub>2</sub> NPs solutions .....	29
Figure 3.2	Transfer characteristics of the TFTs with metal oxide NPs .....	30
Figure 3.3	(a) The TEM images of ZnO NPs with different resolutions and (b) the SEM image of SnO <sub>2</sub> NPs .....	31
Figure 3.4	The XRD patterns of the ZnO and SnO <sub>2</sub> NPs films.....	31
Figure 3.5	(a) Device structure of the FIrpic-doped inverted bottom-emission blue phosphorescent OLEDs with an EIL of ZnO NPs and (b) a schematic energy level diagram.....	33

Figure 3.6	(a) Current density-voltage (J-V) and (b) luminance-voltage (L-V) characteristics of the devices with different ZnO NPs thicknesses .....	34
Figure 3.7	(a) Driving voltages and EQEs at 1000 cd/m <sup>2</sup> and (b) normalized EL spectra of the devices with different ZnO NPs layer thicknesses at the same current density (J=5.1 mA/cm <sup>2</sup> ).....	35
Figure 3.8	(a) AFM images (image size is 5 μm × 5 μm) and (b) the RMS roughnesses of the layers of ZnO NPs with different thicknesses .....	37
Figure 3.9	(a) UPS spectra of the ZnO NPs layers with different concentrations, (b) expanded image of the dashed ellipse in (a), (c) expanded image of the solid ellipse in (a), and (d) schematic energy level diagram of cathode, EIL, and ETL.....	39
Figure 3.10	(a) J-V and (b) L-V characteristics of the inverted bottom-emission blue phosphorescent OLEDs with different ETL thicknesses .....	40
Figure 3.11	(a) Driving voltages and the EQEs at 1000 cd/m <sup>2</sup> and (b) normalized EL spectra of the devices with different ETL thicknesses at the same current density (J=5.1 mA/cm <sup>2</sup> ) .....	41
Figure 3.12	(a) J-V-L and (b) EQE, LCE vs J characteristics for the inverted bottom-emission blue phosphorescent OLEDs with different ETLs.....	43
Figure 3.13	(a) Device structure of the green phosphorescent inverted bottom-emission OLEDs with different types of ZnO layer and (b) optical	

absorption spectra of the ZnO films with different thermal annealing temperatures obtained by the sol-gel method. Inset: schematic energy level diagrams of the ZnO layers with different thermal annealing temperatures.....	44
Figure 3.14 (a) J-V and (b) L-V characteristics of the green phosphorescent inverted bottom-emission OLEDs with different types of ZnO as EILs .....	45
Figure 3.15 (a) EQE-L characteristics and (b) normalized EL spectra of the devices with different types of ZnO layers at the same current density ( $J=5.1 \text{ mA/cm}^2$ ).....	46
Figure 3.16 AFM images of the ITOs and the ZnO films on the ITOs with different thermal annealing temperatures (The image size is $5 \times 5 \mu\text{m}^2$ ).....	48
Figure 3.17 XRD patterns of the ZnO films with different thermal annealing temperatures .....	48
Figure 3.18 Angular distribution of radiation irradiance (normalized to the $0^\circ$ irradiance) and the EL spectra of the green phosphorescent inverted bottom-emission OLED (a), (b) with the ZnO NPs layer (20 mg/ml) and (c), (d) without the ZnO NPs layer with different measuring angles .....	50
Figure 3.19 (a) J-V and (b) L-V characteristics of the devices with different $\text{SnO}_2$ NPs concentrations.....	53
Figure 3.20 (a) EQE-J characteristics and (b) driving voltages and LCEs at $1000 \text{ cd/m}^2$ as a function of the $\text{SnO}_2$ NPs concentrations.....	54

Figure 3.21	Normalized EL spectra of the devices with different SnO <sub>2</sub> NPs concentrations at the same current density ( $J=5.1 \text{ mA/cm}^2$ ) .....	54
Figure 3.22	(a) Angular distribution of radiatin irradiance (normalized to the 0° irradiance) and (b) the EL spectra of the green phosphorescent inverted bottom-emission OLED with 1.5 wt% SnO <sub>2</sub> NPs layer with different measuring angles .....	55
Figure 3.23	(a) AFM images (image size is $5 \mu\text{m} \times 5 \mu\text{m}$ ) and (b) RMS roughnesses of the layers of SnO <sub>2</sub> NPs with different thicknesses .....	56
Figure 3.24	(a) Schematic energy level diagram of the cathode, EIL, and ETL, and (b) UPS spectra of the SnO <sub>2</sub> NPs layers with different concentrations.....	58
Figure 4.1	Optical absorption spectra of MoO <sub>3</sub> , undoped TAPC, and MoO <sub>3</sub> doped TAPC films with different MoO <sub>3</sub> concentrations. Inset: increase of CT complex absorption peak (703 nm) as the MoO <sub>3</sub> concentration increases .....	61
Figure 4.2	(a) J-V characteristics of the hole-only devices with different MoO <sub>3</sub> concentrations (solid line: without MoO <sub>3</sub> (5 nm) layer in both electrodes; dashed line: with MoO <sub>3</sub> (5 nm) layer in both electrodes); (b) electrical conductivities of MoO <sub>3</sub> doped TAPC films with different doping concentrations.....	63
Figure 4.3	(a) Device structure and (b) schematic energy level diagram of the phosphorescent white OLEDs .....	65

Figure 4.4	(a) J-V and (b) L-V characteristics of the phosphorescent white OLEDs with different MoO <sub>3</sub> doping concentrations. Inset in (b): L-J characteristics from the same devices .....	66
Figure 4.5	(a) LPE-L characteristics and (b) LPE and EQE of the white OLEDs at 1000 cd/m <sup>2</sup> with different MoO <sub>3</sub> doping concentrations .....	67
Figure 4.6	(a)–(e) Normalized EL spectra of the white OLEDs with different current density at fixed doping concentrations and (f) normalized EL spectra of the white OLEDs with different MoO <sub>3</sub> doping concentrations at the same current density (J=153 mA/cm <sup>2</sup> ). Each inset shows the corresponding CIE color coordinates.....	70
Figure 4.7	(a) Emission ratio of red, orange, blue colors and (b) CRI and CCT of the white OLEDs with different MoO <sub>3</sub> doping concentraions as a function of current density .....	71
Figure 4.8	Typical EL spectra of Firpic, Ir(BT) <sub>2</sub> (acac), Ir(piq) <sub>2</sub> (acac), (b) captured image of the spectra simulation results, (c) EL spectra and (d) CIE color coordinates of simulated and measured white OLEDs (25% doping) and major lighting sources .....	72
Figure 4.9	(a) J-V characteristics of hole-only devices with different HTLs and (b) optical absorption spectra of MoO <sub>3</sub> doped, undoped, and BCP doped TAPC film. Inset in (a): structure of the hole-only device .....	74

Figure 4.10 (a) Device structure and (b) schematic energy level diagram of the inverted bottom-emission white phosphorescent OLEDs with different HTLs.....	76
Figure 4.11 (a) J-V and (b) L-V characteristics of the inverted bottom-emission white phosphorescent OLEDs with different HTLs....	77
Figure 4.12 (a) EQE-J characteristics and (b) driving voltages and LCEs at 1000 cd/m <sup>2</sup> of the inverted bottom-emission white phosphorescent OLEDs with different HTLs.....	78
Figure 4.13 EL spectra of the inverted bottom-emission white phosphorescent OLEDs with (a) MoO <sub>3</sub> doped TAPC, (b) undoped TAPC, and (c) BCP doped TAPC as HTLs with different current densities, (d) emission ratios of red, green, and blue of each device as a function of current density .....	80
Figure 5.1 Schematic device structures of (a) the conventional full-color OLEDs and (b) the full-color OLEDs with CRL .....	84
Figure 5.2 Energy level diagram for the R, G, and B OLED devices .....	87
Figure 5.3 (a) J-V and (b) L-V characteristics of the devices R1 with different hosts and HTLs .....	88
Figure 5.4 (a) EQE, (b) LPE, (c) LCE vs J characteristics and (d) LPE and LCE at 1000 cd/m <sup>2</sup> of devices R1 with different hosts and HTLs .....	89
Figure 5.5 Normalized EL spectra of devices R1 with (a) Spiro-2CBP, (b) $\alpha$ -NPD, (c) TAPC, (d) BBTC, and (e) CBP as hosts and HTLs at different driving voltages. ....	91

Figure 5.6	(a) J-V and (b) L-V characteristics of the devices G1 and G2 with different HTLs.....	93
Figure 5.7	(a) Schematic energy levels of Ir(piq) <sub>2</sub> (acac) doped Spiro-2CBP, $\alpha$ -NPD, TAPC, BBTC, and CBP with the hole trap depth ( $\Delta E_{\text{HOMO}}$ ) calculated from the difference of the HOMO energy levels between the host and dopant materials. (b) Driving voltage changes at 1000 cd/m <sup>2</sup> with and without CRL as a function of $\Delta E_{\text{HOMO}}$ .....	93
Figure 5.8	J-V characteristics of the hole-only devices with pristine and Ir(piq) <sub>2</sub> (acac) doped Spiro-2CBP, $\alpha$ -NPD, TAPC, BBTC, and CBP. (a)–(e) The driving voltage changes by doping at the same current density are high in the sequence of CBP, Spiro-2CBP, BBTC, TAPC, and $\alpha$ -NPD due to the difference of trap levels. (f)–(g) Comparison of hole transport properties between Spiro-2CBP, TAPC, BBTC, and CBP, and those of Ir(piq) <sub>2</sub> (acac) doped films.....	95
Figure 5.9	Comparison of the absorption spectra of hole transport materials, (a) Spiro-2CBP, (b) $\alpha$ -NPD, (c) TAPC, (d) BBTC, and (e) CBP and Ir(piq) <sub>2</sub> (acac) doped hole transport materials. No significant absorption change is observed in visible spectral region .....	96
Figure 5.10	(a) EQE, (b) LPE, (c) LCE vs J characteristics and (d) LPE and LCE at 1000 cd/m <sup>2</sup> of devices G1 and G2 with different HTLs	97

Figure 5.11 Normalized EL spectra of the devices G1 and G2 with (a) Spiro-2CBP, (b) $\alpha$ -NPD, (c) TAPC, (d) BBTC, and (e) CBP as HTLs at different driving voltages .....	98
Figure 5.12 (a) J-V and (b) L-V characteristics of the devices B1 and B2 with different HTLs.....	100
Figure 5.13 Driving voltage changes of the blue phosphorescent devices at 1000 cd/m <sup>2</sup> with and without CRL as a function of $\Delta E_{\text{HOMO}}$ ....	100
Figure 5.14 (a) EQE, (b) LPE, (c) LCE vs J characteristics and (d) LPE and LCE at 1000 cd/m <sup>2</sup> of the devices B1 and B2 with different HTLs .....	102
Figure 5.15 Normalized EL spectra of the devices B1, B2, and B3 with (a) Spiro-2CBP, (b) $\alpha$ -NPD, (c) TAPC, (d) BBTC, and (e) CBP as HTLs at different driving voltages .....	104
Figure 5.16 CIE color coordinates and color gamut of the devices R1, G1, G2, B1, and B2 at 8 V with different HTLs of (a) Spiro-2CBP, (b) $\alpha$ -NPD, (c) TAPC, (d) BBTC, and (e) CBP .....	105
Figure 5.17 Energy level diagram for the full-color inverted bottom-emission OLED devices .....	109
Figure 5.18 (a) J-V and (b) L-V characteristics of the devices R4 with different hosts and HTLs .....	111
Figure 5.19 (a) EQE, (b) LPE, (c) LCE vs J characteristics and (d) LPE and LCE at 1000 cd/m <sup>2</sup> of the devices R4 with different hosts and HTLs.....	112

Figure 5.20 Normalized EL spectra of the devices R4 with (a) Spiro-2CBP, (b) TAPC, (c) BBTC, and (d) CBP as hosts and HTLs at different driving voltages .....	113
Figure 5.21 (a) J-V and (b) L-V characteristics of the devices G4 and G5 with different HTLs.....	115
Figure 5.22 Driving voltage changes at 1000 cd/m <sup>2</sup> with and without CRL as a function of $\Delta E_{\text{HOMO}}$ .....	115
Figure 5.23 (a) EQE, (b) LPE, (c) LCE vs J characteristics and (d) LPE and LCE at 1000 cd/m <sup>2</sup> of the devices G4 and G5 with different HTLs .....	117
Figure 5.24 Normalized EL spectra of the devices G4 and G5 with (a) Spiro-2CBP, (b) TAPC, (c) BBTC, and (d) CBP as HTLs at different driving voltages .....	118
Figure 5.25 (a) J-V and (b) L-V characteristics of the devices B4 and B5 with different HTLs.....	119
Figure 5.26 Driving voltage changes of the devices B4 and B5 at 1000 cd/m <sup>2</sup> with and without CRL as a function of $\Delta E_{\text{HOMO}}$ .....	120
Figure 5.27 (a) EQE, (b) LPE, (c) LCE vs J characteristics and (d) LPE and LCE at 1000 cd/m <sup>2</sup> of the devices B4 and B5 with different HTLs .....	121
Figure 5.28 Normalized EL spectra of the devices B4 and B5 with (a) Spiro-2CBP, (b) TAPC, (c) BBTC, and (d) CBP as HTLs at different driving voltages .....	122

Figure 5.29 Normalized EL spectra of the devices B6 with (a) Spiro-2CBP, (b) TAPC, (c) BBTC, and (d) CBP as HTLs with different driving voltages.....	123
Figure 5.30 CIE color coordinates and color gamut of the devices R4, G4, G5, B4, and B5 at 13 V with different HTLs of (a) Spiro-2CBP, (b) TAPC, (c) BBTC, and (d) CBP .....	124

# Chapter 1. Introduction

## 1.1 Organic Light-Emitting Diodes

Recently, organic light-emitting diodes (OLEDs) have attracted a great attention due to their applications in full-color displays, backlights of liquid crystal displays (LCDs), and solid-state lighting sources. OLEDs have many advantages such as thin thickness, light weight, availability for flexible device, high efficiency, vivid color, and potential for low-cost fabrication.

Full-color OLEDs display is already utilized in commercial products such as mobile phones, digital cameras, and portable multimedia players. Samsung and LG demonstrated their 55 inch full-color TVs in the society for information display (SID) international symposium, seminar, and exhibition 2012 as shown in Figure 1.1. Samsung and LG utilized fine metal mask (FMM) and color filter with white OLEDs technique, respectively. These large-size OLEDs TVs will be mass-produced and come to market soon. In addition, some solid-state lighting sources using OLEDs are on the market, and flexible and transparent OLEDs displays will be available in the near future.

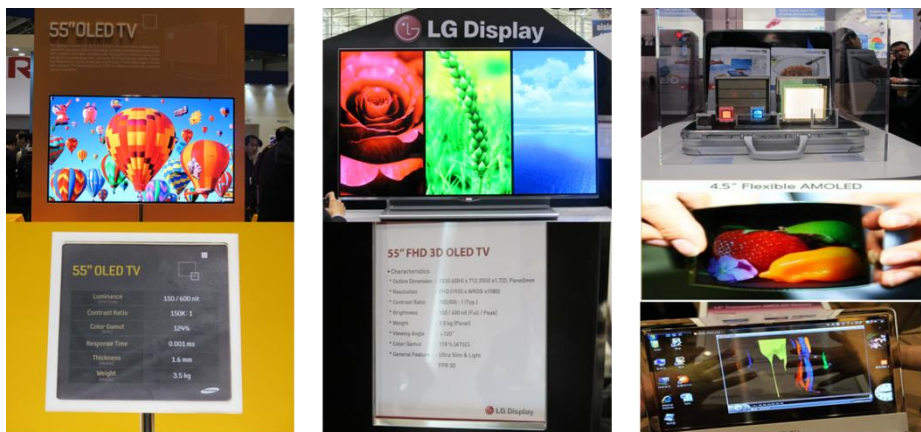


**Figure 1.1** The main applications of OLEDs.

The observation of electroluminescence (EL) in organic materials was first reported by Pope, Kallmann, and Magnate in 1963 [1]. However, they used single crystal anthracene with 10  $\mu\text{m}$  to 20  $\mu\text{m}$  thick and could observe emitted light from anthracene above about 400 V, which are difficult to use them as a practical product. Vityuk and Mikho established that vapor-deposited thin films of anthracene also exhibit EL [2]. Subsequently, Vincett *et al.* reported clearly visible EL from an organic material at voltages significantly less than 100 V using vacuum-deposited anthracene, but external quantum efficiency (EQE) of the device is about 0.03%–0.06% [3]. Partridge reported first EL generation from organic polymer films [4].

Practically available OLEDs were invented by Tang and VanSlyke in 1987 [5]. The device has a double-layer structure of organic thin films, prepared by vacuum deposition. The aromatic diamine as a hole transport layer (HTL) and 8-hydroxyquinoline aluminum ( $\text{Alq}_3$ ) as an emitting and

electron transport layer (ETL) were used. Total thickness of the device was approximately 135 nm, which is much thinner than previous organic EL devices. The device emitted green color with high EQE (1%) and brightness ( $> 1000 \text{ cd/m}^2$ ) at a driving voltage below 10 V. Tang *et al.* improved the efficiency of OLEDs by about a factor of 2 in comparison with the undoped device by introducing molecular doping system in 1989 [6]. Moreover, the EL colors can be readily tuned by a suitable choice of dopants as well as by changing the concentration of the dopant. Above works were achieved by using small molecular weight organic materials and the vacuum thermal evaporation technique. In 1990 Burroughes *et al.* reported the first conjugated polymer light-emitting diodes (PLEDs) by spin-coating poly(p-phenylene vinylene) on the indium-tin-oxide (ITO) coated glass substrate and the maximum quantum efficiency of the device is about 0.05% [7]. The availability of solution process means that PLEDs have a potential of low-cost fabrication for large-size device compared with vacuum thermal evaporation. Kido *et al.* demonstrated first white OLEDs by using polymer doped with blue, green, and orange fluorescent dyes [8]. Though the efficiency of the device is low, this result suggests that OLEDs can be utilized for illumination devices as well as backlights of LCDs. After that, there are many efforts such as synthesizing efficient materials and developing novel device structures to improve the efficiency of OLEDs. However, the efficiency of the device was low because they used only fluorescence. When the electrically injected electrons and holes are recombined, the singlet and triplet excited states are generated with the ratio of 1:3, statistically. Fluorescence utilizes only singlet

excitons so the internal quantum efficiency (IQE) of OLEDs with the fluorescent emitter is theoretically limited to 25%.

M. A. Baldo *et al.* dramatically improved the efficiency of OLEDs by the introduction of the phosphorescent dye 2,3,7,8,12,13,17,18-octaethyl-21H,23H-porphine platinum(II) (PtOEP) [9]. Using phosphorescent material means that the IQE of OLEDs can be theoretically 100% because phosphorescence utilizes triplet excitons as well as singlet excitations. Tandem structure using charge generation layers and p-i-n structure using electrical doping also intensely improved the performance of OLEDs [10, 11]. Today, the performances of OLEDs are surprisingly enhanced and organic materials with high efficiency and stability are being developed from several companies. The recent status of commercially available OLED emitter materials are summarized in Table 1.1.

Though the performance of OLEDs is improved, there are still many problems to resolve. For example, deep blue phosphorescent materials are not commercially available due to their low efficiency and lifetime. The lifetime of the fluorescent deep blue emitter material is generally longer than that of the deep blue phosphorescent material but its efficiency is lower than that of the phosphorescent materials. Phosphorescent light blue materials have lifetime which covers solid-state lighting sources or displays of mobile phones but cannot covers TVs. Light blue color leads to low color gamut in TV so deep blue phosphorescent materials with high efficiency and long life time are required.

Recent phosphorescent materials show the IQE of 100% but EQE is generally limited to 20% due to an optical loss by glass substrate, ITO, and organic materials. Many researchers have studied to increase out-coupling efficiency by using various methods such as external macro-extractor, micro-lens array, surface scattering layers, low-index grid, high-index substrates, and internal extraction layers [14–18]. Panasonic in Japan recently reported light extraction efficiency of 47 % and achieved highly efficient all phosphorescent white OLEDs with 85 lm/W and lifetime of about 100000 hours at 1000 cd/m<sup>2</sup> [19].

To expand OLEDs market and compete with LCDs, mass production of OLEDs TV panels and reduction of fabrication cost are absolutely required. For example, one of problems is the FMM process. Three colors of red (R), green (G), and blue (B) are required for full-color display. The FMM is utilized to form these 3 colors of RGB sub-pixels. This FMM technique causes defects and color mixing due to sagging and misalignment of FMM when it is applied to large-size OLEDs displays [20]. Many companies endeavor to commercialize OLEDs TV panels by resolving several problems.

**Table 1.1** The status of OLED emitter materials

	<b>Color</b>	<b>CIE (x, y)</b>	<b>Efficiency (cd/A)</b>	<b>LT50 (hrs)</b>	<b>Company</b>	<b>Ref.</b>
<b>Fluorescence</b>	Red	(0.67, 0.33)	11	160000	Idemitsu Kosan (CIE, Efficiency: at 10mA/cm <sup>2</sup> , LT50: at 1000cd/m <sup>2</sup> )	[12]
	Green	(0.29, 0.64)	37	200000		
	Blue	(0.14, 0.12)	9.9	11000		
<b>Phosphorescence</b>	Deep Red	(0.69, 0.31)	17	250000	Universal Display Corporation (at 1000 cd/m <sup>2</sup> )	[13]
	Red	(0.64, 0.36)	30	900000		
	Yellow	(0.44, 0.54)	81	1450000		
	Green	(0.31, 0.63)	85	400000		
	Light Blue	(0.18, 0.42)	50	20000		

## 1.2 Inverted Structure OLEDs

In the case of full-color displays, the attention is focused on the active-matrix (AM) OLEDs because of its superior performance compared with passive-matrix OLEDs. The AM OLEDs are already utilized in main display of smart phones. However, there are many technical issues that have to be resolved for developing large-size AM OLEDs. One of the issues is a backplane technology. Since low-temperature polycrystalline silicon (LTPS) [21, 22] has many merits such as high mobility, operating stability, and availability of both *n*-type and *p*-type thin film transistors (TFTs), most commercial AM OLED products use the LTPS-TFT backplane instead of amorphous silicon (a-Si) TFT backplane [23, 24]. But the LTPS-TFT backplane has some drawbacks such as poor uniformity and increase of manufacturing cost as the size of the display panel increases. On the other hand, the a-Si-TFT and oxide-TFT [25] backplanes have more advantage for large-size panels because of their good uniformity and low manufacturing cost compared with the LTPS-TFT. Therefore, there is a growing interest in developing the a-Si-TFT or oxide-TFT process that can be adapted to the AM OLED backplane. Because most a-Si-TFT and oxide-TFT have the *n*-type transistor characteristics, the inverted structure OLED with the bottom cathode is more advantageous than the conventional structure OLED with the bottom anode. When the conventional structure OLED is used with *n*-type transistors, some voltage drop happens in the AM OLED display because the anode of the OLED is connected to the source of TFT, leading to image sticking [26]. In contrast,

there is no voltage drop in the AM OLED display with  $n$ -type transistors using the inverted structure OLED because the bottom cathode of the inverted OLED can be directly connected to the  $n$ -type TFT drain line as shown in Figure 1.2.

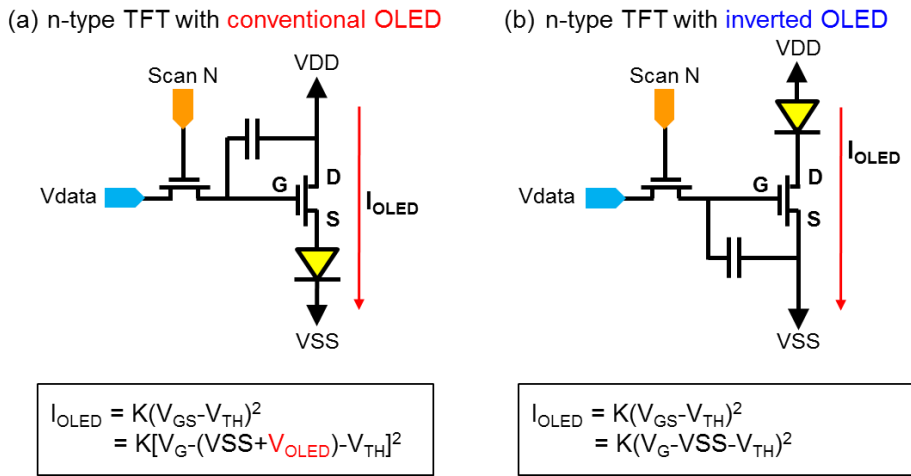


**Figure 1.2** Schematic of the pixel circuits connected with (a) the conventional structure OLED and (b) the inverted structure OLED.

### 1.2.1 Inverted top-emission OLEDs

There are three types of inverted structure OLEDs which are top-emission, bottom-emission, and transparent structures. Inverted top-emission OLEDs usually has transparent anode and metal cathode with high reflectance because the light is emitted from top anode. For efficient inverted top-emission OLEDs, efficient electron injection from the bottom cathode to the ETL and transparent and conductive anode are required.

Various metals with low work function can be used for bottom cathode in inverted top-emission OLEDs because bottom cathode does not need to be transparent. Aluminum (Al), silver (Ag), magnesium (Mg) are used as cathodes [27–30]. Thin lithium fluoride (LiF), magnesium oxide (MgO), lead monoxide (PbO), pentacene, and *n*-type doped organic materials are used as electron injection layers for efficient electron injection [31–35].

Transparent anodes were also studied intensively. Some researchers utilized ITO as an anode of inverted top-emission OLEDs due to its optical transparency [29, 30, 35] but it is known that the sputter deposition of ITO can cause radiation damage to the organic layers [36]. Other researchers have used various semitransparent films such as gold (Au), nickel oxide (NiO), silver (Ag), and indium zinc oxide as the top anode of inverted top-emission OLEDs [37–40]. However, these semitransparent metal anodes have low electrical conductivity and can induce the change of EL spectra at different viewing angles due to microcavity effect [39]. Various organic materials were used as a capping layer on the semitransparent anode to overcome the shift of EL spectrum [33]. But, this additional capping layer leads to increase of fabrication cost and complexity.

### **1.2.2 Inverted bottom-emission OLEDs**

Inverted bottom-emission OLEDs usually has transparent cathode and metal anode with high reflectance because the light is emitted from a bottom cathode. For efficient inverted bottom-emission OLEDs, transparent cathode

and efficient electron injection from the bottom cathode to the ETL are required.

Efficient electron injection is an important issue in the inverted bottom-emission OLEDs because there are few proper cathode materials for the device. The ITO is usually used as a cathode in the inverted bottom-emission OLEDs because of its high optical transparency and electrical conductivity. But the ITO has a high work function ( $\sim 4.7$  eV), which can limit the injection of electron. In order to improve the electron injection from the ITO cathode, various methods have been reported such as an insertion of thin metallic layers with low work functions [41] and use of *n*-type doped ETLs using lithium (Li) [42], cesium (Cs) compound [43–45], and rubidium (Rb) compound [46]. However, such methods can lead to operational instability by oxidation of metal or diffusion of metal dopants [47, 48]. An organic *p-n* junction was also used as an efficient cathode in the flexible inverted OLEDs [49]. But all above methods need a vacuum process which makes the manufacturing costs increase. In this respect, electron injection layers (EILs) using solution processes are much attractive. Zhong et al. reported efficient solution processable and cross-linkable electron injection conjugated polymer materials [50]. They achieved high efficiency inverted PLEDs using this conjugated polymer layer because that EIL reduced the work function of ITO cathode. However, this conjugated polymer EIL requires additional cross-linking process by heating over 150°C and fluorescence lamp illumination. This heat treatment is not good for flexible device because the flexible substrate is usually weak for high temperature. Other candidates for the EIL in

inverted bottom-emission OLEDs are *n*-type metal oxides such as zinc oxide (ZnO), titanium oxide (TiO<sub>2</sub>), and zirconium dioxide (ZrO<sub>2</sub>) [51–54].

However, most *n*-type metal oxides EILs are obtained by the sol-gel methods, which need high temperature annealing process for better electron transport properties [55, 56]. However, this high temperature annealing process is not suitable for flexible electronic devices. *N*-type metal oxides using self-assembled dipole molecules (SADMs) were also used inverted bottom-emission PLEDs [57]. But, the SAM process is very sensitive to the preparation conditions such as the temperature, the humidity, and the substrate roughness and not easy to control the thickness of thin SAM layer [58].

Therefore, development of EIL with optically high transparency, good electron transport and injection property, and low-cost process is required for efficient inverted bottom-emission OLEDs.

### **1.2.3 Inverted transparent OLEDs**

Inverted transparent OLEDs should have transparent cathode and anode because the light is emitted from both electrodes. In other words, inverted transparent OLEDs are inverted bottom-emission OLEDs with a transparent anode. Transparent cathode, anode and efficient electron injection layers are required. Zhou *et al.* used ITO and gold (Au) as a transparent conductive cathode and anode, respectively, in inverted transparent OLEDs [42]. Some papers demonstrated inverted transparent OLEDs using ITO as a cathode and an anode [59, 60].

### 1.3 Outline of Thesis

This thesis is composed of six chapters including **Introductions** and **Conclusion**. As an introductory part, **Chapter 1** provides brief history and recent research trend of OLEDs. In addition, it also includes necessity and significant issues of inverted structure OLEDs. In **Chapter 2**, preparation methods of ZnO nanoparticles (NPs) and ZnO precursor solution are described in detail. The chemical structures of all used organic materials are also demonstrated. In addition, the fabrication and characterization methods for the OLED devices are summarized in this chapter. In **Chapter 3**, the optical and electrical properties of metal oxide NPs layer were investigated and we fabricated inverted bottom-emission OLEDs using these metal oxide NPs layers as EILs. The ZnO NPs and tin dioxide ( $\text{SnO}_2$ ) NPs were used for metal oxide NPs layers. We studied the effects of the metal oxide NPs layer thickness, the ETL thickness, the energy levels of the metal oxide NPs layers, the morphology of metal oxide NPs layers, and lowest-unoccupied-molecular-orbital (LUMO) energy levels of the ETLs for high-performance inverted bottom-emission OLEDs. In addition, we compared the device using the metal oxide NPs with the device without metal oxide NPs. **Chapter 4** contains the change of the device performance by controlling the conductivity of the HTL. In order to increase hole conductivity of the HTL, we utilized *p*-type doping. We investigated the optical and electrical properties of *p*-type doped HTL as the molybdenum trioxide ( $\text{MoO}_3$ ) doping concentrations change. Furthermore, we studied the recombination region shift of the white OLEDs by using

developed *p*-type doped HTLs with various MoO<sub>3</sub> doping concentrations. We also reduce hole conductivity of HTL by doping the 2,9-dimethyl-4,7-diphenyl-1,10-phenanthroline (BCP) to the HTL. We studied the effect of hole conductivity in the inverted bottom-emission OLEDs by using HTLs with different hole conductivities. In **chapter 5**, we inserted red dye doped HTL which is called a common red layer (CRL) between the undoped HTL and the electron blocking layer (EBL) for improving electron-hole balance of OLEDs. We investigated the device performance depending on the highest-occupied-molecular-orbital (HOMO) energy levels of HTLs by using different hole transport materials. We fabricated full-color (R, G, and B) OLEDs and compared the devices inserting the CRLs with the devices without the CRLs. We also fabricated full-color inverted bottom-emission OLEDs using the CRLs and compared the performances with the devices without CRLs. Finally, some concluding remarks of this thesis are made in **Chapter 6**.

## Chapter 2 Experimental Methods

### 2.1 Materials

#### 2.1.1 Preparation of ZnO nanoparticles and precursor solution

The ZnO NPs were prepared [61] modifying the method reported by C. Pacholski *et al.* [62]. At first, 1.23 g of  $\text{Zn}(\text{Ac})_2 \cdot 2\text{H}_2\text{O}$  was dissolved in 55 ml of methanol at room temperature. Then, 25 ml of a methanol solution containing 0.48 g of KOH was added dropwise at 60°C with magnetic stirring. The reaction mixture was kept at 60°C with magnetic stirring for 2 h under  $\text{N}_2$  flow. The product appeared as white precipitate. After collecting by centrifugation, this white precipitate was washed with methanol. Finally, the precipitate could be redispersed in n-butanol. For determining the ZnO concentration, a known amount of the colloidal solution was dried and the residual powder was weighed.

For the ZnO precursor solution, zinc acetate dehydrate ( $\text{Zn}(\text{CH}_3\text{COO})_2$ , 99.999%), ethanolamine (EA;  $\text{NH}_2\text{CH}_2\text{CH}_2\text{OH}$ , 99%), chlorobenzene ( $\text{C}_6\text{H}_5\text{Cl}$ , anhydrous, 99.8%), methanol ( $\text{CH}_3\text{OH}$ , 99.8%), isopropyl alcohol ( $\text{C}_3\text{H}_8\text{O}$ , 99.9%), and acetone ( $(\text{CH}_3)_2\text{CO}$ , 99.5%) were purchased from Sigma-Aldrich Chemical Co., Inc. The ZnO precursor solution was prepared [63] by dissolving zinc acetate dehydrate (0.5487 g, 0.5 molar) in methanol (5 mL) and equal-molar ethanolamine (0.15 mL). The

mixed solution was then stirred at 55 °C for 1 hour to obtain a transparent mixture, after which it was aged for 48 hours at room temperature.

### **2.1.2 Preparation of other materials**

The SnO<sub>2</sub> NPs dissolved in H<sub>2</sub>O were purchased from commercial company (MKnano). The MoO<sub>3</sub>, lithium fluoride (LiF), and aluminum (Al) were purchased from commercial company (CERAC). Most organic materials were purchased from commercial company (Luminescence Technology Corporation) and used without further purification.

### 2.1.3 Chemical structures of organic materials

Below figures are chemical structures of organic materials used in this thesis.

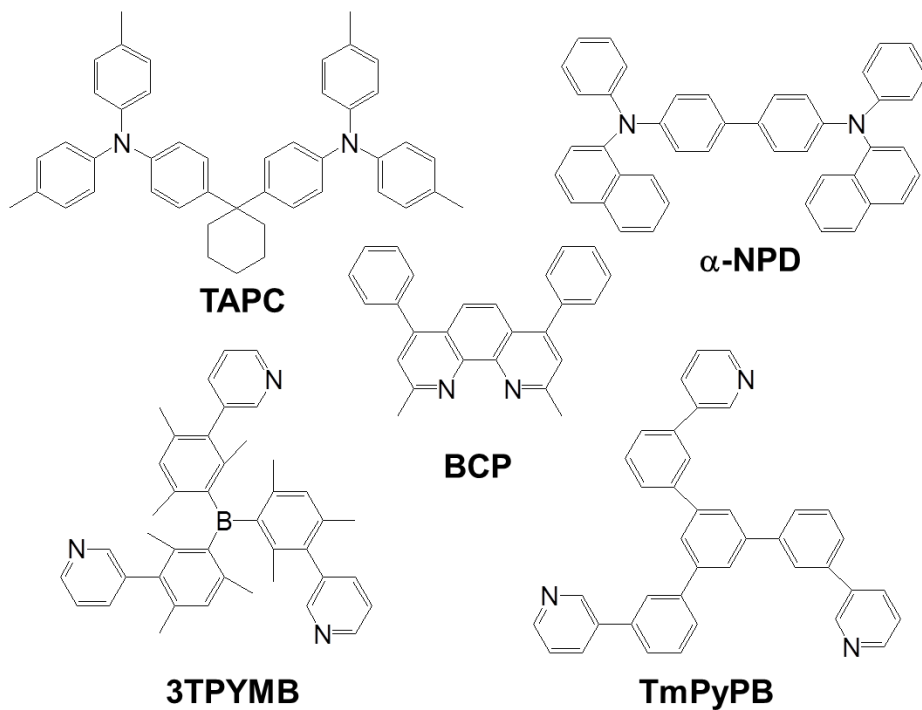


**Figure 2.1** Chemical structures of di-[4-(N,N-ditolyl-amino)-phenyl]cyclohexane (TAPC) and N,N'-di(1-naphthyl)-N,N'-diphenylbenzidine ( $\alpha$ -NPD) as hole transport materials and 2,9-dimethyl-4,7-diphenyl-1,10-phenanthroline (BCP), tris[2,4,6-trimethyl-3-(pyridine-3-yl)phenyl]borane (3TPYMB), and 1,3,5-tri[(3-pyridyl)-phen-3-yl]benzene (TmPyPB) as electron transport materials.

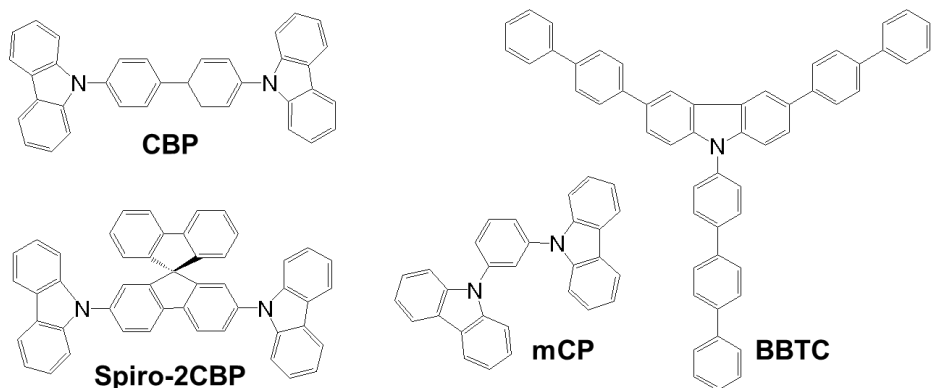


**Figure 2.2** Chemical structures of 4,4'-bis(carbazol-9-yl)biphenyl (CBP), 2,7-bis(carbazol-9-yl)-9,9-spirobifluorene (Spiro-2CBP), 1,3-bis(carbazol-9-yl)benzene (mCP), and 3,6-bis-biphenyl-4-yl-9-[1,1',4',1'']terphenyl-4-yl-9H-carbazole (BBTC) as phosphorescent host materials.

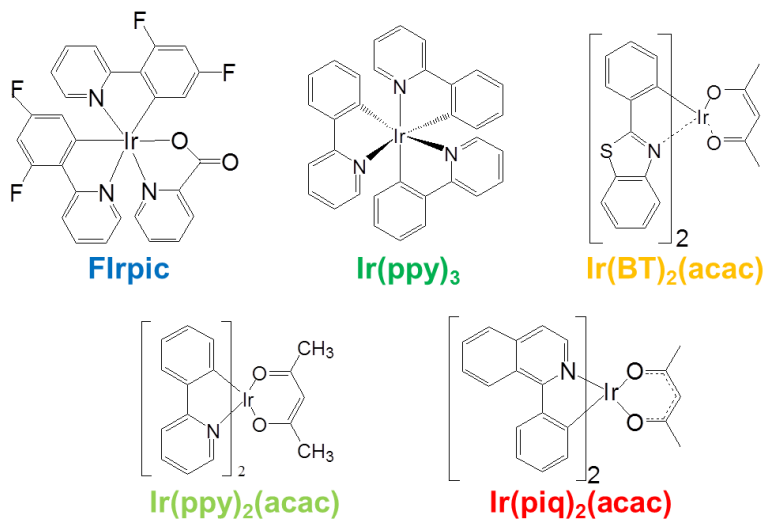


**Figure 2.3** Chemical structures of phosphorescent dopant materials which are bis(3,5-difluoro-2-(2-pyridyl)phenyl-(2-carboxypyridyl)iridium(III) (FIrpic) for blue emitting, tris(2-phenylpyridine)iridium(III) (Ir(ppy)<sub>3</sub>) and bis(2-phenylpyridine)(acetylacetonate)iridium(III) (Ir(ppy)<sub>2</sub>(acac)) for green emitting, bis(2-phenylbenzothiazolato)(acetylacetonate)iridium(III) (Ir(BT)<sub>2</sub>(acac)) for orange emitting, and bis(1-phenylisoquinoline)(acetylacetonate)iridium(III) (Ir(piq)<sub>2</sub>(acac)) for red emitting.

## 2.2 Device Fabrication and Characterization Methods

### 2.2.1 Device fabrication

All devices used in this thesis have slightly different structures in each chapter to obtain optimized performances. Specified device structures and processes are described in each chapter. Typical device fabrication methods are as follows: The patterned ITO coated glass substrates were cleaned in ultrasonic bath (Branson 5510) with acetone, isopropyl alcohol, and deionized water. The cleaned substrates were dried in ambient oven at 120°C for more than 1 hour. For the standard structure, ITO coated glass substrates were treated with ultraviolet-ozone cleaner (UVO-42) to remove the surface hydrocarbon contamination and increase the work function of the ITO. For the inverted structure, ZnO NPs, ZnO precursor solution, and SnO<sub>2</sub> NPs layers were deposited on the substrates by spin-coating at a speed of 2000 rpm for 60 seconds. The ZnO and SnO<sub>2</sub> NPs layers were dried in the oven filled with nitrogen gas at a temperature of 90°C and 100°C, respectively, for eliminating solvents. The deposited ZnO precursor layers were dried on the hot plate with 100°C, 200°C, and 300°C in air for formation of ZnO films. For good wetting on the substrates, the substrates were ultraviolet-ozone treated for 10 minutes when ZnO precursor solution and SnO<sub>2</sub> NPs were deposited. The vacuum deposition of thin films was performed by thermal evaporation under a base pressure of  $1-5 \times 10^{-6}$  Torr at a rate of 0.2-2 Å/s for organic semiconducting

materials, 0.04–0.1 Å/s for LiF (electron injection material), 0.2–0.5 Å/s for MoO<sub>3</sub> (hole injection material) and 3–5 Å/s for Al (metal cathode or anode), respectively. The evaporation speed was monitored with a quartz-oscillator thickness monitor. The doping concentration was adjusted by varying the relative evaporation speeds of the host and dopant materials. A brief scheme of inverted structure OLEDs fabrication process used in this thesis is presented in Figure 2.4.

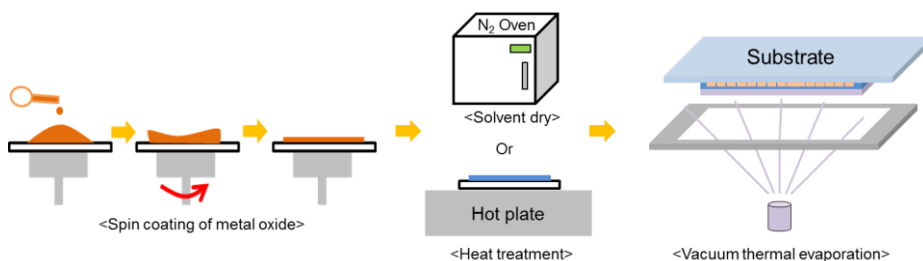


**Figure 2.4** A scheme of the inverted OLEDs fabrication process.

## 2.2.2 Current-voltage-luminance measurement

Fabricated device was mounted onto the cryostat for the current-voltage-luminance (I-V-L) measurement. The emitting area is  $1.4 \times 1.4 \text{ mm}^2$  which is defined by the crossing overlap of patterned ITO and Al electrodes. Most of the devices were measured at room temperature.

The I-V characteristics were measured with a Keithley 236 source measurement unit, while the EL was measured with a calibrated Si photodiode (Hamamatsu, S5227-1010BQ) with a size of  $10 \text{ mm} \times 10 \text{ mm}$  placed at an

angle normal to the device surface, assuming that the device was a Lambertian source. An ARC PD438 photomultiplier tube (PMT) was also used to detect a turn-on voltage of OLEDs. The EL spectra and the Commission Internationale de L'Eclairage (CIE) color coordinates were measured with a Konica-Minolta CS-1000A spectroradiometer. The luminance and efficiency were calculated from the photocurrent signal of the photodiode with a Keithley 2000 multimeter, and corrected precisely with the luminance from the CS-1000A. Schematic diagrams of I-V-L and EL spectra measurement are shown in Figure 2.5(a) and 2.5(b), respectively.

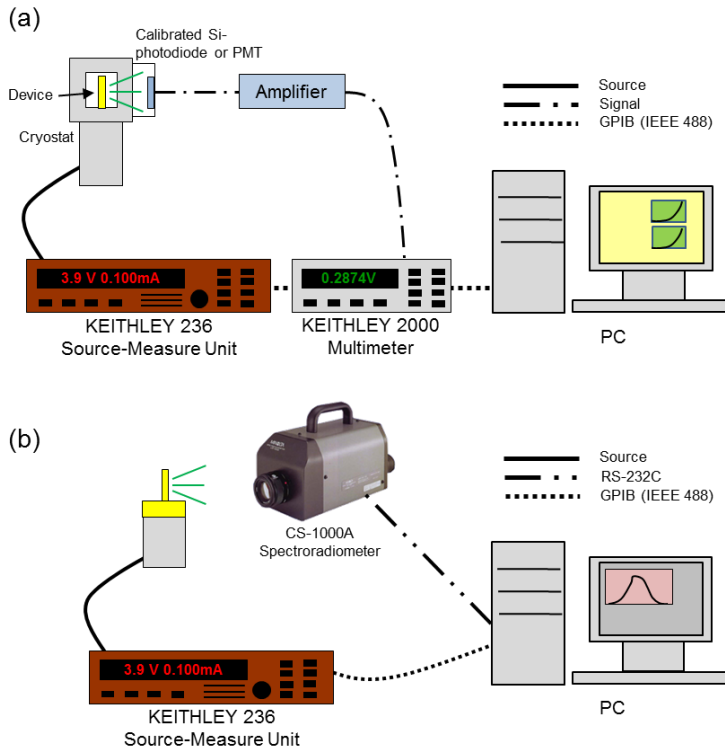


**Figure 2.5** Schematic diagrams for the measurement of (a) I-V-L characteristics and (b) EL spectra.

The chromatic characteristics can also be calculated from the EL spectra measured by the CS-1000A spectroradiometer using the CIE 1931 color expression system. The XYZ tristimulus values can be calculated by following equations,

$$X = K_m \int_0^{\infty} \bar{x}(\lambda)P(\lambda)d\lambda \quad (2.1)$$

$$Y = K_m \int_0^{\infty} \bar{y}(\lambda)P(\lambda)d\lambda \quad (2.2)$$

$$Z = K_m \int_0^{\infty} \bar{z}(\lambda)P(\lambda)d\lambda \quad (2.3)$$

where,  $P(\lambda)$  is a given spectral power distribution of emissive source,  $\bar{x}$ ,  $\bar{y}$  and  $\bar{z}$  are the CIE standard color matching functions (see Figure 2.6(a)) and  $K_m$  is the weighing constant (683 lm/W). From the tristimulus values, the CIE color coordinates calculated by following equations,

$$x = \frac{X}{X+Y+Z} \quad (2.4)$$

$$y = \frac{Y}{X+Y+Z} \quad (2.5)$$

$$z = \frac{Z}{X+Y+Z} \quad (2.6)$$

Any color can be plotted on the CIE chromaticity diagram as shown in Figure 2.6(b).

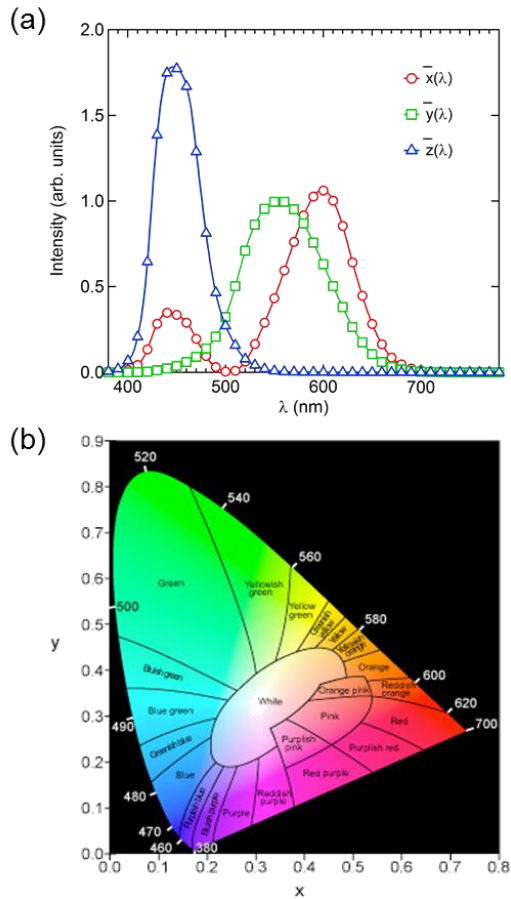


**Figure 2.6** (a) The CIE standard observer color-matching functions and (b) the CIE 1931 color space chromaticity diagram. The outer curved boundary is the spectral locus, with wavelengths shown in nanometers.

### 2.2.3 Electroluminescence efficiency calculation

To evaluate the emission properties of OLEDs, the commonly employed efficiencies are the EQE, the luminous current efficiency (LCE) and the luminous power efficiency (LPE).

The EQE can be defined by the following equation.

$$\text{EQE} = \frac{\text{number of emitted photons}}{\text{number of injected electrons}} [\%] \quad (2.7)$$

Typically, OLEDs emit light into the half plane due to the reflective metal electrode. Without any modification for increasing out-coupling efficiency, over 80% of the emission can be lost to internal absorption and wave-guiding in a simple planar light-emitting device.

Since human eye has different spectral sensitivity in visible spectral area, the response of the eye is standardized by the CIE in 1924 (see  $\bar{y}$  in Figure 2.6(a)). The luminous efficiency weighs all emitted photons according to the photopic response of human eye. The difference is that EQE weighs all emitted photons equally. The LCE can be expressed by the following equation.

$$\text{LCE} = \frac{\text{luminance [cd/m}^2\text{]}}{\text{current density [A/m}^2\text{]}} [\text{cd/A}] \quad (2.8)$$

The luminance value ( $\text{cd/m}^2$ ) can be easily measured by the commercial luminance meter (CS-1000A in this thesis). One candela (cd) means one lumen (lm)/steradian.

The LPE is the ratio of the lumen output to the input electrical power as follows,

$$\text{LPE} = \frac{\text{luminous flux [lm]}}{\text{electrical power [W]}} [\text{lm/W}] \quad (2.9)$$

## 2.2.4 Angular dependent electroluminescence measurement

Angular dependent EL intensity and spectra were measured from  $0^\circ$  to  $90^\circ$  by using an optical fiber and an Acton Spectro-275 monochromator combined with an ARC PD438 PMT on a rotation stage. A schematic diagram of this measurement system is depicted in Figure 2.7.

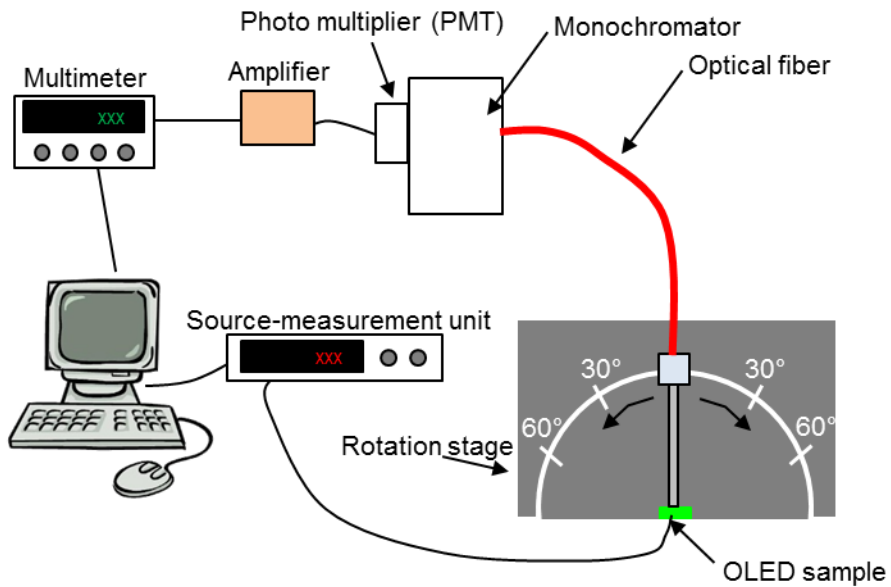


**Figure 2.7** A schematic diagram of the angular dependent EL measurement set up.

## 2.2.5 Other characterization methods

UV-Visible Spectroscopy: The absorption spectra were measured with DU-70 UV/Vis Scanning Spectrophotometer (Beckman Coulter, Inc.). For the film measurement, materials were spin-coated or thermally evaporated with the thickness of ~100 nm on the quartz substrate.

Atomic Force Microscopy (AFM): Topography of each film was measured by XE-100 (Park Systems) AFM System. Most of the films were measured in non-contact mode with NCHR probe tip (320 kHz, 42 N/m) followed by image processing in Gwyddion v.2.22 and XEI v.1.7.1.

Energy Level Measurement: The HOMO energy levels of organic materials were measured by Model AC-2 Photoelectron Spectrometer (RKI Instruments) in ambient atmosphere at room temperature. The materials were deposited on the ITO coated glass substrate.

X-Ray Diffraction (XRD): To check the crystalline structure of films, XRD patterns were obtained from MXP18XHFSRA-22 (MAC Science Co.) between 5° and 80°. All films were deposited on the quartz substrates.

Transmission Electron Microscopy (TEM): The size of ZnO NPs was measured by an H-7600 (Hitachi) TEM operated at an acceleration voltage of 100 kV.

Field Emission Scanning Electron Microscopy (FE-SEM): The size of SnO<sub>2</sub> NPs was measured by S48000 FE-SEM (Hitachi).

Ultraviolet Photoelectron Spectroscopy (UPS): The energy levels of ZnO NPs, SnO<sub>2</sub> NPs, and ZnO film obtained from sol-gel method were measured by AXIS-NOVA (Kratos. Inc) UPS at  $3.5 \times 10^{-9}$  Torr. The metal oxides layers were deposited on the ITO coated glass substrates using a spin-coating method.

Semiconductor Parameter Analyzer: The transfer characteristics of TFTs with metal oxide were measured in glove box filled with N<sub>2</sub> gas at room temperature by using a 4155C (Agilent) semiconductor parameter analyzer.

Color Rendering Index (CRI): The CRI means that how well the light matches a black body at the equivalent color temperature (CRI > 80 desired, < 50 unacceptable for a lighting source). The CRI value is calculated from the EL spectra using CIE D008, Rel. 2.0 – 1994 program.

Film Thickness Measurement: Ellipsometers (L2W15S830 with 632.8-nm He-Ne laser light, Gaertner Scientific Corp. and M2000D, Woollam) and an AFM (XE-100, Park Systems) were used for measuring the thicknesses of films.

## **Chapter 3. Inverted Bottom-Emission OLEDs Using Metal Oxide Nanoparticles**

The EIL is very important in the inverted structure OLEDs because poor electron injection leads to poor performance of the device. The EIL should have optical transparency, proper energy level, and high electron transport properties.

Some metal oxide NPs satisfy above properties for EIL in inverted bottom-emission OLEDs so we investigated various properties of ZnO NPs and SnO<sub>2</sub> NPs. In addition, we improved the performance of the inverted bottom-emission OLEDs using these metal oxide NPs as an EIL.

### **3.1 Properties of Metal Oxide Nanoparticles**

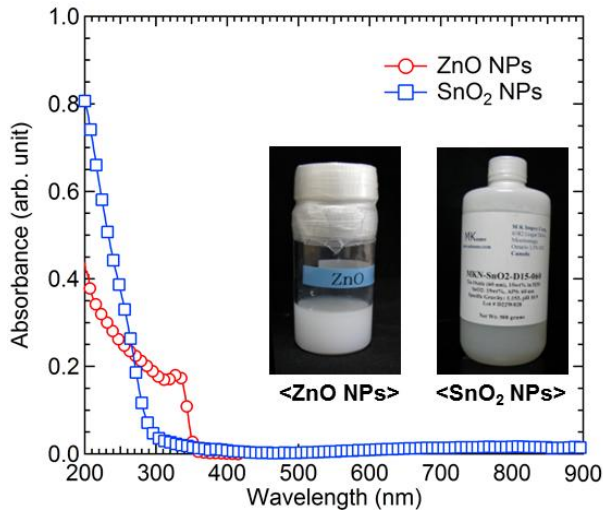
#### **3.1.1 Optical properties of metal oxide nanoparticles**

The optical transparency of the metal oxide NPs film is very important in the inverted bottom-emission OLEDs because the light is emitted from emitting layer (EML) pass through the metal oxide NPs layer. Figure 3.1 shows the optical absorption spectra of ZnO and SnO<sub>2</sub> NPs films. The inset of Figure 3.1 shows photographs of ZnO and SnO<sub>2</sub> NPs solutions. Both films are deposited on the quartz substrates using a spin-coating method. The thicknesses of ZnO and SnO<sub>2</sub>

NPs films are about 130 nm and 150 nm, respectively. Both metal oxide NPs films have no absorption in visible spectral region (380–780 nm). This means that both films are optically transparent even though their thicknesses are over 100 nm. From the long-wavelength optical-absorption edge ( $\lambda_{edge}$ ), we estimate the optical band gap ( $E_g$ ) of the material. The  $E_g$  of ZnO and SnO<sub>2</sub> NPs films are about 3.5 eV and 4.1 eV, respectively, from following equation.

$$E_g = \frac{hc}{q\lambda_{edge}} \quad (3.1)$$

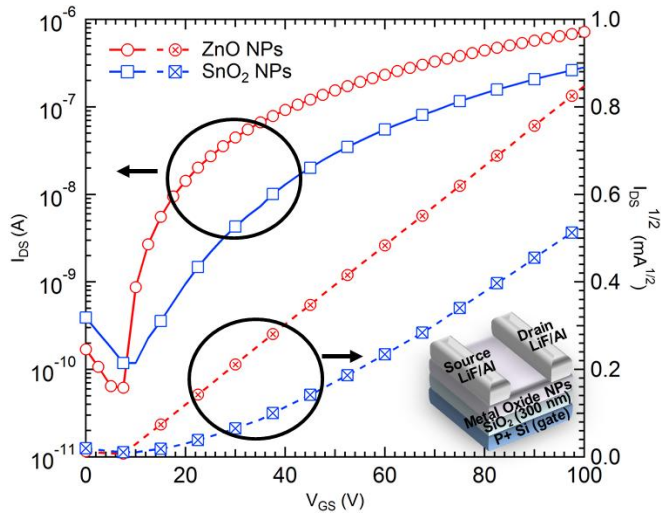
In this equation,  $h$ ,  $c$ , and  $q$  mean Planck's constant ( $6.626 \times 10^{-34}$  J·s), velocity of light in vacuum ( $3.0 \times 10^8$  m/s), and elementary charge ( $1.602 \times 10^{-19}$  J/eV). Consequently, both metal oxide NPs films can be utilized in OLEDs regardless of colors of emitted light due to their large optical band gaps.



**Figure 3.1** Optical absorption spectra of ZnO and SnO<sub>2</sub> NPs films. Inset: Photographs of ZnO and SnO<sub>2</sub> NPs solutions.

### 3.1.2 Electrical properties of metal oxide nanoparticles

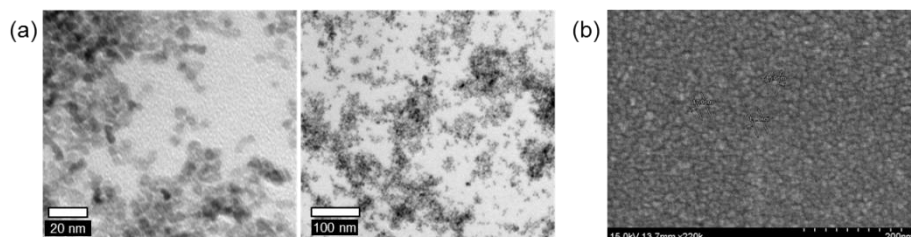
The electron transport properties of metal oxide NPs films are one of critical factors for using them as EILs. To investigate the electron mobility of metal oxide NPs films, we fabricated TFTs using metal oxide NPs layers as active layers as shown in the inset of Figure 3.2. Figure 3.2 shows transfer characteristics of the TFTs with metal oxide NPs. We can calculate electron mobility of metal oxide NPs films from the transfer curves. The electron mobility of ZnO and SnO<sub>2</sub> NPs layers are  $4.03 \times 10^{-4} \text{ cm}^2/\text{V s}$  and  $2.92 \times 10^{-4} \text{ cm}^2/\text{V s}$ , respectively. These values are relatively high electron mobility compared to commonly using organic electron transport materials, so they can be utilized as EILs in OLEDs.



**Figure 3.2** Transfer characteristics of the TFTs with metal oxide NPs.

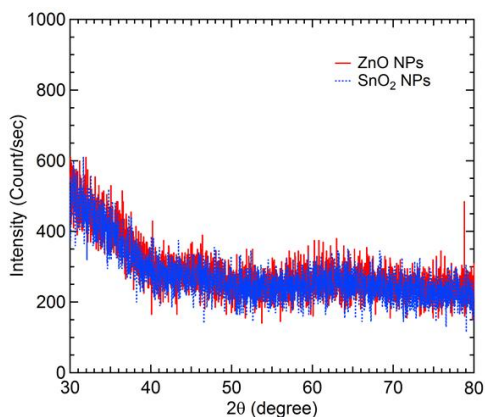
### 3.1.3 Other properties of metal oxide nanoparticles

Figure 3.3(a) and (b) show the TEM images of ZnO NPs and the SEM image of SnO<sub>2</sub> NPs, respectively. The particle sizes of ZnO and SnO<sub>2</sub> NPs are approximately 3–5 nm and 10–20 nm, respectively.



**Figure 3.3** (a) The TEM images of ZnO NPs with different resolutions and (b) the SEM image of SnO<sub>2</sub> NPs.

We also measured XRD patterns of metal oxide NPs films. Figure 3.4 shows XRD patterns of ZnO and SnO<sub>2</sub> NPs films on the quartz substrate. The patterns show no peak in whole scan region, which means that both metal oxide NPs films are amorphous.



**Figure 3.4** The XRD patterns of the ZnO and SnO<sub>2</sub> NPs films.

## **3.2 Inverted Bottom-Emission OLEDs with ZnO Nanoparticles**

We found that the ZnO NPs can be utilized as an EIL in the inverted bottom-emission OLEDs due to their wide optical band gap and good electron transport properties. We inserted the ZnO NPs layer between the ITO cathode and the ETL in the inverted bottom-emission OLEDs.

### **3.2.1 Device characteristics depending on ZnO nanoparticles thickness**

The inverted bottom-emission blue phosphorescent OLED structure and schematic energy level diagram are shown in Figure 3.5. We inserted the ZnO NPs layers with different thicknesses between the ITO cathode and the ETL [64]. The thicknesses ( $d$ ) of the ZnO NPs layers spin-coated from 2 mg/ml, 5 mg/ml, 10 mg/ml, 20 mg/ml, 30 mg/ml, and 40 mg/ml solutions are  $d=17$  nm, 23 nm, 30 nm, 45 nm, 55 nm, and 61 nm, respectively. We used 3TPYMB [65] as an ETL due to its high LUMO energy level. The mCP doped with FIrpic layer was used as a blue EML. The triplet energy level of blue phosphorescent dopant is higher than that of green or red phosphorescent dopant. Consequently, we selected a blue emitting device in this study because green and red phosphorescent emitting devices are usually working well if a blue phosphorescent emitting device is working well. A TAPC was selected as a

HTL and a MoO<sub>3</sub> was used as a hole injection layer (HIL) because of its good hole injection property in the inverted organic devices [66].

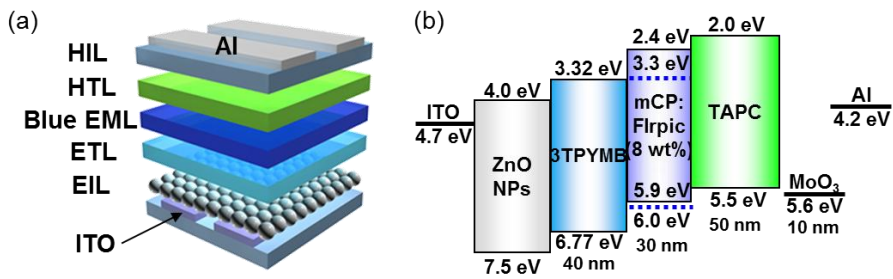


**Figure 3.5** (a) Device structure of the Flrpic-doped inverted bottom-emission blue phosphorescent OLEDs with an EIL of ZnO NPs and (b) a schematic energy level diagram.

Figure 3.6 shows the current density-voltage (J-V) and luminance-voltage (L-V) characteristics of the devices prepared with various ZnO NPs layer thicknesses. It is clear that the current density and luminance of the device increase significantly by the insertion of the ZnO NPs layer: The turn-on voltage decreases by about 4 V and the maximum luminance increases more than ten times with the addition of the ZnO NPs layer. For the device with a 45 nm thick ZnO NPs layer, the maximum luminance,  $L_{\max}$ , is 16917 cd/m<sup>2</sup> at 21.2 V and the driving voltage for 1000 cd/m<sup>2</sup>,  $V_{1000 \text{ nit}}$ , is 14.3 V while  $L_{\max}=1333 \text{ cd/m}^2$  at 27.3 V and  $V_{1000 \text{ nit}}=26.6 \text{ V}$  for the device without the ZnO NPs layer. This result indicates that the layer of ZnO NPs can inject electron very efficiently due to improved energy level matching at ITO/ZnO NPs/ETL (3TPYMB) interfaces as shown in Figure 3.5(b). As the thickness of

the ZnO NPs layer increases up to 45 nm, the current density and luminance of the device slightly increase but thicker thicknesses than 45 nm result in lower current density and luminance. This may be due to the fact that the injection and transport of electrons become better as the surface coverage of ZnO NPs on top of ITO becomes better with increasing ZnO NPs layer thickness up to 45 nm and then the resistance of ZnO NPs layer increases as the thickness of ZnO NPs layer becomes thicker. The surface morphology of ZnO NPs layer will be discussed later as shown in Figure 3.8.

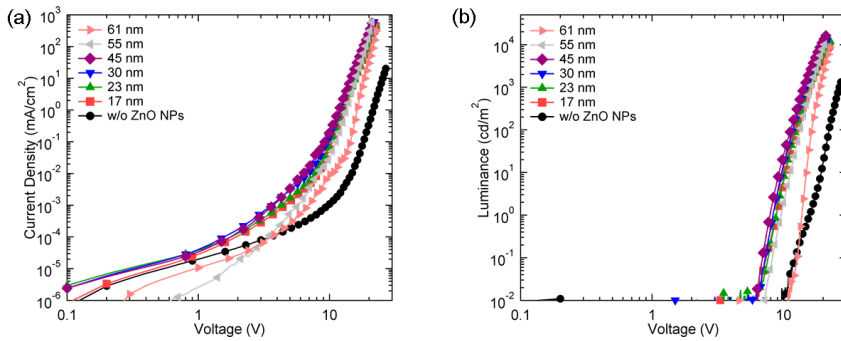
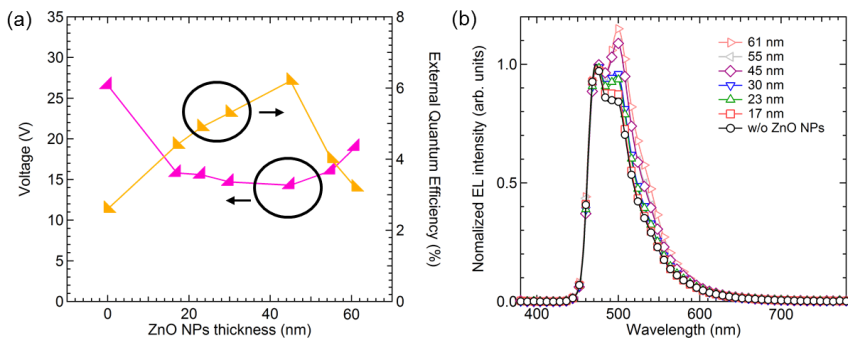


**Figure 3.6** (a) Current density-voltage (J-V) and (b) luminance-voltage (L-V) characteristics of the devices with different ZnO NPs layer thicknesses.

Figure 3.7(a) shows the driving voltages and EQEs of the devices with different ZnO NPs layer thicknesses at  $1000 \text{ cd/m}^2$ . The efficiencies are much higher for the devices with the ZnO NPs layer compared with the device without the ZnO NPs layer and they increase as the ZnO NPs layer thickness increases up to 45 nm and then decrease. The driving voltages of devices decrease as the ZnO NPs layer thickness increases up to 45 nm and then

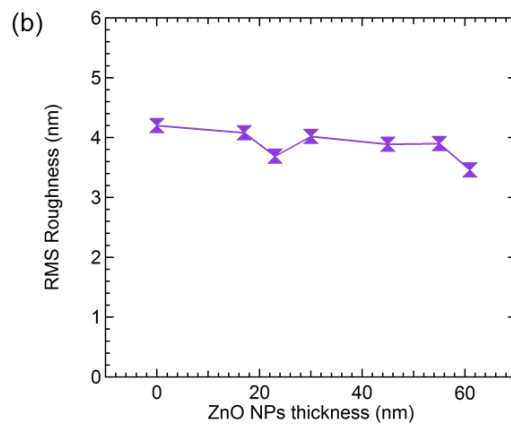
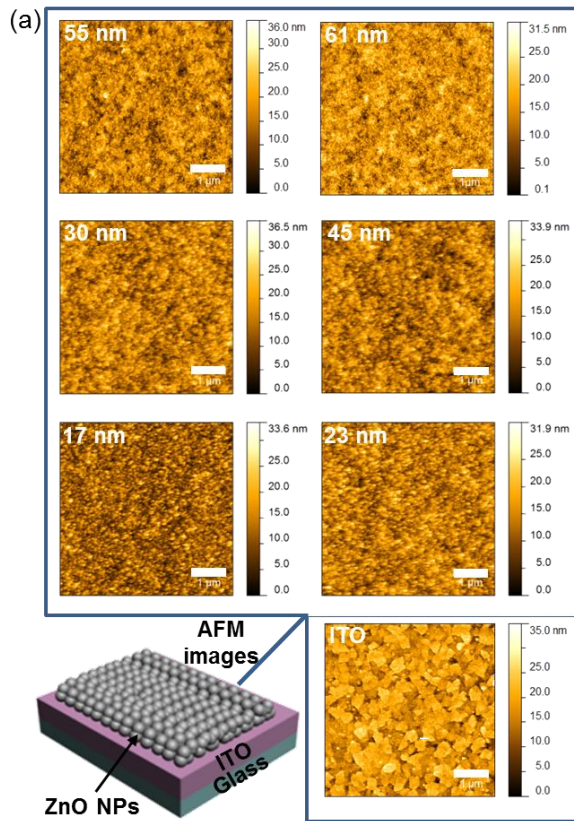
increase. As more electrons are injected to the ETL in the devices with ZnO NPs layer, electron-hole balance becomes to be improved and hence the quantum efficiency increases.

Figure 3.7(b) shows the EL spectra, normalized at the main emission peak at  $\sim 472$  nm, for the devices with different ZnO NPs layer thicknesses at a current density of  $J=5.1$  mA/cm<sup>2</sup>. The device without the ZnO NPs layer shows the typical EL spectrum of FIrpic emission where the emission peak at  $\sim 472$  nm is larger than the vibronic peak at longer wavelength. In comparison, the long-wavelength EL peak increases relatively with the EL peaks slightly shifted to longer wavelengths as the ZnO NPs thicknesses increase. This can be attributed to the optical interference effects [67]. The interference effects depend on the ZnO NPs layer thicknesses and change the spectral characteristics of the EL emission.



**Figure 3.7** (a) Driving voltages and EQEs at 1000 cd/m<sup>2</sup> and (b) normalized EL spectra of the devices with different ZnO NPs layer thicknesses at the same current density ( $J=5.1$  mA/cm<sup>2</sup>)

We investigated the surface morphology of the ZnO NPs layers with different thicknesses on the ITO coated glass substrates by using AFM. Figure 3.8 shows AFM images and the root-mean-square (RMS) roughnesses of ZnO NPs layer with different thicknesses and ITO. The roughness of ITO coated glass substrate is slightly reduced by depositing ZnO NPs. The roughness of ZnO NPs layer decreases as the thickness of ZnO NPs layer increases because of improved surface coverage. This result indicates that both surface coverage and thickness of ZnO NPs layer are important for efficient inverted bottom-emission OLEDs.



**Figure 3.8** (a) AFM images (image size is  $5 \mu\text{m} \times 5 \mu\text{m}$ ) and (b) the RMS roughnesses of the layers of ZnO NPs with different thicknesses.

We also measured the change of energy level of ZnO NPs layer as the thickness of ZnO NPs layer change by using UPS. Figure 3.9 shows UPS spectra of ZnO NPs layers with different thicknesses. The plot represents the full valence spectrum recorded under He II (21.22 eV) excitation. Vertical lines mark the onset of photoemission, one of the valence features as a function of thickness. A shift of these features towards higher binding energy occurs as the ZnO NPs concentration increases, indicating a corresponding shift of the energy level. The onset of the ZnO NPs layer with 2 mg/ml is nearly same with that of the ZnO NPs layer with 5 mg/ml and the onset of the ZnO NPs layer with 10 mg/ml is shifted to higher binding energy. The onset of the ZnO NPs layer with 20 mg/ml is nearly same with that of the ZnO NPs layer with 30 mg/ml and 40 mg/ml. As the concentration of ZnO NPs layer increases, the valence band energy level of ZnO NPs layer goes down. In other words, energy level difference ( $\Delta E1$ ) between ITO and ZnO NPs layer decreases and energy level difference ( $\Delta E2$ ) between ZnO NPs layer and ETL increases. As the energy barrier between ITO and ZnO NPs layer is reduced, more electrons can be injected to ZnO NPs layer. The energy level difference between ZnO NPs layer with 5 mg/ml and 10 mg/ml and between 10 mg/ml and 20 mg/ml are about 0.24 eV and 0.12 eV, respectively. In other words, the current and luminance increase as the injected electrons increases due to reduced energy barrier between ITO and ZnO NPs layer. However, the devices using ZnO NPs layer with 30 mg/ml and 40 mg/ml show low current and luminance due to increased resistance from thick thickness and same energy barrier with 20 mg/ml. Therefore, energy level and thickness of ZnO

NPs layer are significant factors for high performance inverted structure OLEDs.

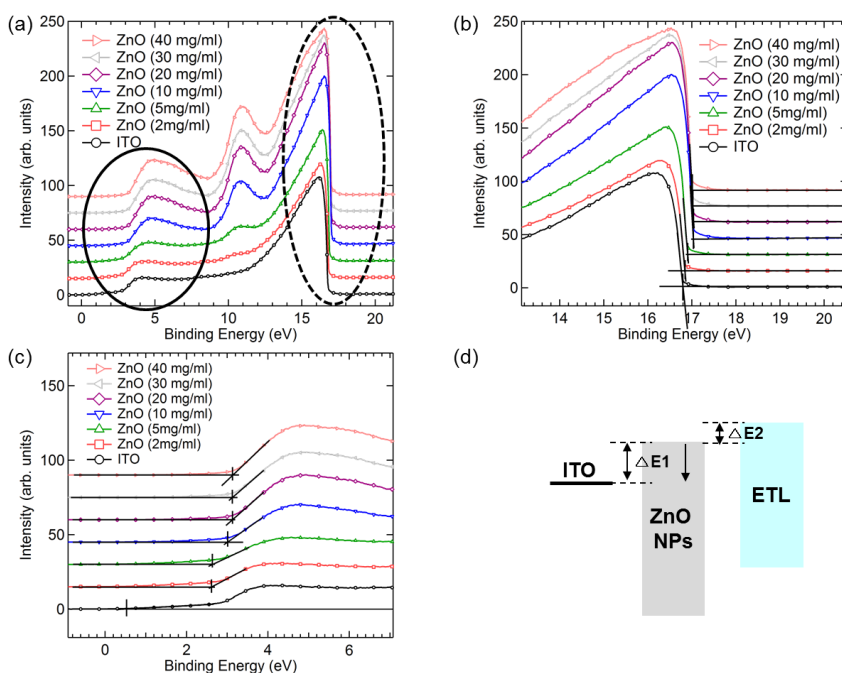


**Figure 3.9** (a) UPS spectra of the ZnO NPs layers with different concentrations, (b) expanded image of the dashed ellipse in (a), (c) expanded image of the solid ellipse in (a), and (d) schematic energy level diagram of cathode, EIL, and ETL.

### 3.2.2 Device characteristics depending on ETL thickness

We change the ETL thickness in the inverted bottom-emission OLEDs with device structure shown in Figure 3.5. The thicknesses of 3TPYMB are 0 nm, 20 nm, 40 nm, 60 nm, 80 nm, and 100 nm. Figure 3.10(a) shows the J-V characteristics of the devices with different ETL thicknesses. The current

density decreases as the thickness of the ETL increases due to low conductivity of 3TPYMB. The luminance of the devices also have similar tendency of current density. However, the luminance of the device without ETL is slightly lower than that of the device with 20 nm of ETL thickness. The EML in the device without ETL is directly connected to the ITO cathode, and this leads to the exciton quenching in the EML due to high electric field near the ITO electrode.

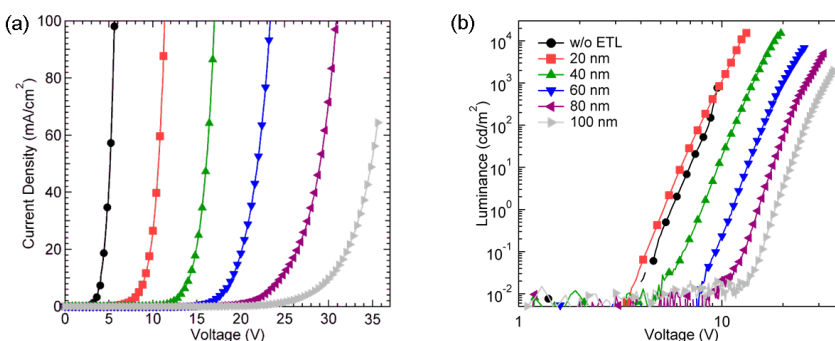


**Figure 3.10** (a) J-V and (b) L-V characteristics of the inverted bottom-emission blue phosphorescent OLEDs with different ETL thicknesses.

Figure 3.11(a) shows the driving voltages and EQEs of the devices with different ETL thicknesses at 1000 cd/m<sup>2</sup>. The driving voltage of the device increases as the thickness of the device increases but the efficiency of the device shows the highest value at the ETL thickness of 40 nm. It indicates that proper thickness exists for low driving voltage and high efficiency.

Figure 3.11(b) shows the EL spectra, normalized at the main emission peak at ~472 nm, for the devices with different ETL thicknesses at a current

density of  $J=5.1 \text{ mA/cm}^2$ . The EL spectrum of the device without ETL was measured at a current density of  $J=1020 \text{ mA/cm}^2$  due to its low luminance at low current density. As the thickness of ETL changes, the long-wavelength EL peak and full-width-half-maximum (FWHM) change. This tendency is similar to that of the devices with different ZnO thicknesses as shown in 3.7(b). This can also be attributed to the optical interference effects [67]. The interference effects depend on the ETL thicknesses and change the spectral characteristics of the EL emission.

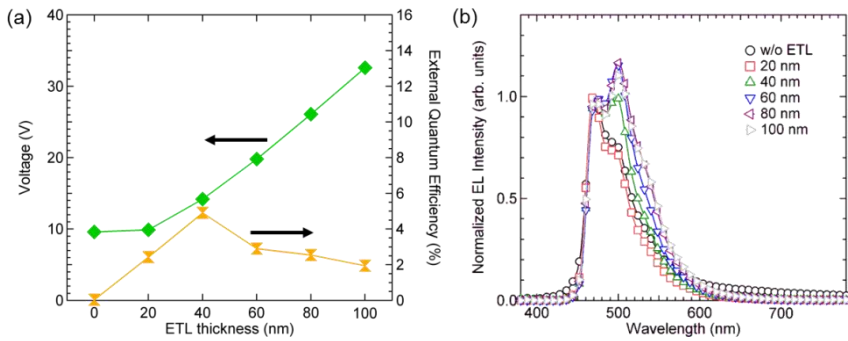


**Figure 3.11** (a) Driving voltages and EQEs at  $1000 \text{ cd/m}^2$  and (b) normalized EL spectra of the devices with different ETL thicknesses at the same current density ( $J=5.1 \text{ mA/cm}^2$ ).

### 3.2.3 Device characteristics depending on electron transport material

The LUMO energy level of ETL is very important to inject electrons from EIL to ETL efficiently in the inverted bottom-emission OLEDs. In this part, we

compared [68] 3TPYMB with BCP [69] as ETLs. The device structure is same with that of Figure 3.5 and the thickness of ZnO NPs layer is approximately 45 nm.

Figure 3.12(a) compares current density-voltage-luminance (J-V-L) characteristics of the inverted bottom-emission blue phosphorescent OLEDs with two different ETLs. The device with 3TPYMB as the ETL has much higher current density and luminance at the same voltage than the device with BCP. The turn-on voltage of the device with 3TPYMB is about 2 V lower than the device with BCP. Because the LUMO energy level of the BCP is approximately 0.3 eV lower than that of 3TPYMB, it is difficult to inject the electron from ZnO NPs to ETL in the device with BCP compared with the device with 3TPYMB.

Figure 3.12(b) compared the EQE and LCE of the devices with different ETLs. The efficiencies at low current density ( $J < 20 \text{ mA/cm}^2$ ) are much higher for the device with 3TPYMB than the device with BCP. The peak efficiencies of the device with 3TPYMB are 8.2 % and 16.5 cd/A at  $0.57 \text{ mA/cm}^2$ . Because the 3TPYMB can easily inject electrons from the EIL to the ETL than the BCP, electron-hole balance increases, resulting in higher efficiency. Furthermore, the 3TPYMB has much higher HOMO and triplet energy level ( $T_1=2.95 \text{ eV}$ ) [65] than the BCP ( $T_1=2.6 \text{ eV}$ ) [69]. This also contributes to the higher efficiency of the device with 3TPYMB. However, the device with 3TPYMB exhibits severe efficiency roll-off and, as a result, the device with BCP shows higher efficiency in the high current density region. In addition, the maximum luminance of the device with BCP is higher

than that of the device with 3TPYMB. These results imply that the triplet-triplet (T-T) annihilation [70] or triplet-polaron quenching may occur more seriously for the device with 3TPYMB due to better hole blocking ability and confinement of triplet excitons in the EML.

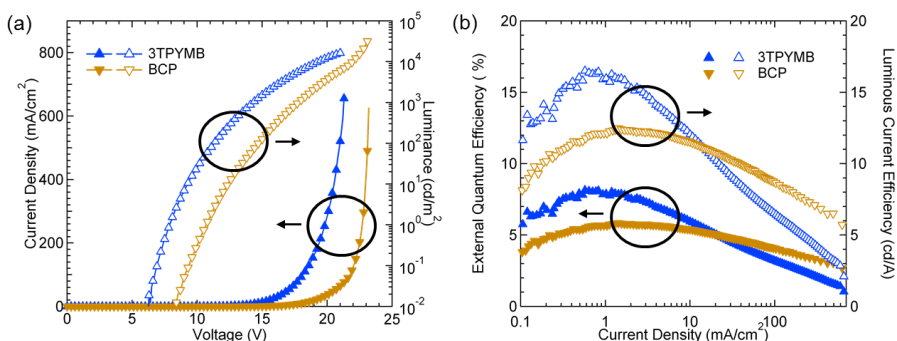


**Figure 3.12** (a) J-V-L and (b) EQE, LCE vs J characteristics for the inverted bottom-emission blue phosphorescent OLEDs with different ETLs.

### 3.2.4 Device characteristics depending on types of ZnO

We compared the ZnO NPs layer with the ZnO layer obtained by the sol-gel method as an EIL in the inverted bottom-emission OLEDs. We fabricated green phosphorescent inverted bottom-emission OLEDs using the ZnO as an EIL as shown in Figure 3.13(a). We applied heat to the ZnO precursor films with temperature of 100°C, 200°C, and 300°C for the formation of the ZnO film. The ZnO films with 200°C and 300°C thermal annealing show typical absorption spectra of ZnO as shown in Figure 3.13(b). However, the ZnO film with 100°C thermal annealing does not show any absorption because low

temperature cannot make a ZnO film from ZnO precursor solutions. From the long-wavelength optical-absorption edge and UPS data, we can calculate the energy levels of the ZnO films with different thermal annealing temperatures as shown in the inset of Figure 3.13(b). The conduction band energy levels of ZnO films are similar with that of the ZnO NPs film (See Figure 3.5(b))

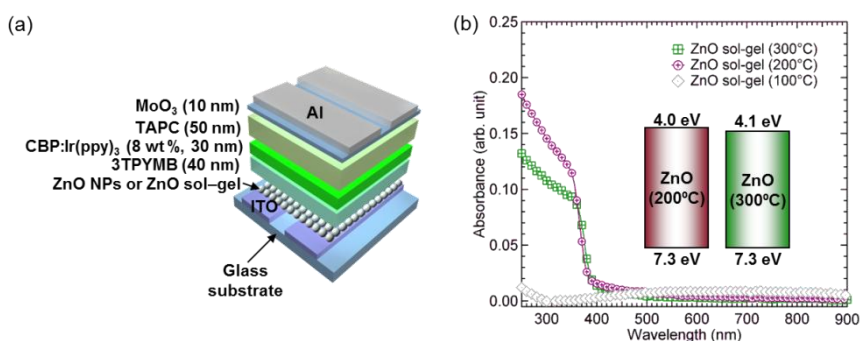


**Figure 3.13** (a) Device structure of the green phosphorescent inverted bottom-emission OLEDs with different types of ZnO layer and (b) optical absorption spectra of the ZnO films with different thermal annealing temperatures obtained by the sol-gel method. Inset: schematic energy level diagrams of the ZnO layers with different thermal annealing temperatures.

Figure 3.14 shows J-V and L-V characteristics of the green phosphorescent inverted bottom-emission OLEDs with different types of ZnO as EILs. The device with ZnO NPs layer exhibits much higher current density and luminance than the device with ZnO layer obtained by sol-gel method. And the device with 300°C treated ZnO film has higher current density and luminance than the device with 200°C treated ZnO film at the same voltage.

The device with 100°C treated ZnO film is not working, which means very low current and no luminance in whole voltage scan region due to unformatted ZnO film at 100°C. The current density at 20 V and driving voltage for 1000 cd/m<sup>2</sup> of the device with ZnO NPs, ZnO (300°C), and ZnO (200°C) are 273 mA/cm<sup>2</sup>, 62 mA/cm<sup>2</sup>, 25 mA/cm<sup>2</sup> and 12.1 V, 14.9 V, 16.4 V, respectively. This result implies that the ZnO NPs layer is better than the ZnO films obtained from sol-gel method in the inverted bottom-emission OLEDs and high thermal annealing temperature are required for efficient ZnO film with sol-gel method as an EIL.

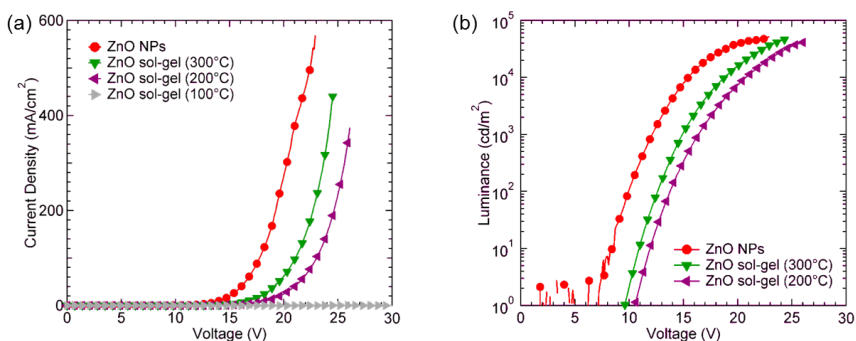


**Figure 3.14** (a) J-V and (b) L-V characteristics of the green phosphorescent inverted bottom-emission OLEDs with different types of ZnO as EILs.

Figure 3.15(a) shows EQEs of the devices with different types of ZnO layers as a function of luminance. The device with the ZnO NPs layer has much higher efficiency than the devices with ZnO layers obtained by sol-gel method. The EQEs at 1000 cd/m<sup>2</sup> of the devices with ZnO NPs, ZnO (300°C), and ZnO (200°C) are about 15.1 %, 12.5 %, and 11.2 %, respectively.

Figure 3.15(b) exhibits the EL spectra, normalized at the main emission peak at  $\sim 513$  nm, for the devices with different types of ZnO layer at a current density of  $J=5.1$  mA/cm<sup>2</sup>. All devices show nearly same EL spectra which are typical EL spectra of Ir(ppy)<sub>3</sub> emission. In other words, used ZnO EILs rarely affect the EL spectrum of the green phosphorescent inverted bottom-emission OLEDs.

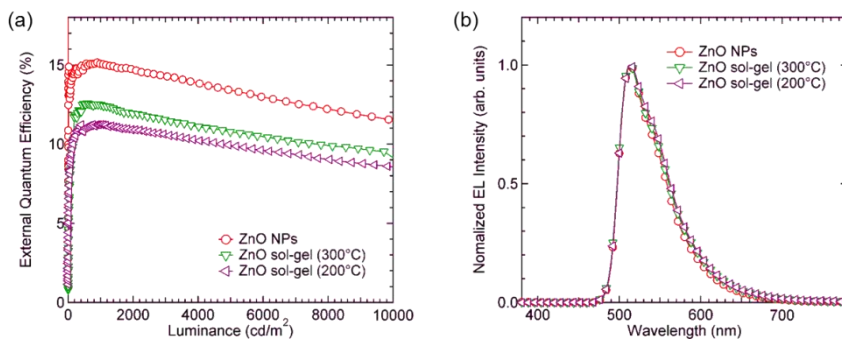


**Figure 3.15** (a) EQE-L characteristics and (b) normalized EL spectra of the devices with different types of ZnO layers at the same current density ( $J=5.1$  mA/cm<sup>2</sup>)

To investigate the difference between ZnO NPs layer and ZnO layer obtained by sol-gel method, we analyzed surface morphology of the ZnO layers with different thermal annealing temperatures by using an AFM. Figure 3.16 shows the AFM images of the ITOs and the ZnO films on the ITOs with different thermal annealing temperatures. The surface morphologies of ITOs are nearly same regardless of the annealing temperature. The RMS roughness of ITOs with 100°C, 200°C, and 300°C are 2.43 nm, 2.47 nm, and 2.51 nm, respectively. However, the surface morphologies of ZnO films on the ITOs are different as the annealing temperature changes. The

surface of ZnO precursor layer is slightly rugged at 100°C and changes to very rough surface like a gorge at 200°C. The RMS roughness of ZnO films with 100°C and 200°C are 7.84 nm and 18.6 nm, respectively. However, the surface of the ZnO film becomes smooth at 300°C. It is about 2.12 nm of RMS roughness which is lower than that of the ITO. This result may be caused by the change process from the ZnO precursor to the ZnO. We are required to more study about this result. As a result, the roughness of the ZnO film is not a critical factor to make difference between the device with the ZnO NPs layer and the device with the ZnO layer obtained by sol-gel method because the roughness of ZnO NPs layer is about 3.9 nm which is higher than that of the ZnO film with 300°C thermal annealing. We estimated electron mobility of ZnO films with 200°C and 300°C thermal annealing by using the TFTs with same structure of the inset of Figure 3.2. The electron mobility of the ZnO films with 200°C and 300°C thermal annealing are  $3.12 \times 10^{-5} \text{ cm}^2/\text{V}\cdot\text{s}$  and  $2.12 \times 10^{-4} \text{ cm}^2/\text{V}\cdot\text{s}$ , respectively. These lower electron mobility than that of the ZnO NPs may lead to the lower performance of the device with ZnO films obtained by sol-gel method than that of the device with ZnO NPs layer.

We also measured the XRD patterns of ZnO films on the quartz substrates with different thermal annealing temperatures as shown in Figure 3.17. The patterns show no peak in whole scan region, which means that all ZnO films are amorphous regardless of thermal annealing temperature.

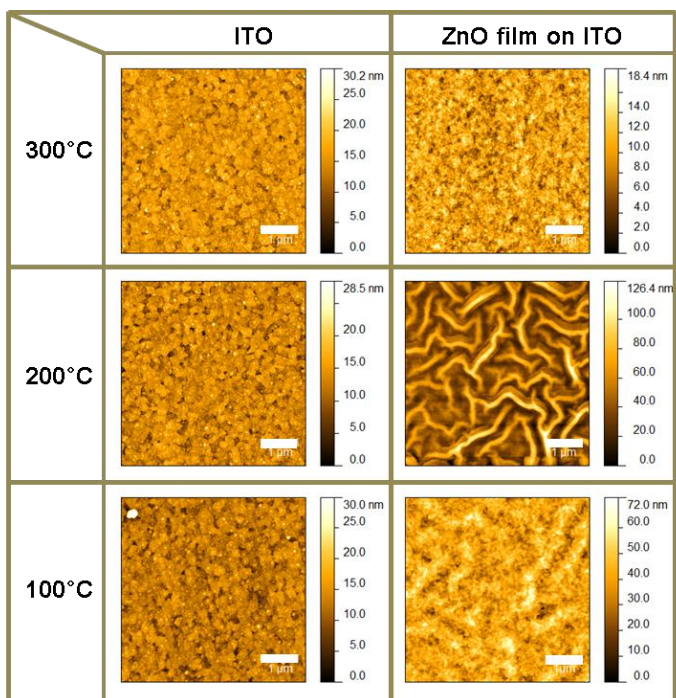


**Figure 3.16** AFM images of the ITOs and the ZnO films on the ITOs with different thermal annealing temperatures (The image size is  $5 \times 5 \mu\text{m}^2$ ).

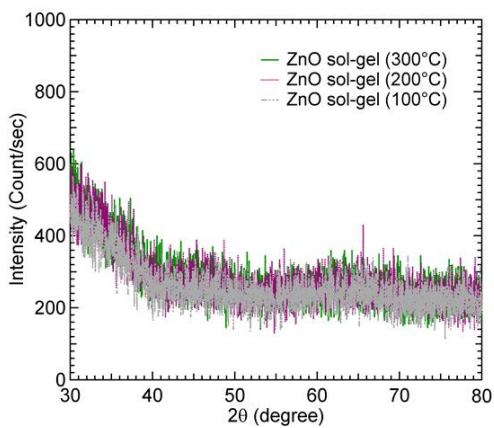


**Figure 3.17** XRD patterns of the ZnO films with different thermal annealing temperatures.

### **3.2.5 Angular dependence of the EL spectra in the inverted bottom-emission OLEDs using ZnO nanoparticles**

The angular dependence of the EL spectra is an important factor for full-color display because different EL spectra as viewing angle changes cause color distortion with different viewing angle in the full-color display. In the case of top-emission OLEDs, viewing angle problem exists due to the microcavity effect from both metal anode and cathode. In contrast, bottom-emission OLEDs have no viewing angle problem because the ITO which is usually used as a transparent electrode has very low optical reflectivity.

We measured the angular dependence of irradiance and EL spectra of the inverted bottom-emission green phosphorescent OLEDs with the ZnO NPs layer as an EIL and without the ZnO NPs layer as shown in Figure 3.18. The angular irradiance characteristic of the device is nearly Lambertian emission profile irrespective of ZnO NPs layer insertion. In addition, the EL spectra of the devices at different viewing angles also show little spectrum shift from the normal direction to 75° off the direction. Therefore, the ZnO NPs layer can be utilized for the full-color OLED displays without the viewing angle problem.

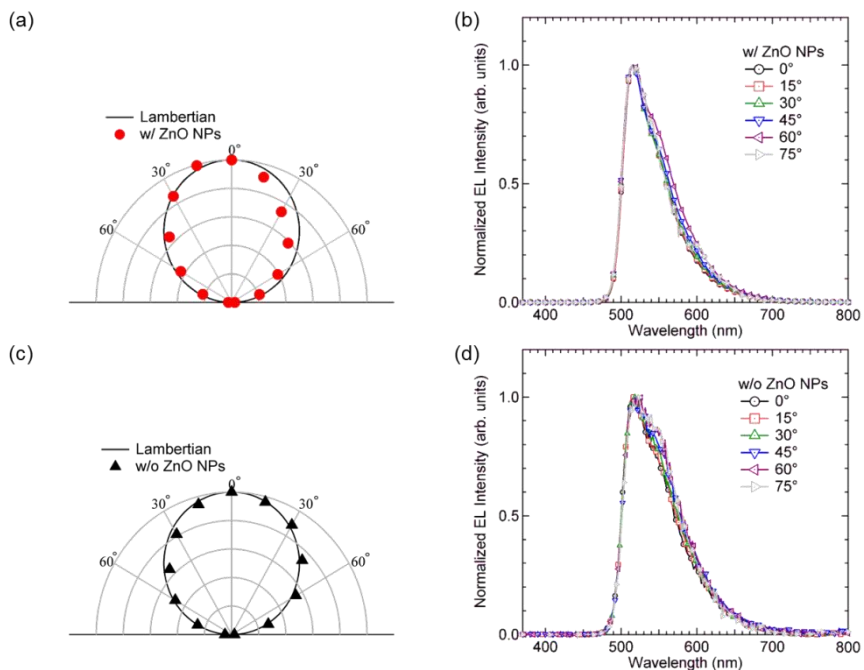


**Figure 3.18** Angular distribution of radiation irradiance (normalized to the  $0^\circ$  irradiance) and the EL spectra of the green phosphorescent inverted bottom-emission OLED (a), (b) with the ZnO NPs layer (20 mg/ml) and (c), (d) without the ZnO NPs layer with different measuring angles.

### **3.3 Inverted Bottom-Emission OLEDs with SnO<sub>2</sub> Nanoparticles**

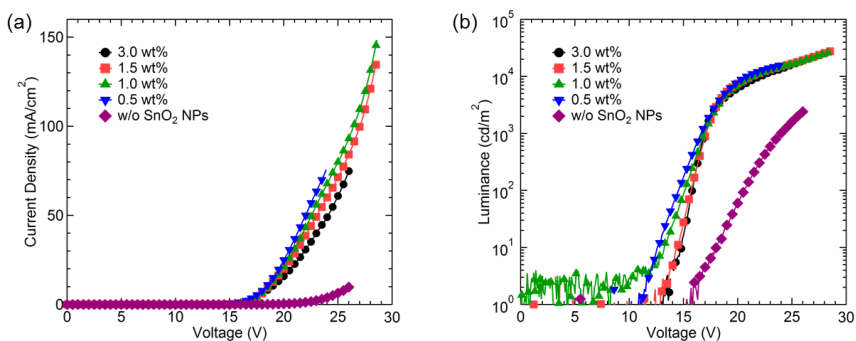
In this part, we utilized SnO<sub>2</sub> NPs as an EIL in the inverted bottom-emission OLEDs due to its high transparency and good electron transport properties. Furthermore, it is known that SnO<sub>2</sub> has a low sensitivity to UV degradation because of its large band gap [71]. The SnO<sub>2</sub> layer is already used in quantum dot LEDs but the radio frequency magnetron sputter process which requires high cost is utilized to deposit SnO<sub>2</sub> layer [72]. The SnO<sub>2</sub> NPs layer used in this work is deposited using solution process which is a spin-coating method and not required additional thermal annealing or other treatments. It means that the process for SnO<sub>2</sub> NPs layer is simple and low-cost.

#### **3.3.1 Device characteristics depending on SnO<sub>2</sub> nanoparticles thickness**

We fabricated green phosphorescent inverted bottom-emission OLEDs with different thicknesses of SnO<sub>2</sub> NPs layers. The device structure is same with Figure 3.13(a) and the SnO<sub>2</sub> NPs layer is inserted instead of the ZnO layer. The thicknesses of the SnO<sub>2</sub> NPs layers spin-coated from 1.0 wt%, 1.5 wt%, and 3.0 wt% solutions are 15 nm, 17 nm, and 27 nm, respectively. The

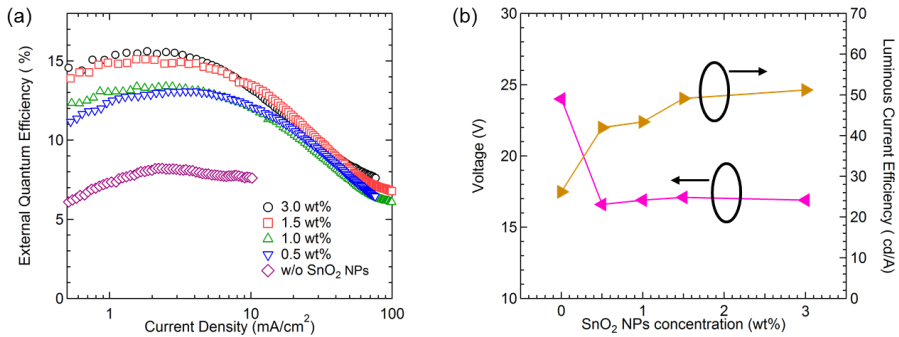
thickness of the 0.5 wt% SnO<sub>2</sub> NPs layer cannot be measured because it is too thin to measure.

Figure 3.19 shows the J-V and L-V characteristics of the devices with different SnO<sub>2</sub> NPs concentrations. It is clear that the current density and luminance of the device increase significantly by the insertion of the SnO<sub>2</sub> NPs layer compared with the device without the SnO<sub>2</sub> NPs layer. For the device with a 1.5 wt% SnO<sub>2</sub> NPs layer, the maximum luminance is 27575 cd/m<sup>2</sup> at 28.5 V and the driving voltage for 1000 cd/m<sup>2</sup> is 17.1 V while those values are 2512 cd/m<sup>2</sup> at 26.1 V and 24 V, respectively, for the device without the SnO<sub>2</sub> NPs layer. This result indicates that the insertion of SnO<sub>2</sub> NPs layer can inject electron efficiently from the ITO to the 3TPYMB layer. The current density and luminance slightly decrease at the same voltage as the concentration of SnO<sub>2</sub> NPs increases because total thickness of the device increases. The maximum luminance of the device with 3.0 wt% SnO<sub>2</sub> NPs layer is also lower than that of the device with 1.5 wt% SnO<sub>2</sub> NPs layer. In other words, the driving voltage increases and current decreases as the thickness of SnO<sub>2</sub> NPs layer increases.



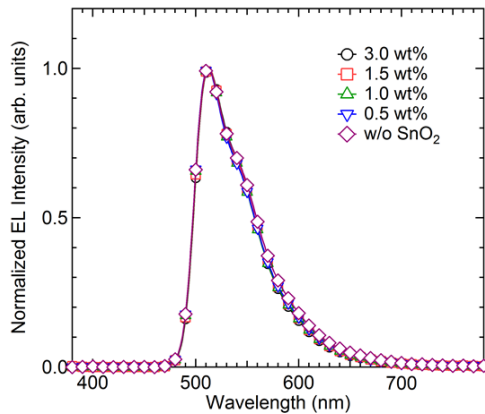
**Figure 3.19** (a) J-V and (b) L-V characteristics of the devices with different SnO<sub>2</sub> NPs concentrations.

Figure 3.20(a) shows that the devices with SnO<sub>2</sub> NPs layers have much higher EQEs compared with that of the device without the SnO<sub>2</sub> NPs layer. The device with the 3.0 wt% SnO<sub>2</sub> NPs layer shows the highest efficiencies of 15.6 % and 51.1 cd/A at 1000 cd/m<sup>2</sup>, which is about two times higher than that of the device without the SnO<sub>2</sub> NPs layer. As more electrons are injected to the ETL in the devices with SnO<sub>2</sub> NPs layer, electron-hole balance is enhanced and thus the quantum efficiency increases. We also compare the driving voltage and the LCE at 1000 cd/m<sup>2</sup> as a function of SnO<sub>2</sub> NPs concentrations as shown in Figure 3.20(b). It is obvious that the driving voltage is decreased and the efficiency is enhanced by using the SnO<sub>2</sub> NPs as an EIL. The driving voltage decreases and the LCE increases as the concentration of SnO<sub>2</sub> NPs increases. Considering the J-V-L characteristics and the efficiencies, the device with 1.5 wt% SnO<sub>2</sub> NPs layer shows the best performance among the devices with different SnO<sub>2</sub> NPs layer thicknesses.



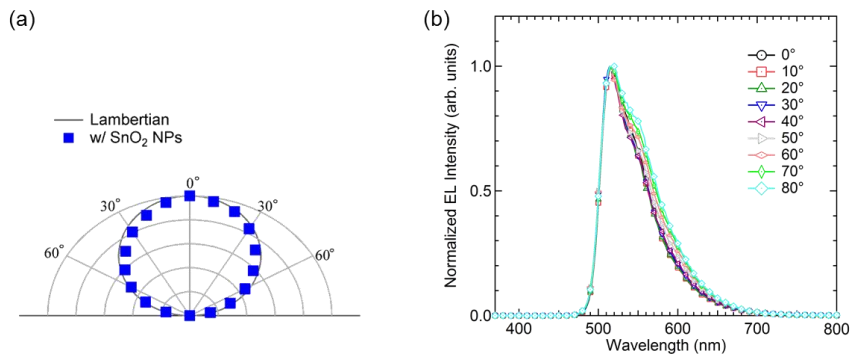
**Figure 3.20** (a) EQE-J characteristics and (b) driving voltages and LCEs at 1000  $\text{cd/m}^2$  as a function of the  $\text{SnO}_2$  NPs concentrations.

Figure 3.21 shows the EL spectra, normalized at the main emission peak ( $\sim 512$  nm), for the devices with different  $\text{SnO}_2$  NPs concentrations at a current density of  $J=5.1 \text{ mA/cm}^2$ . All the EL spectra are same shape regardless of the  $\text{SnO}_2$  NPs concentrations. This means that the  $\text{SnO}_2$  NPs layer scarcely affect the EL spectrum of the inverted bottom-emission OLEDs.



**Figure 3.21** Normalized EL spectra of the devices with different  $\text{SnO}_2$  NPs concentrations at the same current density ( $J=5.1 \text{ mA/cm}^2$ ).

We also measured the angular dependence of irradiance and EL spectra of the device with the SnO<sub>2</sub> NPs layer as an EIL as shown in Figure 3.22. The angular irradiance characteristic of the device with the SnO<sub>2</sub> NPs layer is nearly Lambertian emission profile. In addition, the EL spectra of the device with the SnO<sub>2</sub> NPs layer at different viewing angles shows little spectrum shift from the normal direction to 80° off the direction. Consequently, the SnO<sub>2</sub> NPs layer can be utilized for the OLED displays without the viewing angle problem.



**Figure 3.22** (a) Angular distribution of radiation irradiance (normalized to the 0° irradiance) and (b) the EL spectra of the green phosphorescent inverted bottom-emission OLED with 1.5 wt% SnO<sub>2</sub> NPs layer with different measuring angles.

### 3.3.2 Surface morphology and energy level of SnO<sub>2</sub> NPs layer

We found that the device performances are different as the thickness of SnO<sub>2</sub> NPs layer changes. So we investigated the surface morphology and the energy level of SnO<sub>2</sub> NPs layer as the thickness of the SnO<sub>2</sub> NPs layer changes.

First, we investigated the surface morphology of SnO<sub>2</sub> NPs layers with different concentrations on the ITO coated glass substrate by using an AFM. Figure 3.23 shows AFM images and the RMS roughnesses of the SnO<sub>2</sub> NPs layers with different concentrations. The roughness of ITO coated glass substrate is reduced by depositing the SnO<sub>2</sub> NPs. The roughness of the SnO<sub>2</sub> NPs layer decreases as the concentration of SnO<sub>2</sub> layer increases because of improved surface coverage.

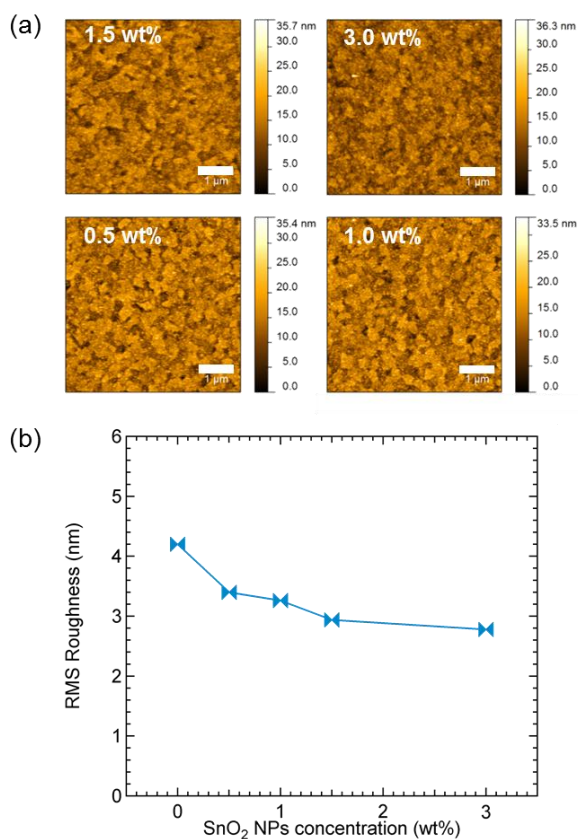


**Figure 3.23** (a) AFM images (image size is 5 μm × 5 μm) and (b) RMS roughnesses of the layers of SnO<sub>2</sub> NPs with different thicknesses.

We also measured the change of energy level of the SnO<sub>2</sub> NPs layer as the concentrations of SnO<sub>2</sub> NPs layer change by using UPS. Figure 3.24 shows UPS spectra of the SnO<sub>2</sub> NPs layers with different concentrations. The plot represents the full valence spectrum recorded under He II (21.22 eV) excitation. Vertical lines mark the onset of photoemission, one of the valence features as a function of doping concentrations. A shift of these features towards higher binding energy occurs as the SnO<sub>2</sub> NPs concentration increases, indicating a corresponding shift of the energy level. The onset of the SnO<sub>2</sub> NPs layer with 0.5 wt% is nearly same with that of the the SnO<sub>2</sub> NPs layer with 1.0 wt% and the onset of the SnO<sub>2</sub> NPs layer with 1.5 wt% is nearly same with that of the SnO<sub>2</sub> NPs layer with 3.0 wt% and 15 wt%. This tendency is similar to the EQE tendency of the devices with the SnO<sub>2</sub> NPs layer. As the concentration of the SnO<sub>2</sub> NPs increases, the valence band energy level of the SnO<sub>2</sub> NPs layer goes down. In other words, energy level difference ( $\Delta E3$ ) between the ITO and the SnO<sub>2</sub> NPs layer decreases and energy level difference ( $\Delta E4$ ) between the SnO<sub>2</sub> NPs layer and the ETL increases. The measured energy levels of SnO<sub>2</sub> NPs layer are approximately 3.6 eV for the conduction band and 7.7 eV for the valence band. The energy barrier between the ITO and the SnO<sub>2</sub> NPs layer is higher than that between the ITO and the ZnO NPs layer. This may cause higher turn-on voltage of the device with SnO<sub>2</sub> NPs layer compared with the device with ZnO NPs layer. Therefore, the energy level of metal oxide NPs layer is a critical factor for high performance inverted structure OLEDs.

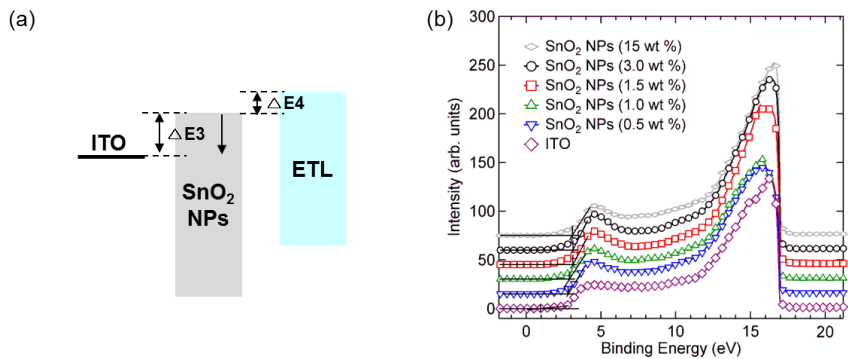


**Figure 3.24** (a) Schematic energy level diagram of the cathode, EIL, and ETL, and (b) UPS spectra of the SnO<sub>2</sub> NPs layers with different concentrations.

## Chapter 4. OLEDs with P-type Doped Hole Transport Layer

### 4.1 White OLEDs using P-type Doped HTL

To achieve high quantum efficiency in the phosphorescent OLEDs, charges and triplet excitons must be confined to the emission region of a device. Therefore, the hole transport material and electron transport material should have shallow LUMO and deep HOMO energy levels, respectively. In addition, they also have a higher triplet energy level than that of the emitting material. For example, a device with TAPC has much higher quantum efficiency than devices with other hole transport materials, such as  $\alpha$ -NPD and 4,4'-bis[N-(p-tolyl)-N-phenylamino]biphenyl (TPD), due to its higher triplet energy level compared with other hole transport materials [73].

To decrease the driving voltage of OLEDs, the potential energy barrier between the electrode and the organic material should be reduced and the carrier transport material should have high electrical conductivity. Electrical doping such as *p*-type doping and *n*-type doping can reduce the driving voltage of OLEDs because it decreases the contact resistance between the electrodes and organic materials as well as increases the electrical conductivity of organic materials due to increased charge amounts [74]. Recently, transition metal oxides such as MoO<sub>3</sub> and tungsten trioxides have

been widely used as *p*-type dopants to enhance hole injection and transport in the organic devices [75–80].

In this part, we investigate the optical and electrical properties of MoO<sub>3</sub> doped TAPC films with different doping concentrations. Based on these results, we fabricated trichromatic white OLEDs with red, orange, and blue emission layers. By employing a MoO<sub>3</sub> doped TAPC layer as a HTL, we improved the power efficiency and decreases the driving voltage of white OLEDs. In addition, the white OLEDs show a high CRI of about 86 with the CIE 1931 chromatic coordinates of (0.4303, 0.3893) and correlated color temperature (CCT) of 3008 K. The CCT is black body temperature emitting the same color, and warm light is 2800 K–3200 K, cool light is > 5000K.

#### **4.1.1 Optical property of MoO<sub>3</sub> doped TAPC layer**

Figure 4.1 shows the optical absorption spectra of MoO<sub>3</sub>, undoped TAPC, and MoO<sub>3</sub> doped TAPC films with different MoO<sub>3</sub> concentrations. All film thicknesses are 100 nm. The absorption spectrum of the undoped TAPC film shows an absorption peak at 310 nm and no absorption peaks between 400 nm and 900 nm. However, the optical absorption spectrum of the MoO<sub>3</sub> doped TAPC film shows an additional absorption peak at 703 nm, and the intensity of this new peak increases as the doping concentration of the MoO<sub>3</sub> increases, as shown in the inset of Figure 4.1. This new peak is absent in the optical absorption spectra of undoped TAPC and MoO<sub>3</sub> films. This result is similar to other *p*-type doping results discussed in other literatures, and they explain that

the new absorption peak is originated from the charge transfer (CT) complex between the hole transport material and dopant [79, 81, 82]. Therefore, the absorption peak at 703 nm in the MoO<sub>3</sub> doped TAPC film indicates the formation of CT complexes between the TAPC and the MoO<sub>3</sub>, resulting in *p*-type doping of the TAPC.

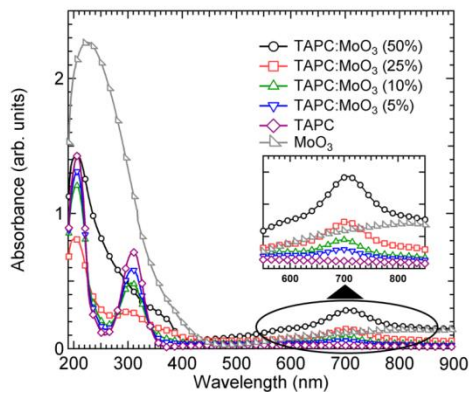


**Figure 4.1** Optical absorption spectra of MoO<sub>3</sub>, undoped TAPC, and MoO<sub>3</sub> doped TAPC films with different MoO<sub>3</sub> concentrations. Inset: increase of CT complex absorption peak (703 nm) as the MoO<sub>3</sub> concentration increases.

#### 4.1.2 Electrical property of MoO<sub>3</sub> doped TAPC layer

To investigate the enhancement of hole injection and transport in the MoO<sub>3</sub> doped TAPC film, we fabricated hole-only devices with device structures composed of ITO/TAPC:MoO<sub>3</sub> (x vol%, 100 nm)/Al (100 nm) and ITO/MoO<sub>3</sub> (5 nm)/TAPC:MoO<sub>3</sub> (x vol%, 100 nm)/MoO<sub>3</sub> (5 nm)/Al (100 nm). The MoO<sub>3</sub> layer (5 nm) can efficiently inject holes from the electrode to the organic layer

so we can find that the cause of current increase is whether the enhancement of hole injection or hole transport of the MoO<sub>3</sub> doped TAPC layer by comparing above two devices [76, 83]. Figure 4.2(a) shows the J-V characteristics of the hole-only devices with different MoO<sub>3</sub> concentrations. The devices with a MoO<sub>3</sub> doped layer exhibit dramatically enhanced hole injection and transport abilities with respect to the device with an undoped layer. In comparing devices with an undoped and a 5% MoO<sub>3</sub> doped layer, the current density of the device with the MoO<sub>3</sub> layer (5 nm) in the electrode is higher than that of the device without the MoO<sub>3</sub> layer (5 nm); however, the current density of the devices with doping concentrations above 10% is almost the same regardless of the insertion of the MoO<sub>3</sub> layer (5 nm). This result indicates that the hole injection barrier between ITO and the MoO<sub>3</sub> doped TAPC layer is similar to that between ITO and the MoO<sub>3</sub> layer when the doping concentration is greater than 10%. The current density of the device increases as the doping concentration increases. However, the current density of a 50% doped layer is slightly lower than that of a 25% doped layer. This result is different from those observed in the absorption spectra. This may be due to the fact that heavily doped MoO<sub>3</sub> reduces the hole mobility of the doped film. The decrease in hole mobility has previously been observed in MoO<sub>3</sub> doped N<sup>7</sup>-diphenyl-N,N<sup>7</sup>-bis(1-naphthyl)(1,1'-biphenyl)-4,4'-diamine (NPB) [84]. Figure 4.2(b) shows the electrical conductivities of the MoO<sub>3</sub> doped TAPC films as a function of MoO<sub>3</sub> doping concentration, which is derived from the ohmic regime of the J-V characteristics in Figure 4.2(a). The electrical conductivity of MoO<sub>3</sub> doped TAPC film increases as the MoO<sub>3</sub>

doping concentration increases. When the doping concentration is greater than 25%, the MoO<sub>3</sub> doped TAPC films exhibit similar electrical conductivities. The electrical conductivity of the undoped, 5%, 10%, 25%, and 50% MoO<sub>3</sub> doped TAPC films is approximately  $1.2 \times 10^{-8}$  S/cm,  $4.1 \times 10^{-7}$  S/cm,  $3.3 \times 10^{-6}$  S/cm,  $6.9 \times 10^{-6}$  S/cm, and  $6.2 \times 10^{-6}$  S/cm, respectively. These values are similar to the reported values for MoO<sub>x</sub> doped 4',4''-tri(N-carbazolyl)triphenylamine (TCTA) or NPB [75]. The above results indicate that MoO<sub>3</sub> doped TAPC films can be used as HTLs in OLEDs to reduce the driving voltage and to improve the power efficiency.

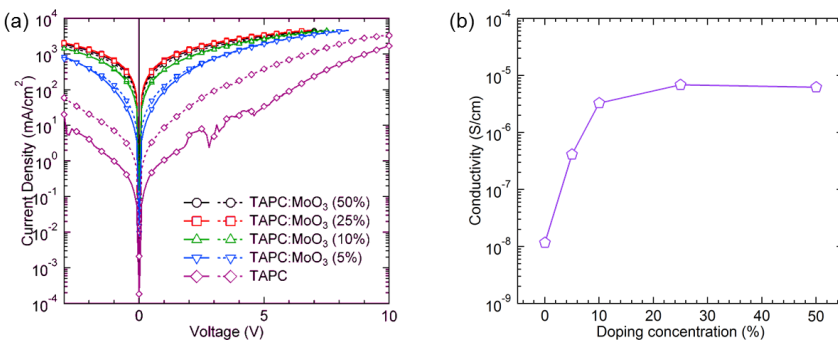


**Figure 4.2** (a) J-V characteristics of the hole-only devices with different MoO<sub>3</sub> concentrations (solid line: without MoO<sub>3</sub> (5 nm) layer in both electrodes; dashed line: with MoO<sub>3</sub> (5 nm) layer in both electrodes); (b) electrical conductivities of MoO<sub>3</sub> doped TAPC films with different doping concentrations.

### 4.1.3 Phosphorescent white OLEDs using p-type doped HTL

To investigate the effect of MoO<sub>3</sub> doped TAPC layer in the OLEDs, we have fabricated white OLEDs with MoO<sub>3</sub> doped TAPC layer. Figures 4.3(a) and (b) show the device structure and schematic energy level diagram of the phosphorescent white OLEDs, respectively. A MoO<sub>3</sub> doped TAPC film was used as an HTL as well as a HIL in the device. We changed the doping concentration from 5 vol% to 50 vol%. To prevent exciton quenching in the EML by the dopants in the HTL, we inserted an undoped TAPC film as a buffer layer between the MoO<sub>3</sub> doped TAPC layer and EML [85]. We used mCP as a host for the EML and three phosphorescent dopants which are Flrpic as a blue dopant, (Ir(BT)<sub>2</sub>(acac)) as an orange dopant [86], and (Ir(piq)<sub>2</sub>(acac)) as a red dopant [87]. We used 3TPYMB as an ETL because of its deep HOMO and high triplet energy level. This ETL can block holes and confine triplet excitons effectively [65, 88]. LiF and Al were used as an EIL and cathode, respectively. For comparison, we also fabricated white OLEDs with an undoped TAPC layer (30 nm) as an HTL and MoO<sub>3</sub> (10 nm) as an HIL instead of a MoO<sub>3</sub> doped TAPC layer (40 nm). Since the white OLEDs have three EMLs with different colors, we can easily find the variation of recombination region with MoO<sub>3</sub> doping concentrations compared with mono-color OLEDs.

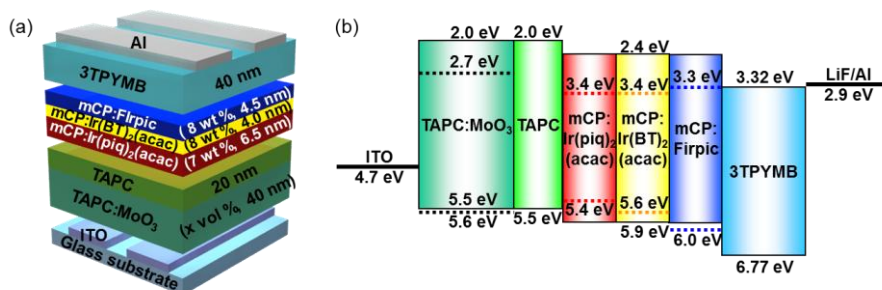


**Figure 4.3** (a) Device structure and (b) schematic energy level diagram of the phosphorescent white OLEDs.

Figure 4.4 (a) and (b) show the J-V and L-V characteristics of the devices prepared with different MoO<sub>3</sub> doping concentrations, respectively. It is clear that the current density and luminance of the device increase significantly with the insertion of the MoO<sub>3</sub> doped TAPC layer compared with the device with an undoped layer. For the device with 25% doping concentration, the driving voltage at 1000 cd/m<sup>2</sup>,  $V_{1000\text{nit}}$ , is 5.6 V, and the current density at 10 V,  $J_{10\text{V}}$ , is around 230 mA/cm<sup>2</sup>, whereas  $V_{1000\text{nit}}$  is 6.8 V and  $J_{10\text{V}}$  is around 73 mA/cm<sup>2</sup> for the device with an undoped layer. This result indicates that the layer of MoO<sub>3</sub> doped TAPC can inject and transport holes very efficiently due to improved hole injection between ITO and the MoO<sub>3</sub> doped TAPC layer and enhanced electrical conductivity. However, the increase in the luminance of all devices decreases in the high-current-density region as shown in the inset of Figure 4.4(b). The slope of L-J curve decreases when the current density of the device is greater than approximately 20 mA/cm<sup>2</sup>. As the current density of the device increases, many holes accumulate at the interface between the EML and the ETL because of the deep HOMO energy level of 3TPYMB and

the relatively higher hole mobility of mCP with respect to the electron mobility [89]; the accumulated holes then disturb the radiative emission of triplet excitations. In other words, triplet-triplet (T-T) annihilation or triplet-polaron quenching may cause the decrease of the luminance in the high-current-density region [90].

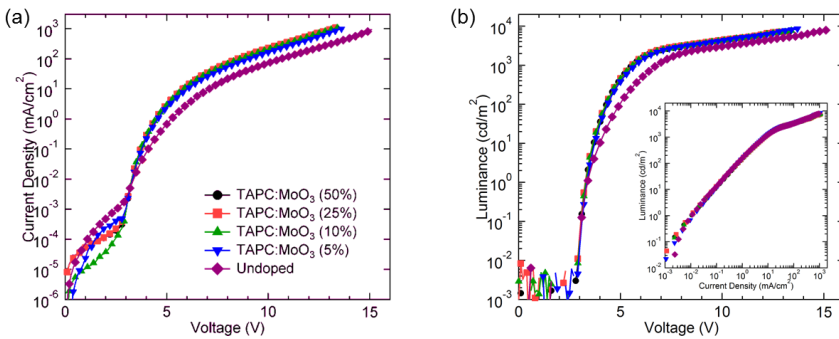


**Figure 4.4** (a) J-V and (b) L-V characteristics of the phosphorescent white OLEDs with different MoO<sub>3</sub> doping concentrations. Inset in (b): L-J characteristics from the same devices.

Figure 4.5(a) and (b) show the LPE-L characteristics and the LPE and EQE of the devices at 1000 cd/m<sup>2</sup> with different MoO<sub>3</sub> doping concentrations, respectively. The LPE of the device with a MoO<sub>3</sub> doped TAPC layer is much higher than that of the device with an undoped layer. The LPE of the device with undoped, 5%, 10%, 25%, and 50% MoO<sub>3</sub> doped layer is 9.8 lm/W, 11.2 lm/W, 11.4 lm/W, 11.0 lm/W, and 10.7 lm/W at 100 cd/m<sup>2</sup>, respectively. The LPE of undoped device is comparable to the reported values for the white OLEDs with similar emitting colors which are blue, orange, and red [87]. The

LPE of the device with a 5% doping concentration is around 7.9 lm/W at 1000  $\text{cd/m}^2$ , which is 27.4% higher than that of the undoped device, which is around 6.2 lm/W. The LPE of the device with a  $\text{MoO}_3$  doped TAPC layer increases up to a doping concentration of 5% and then decreases at 1000  $\text{cd/m}^2$  as shown in Figure 4.5(b). This pattern is related to the EQE variation tendency with the doping concentration. The hole mobility of TAPC [91] is much higher than the electron mobility of 3TPYMB [65]. The electrical conductivity of TAPC increases with the  $\text{MoO}_3$  doping concentration. Therefore, the hole density is much higher than the electron density in the EML as the doping concentration increases, a pattern that leads to an electron-hole imbalance, and, thus, the EQE decreases as the doping concentration increases. This electron-hole imbalance can be improved by employing an electron transport material with high electron mobility or *n*-type doped organic layer. We summarize the performance of the phosphorescent white OLEDs with different  $\text{MoO}_3$  doping concentrations in Table 4.1.

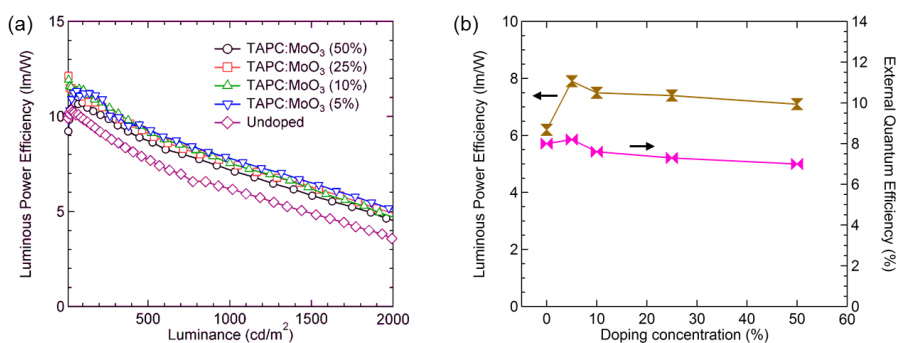


**Figure 4.5** (a) LPE-L characteristics and (b) LPE and EQE of the white OLEDs at 1000  $\text{cd/m}^2$  with different  $\text{MoO}_3$  doping concentrations.

**Table 4.1** Performance of the phosphorescent white OLEDs with different MoO<sub>3</sub> doping concentrations..

Doping concentration	Current density <sup>a</sup> (mA/cm <sup>2</sup> )	Driving voltage <sup>b</sup> (V)	Max. EQE (%)	LPE <sup>b</sup> (lm/W)	CIE 1931 chromatic coordinates <sup>c</sup> (x, y)	CRI <sup>c</sup>
50%	222	5.6	8.1	7.1	(0.4134, 0.3869)	85
25%	230	5.6	8.4	7.4	(0.4303, 0.3893)	86
10%	210	5.6	8.9	7.5	(0.4339, 0.3837)	84
5%	165	5.7	9.3	7.9	(0.4325, 0.3837)	84
undoped	73	6.8	9.5	6.2	(0.4596, 0.3826)	84

<sup>a</sup>At 10 V.

<sup>b</sup>At luminance of 1000 cd/m<sup>2</sup>.

<sup>c</sup>At current density of 153 mA/cm<sup>2</sup>.

Figure 4.6(a)–(e) show the EL spectra, normalized by the main emission peak of FIrpic at 468 nm, for the white OLEDs with different MoO<sub>3</sub> doping concentrations at various current densities. The orange (~560 nm) and the red (~620 nm) emission peaks of the EL spectrum increase irrespective of the MoO<sub>3</sub> doping concentrations as the current density increases, so the CIE 1931 chromatic coordinates move to red region. The hole can be easily trapped in the red and orange EML due to the low HOMO level of Ir(piq)<sub>2</sub>(acac) and Ir(BT)<sub>2</sub>(acac) compared with that of mCP. As the current density increases,

the amounts of trapped hole increase in the red and orange emitting layer, resulting in the color shift as shown in each inset of Figures 4.6(a)–(e). The change of EL spectrum is severe in the device with undoped TAPC. This implies that the hole in the undoped TAPC is more electric field dependent than the hole in the *p*-doped TAPC. We also compare the EL spectra with different MoO<sub>3</sub> doping concentrations at the same current density of  $J=153$  mA/cm<sup>2</sup> as shown in Figure 4.6(f). As the MoO<sub>3</sub> doping concentration increases, the intensity of the red emission peak is reduced and shifted from 623 nm (50%) to 619 nm (undoped).

Figure 4.7(a) shows the emission ratio of red, orange, and blue of the white OLEDs with different MoO<sub>3</sub> doping concentrations as a function of current density. The red emission ratio increases as the current density increases, whereas the orange and blue emission ratio decreases as the current density increases. This result is because the main exciton recombination region changes from the ETL side to the HTL side. In other words, the electrons move to HTL side and form excitons by recombination with trapped holes in the red dopant, resulting in the increase of red emission. However, the blue and orange emissions increase as the MoO<sub>3</sub> doping concentrations increase. This result implies that the recombination region is gradually shifted to the cathode side as the MoO<sub>3</sub> doping concentration increases. In other words, more holes reach the ETL side by inserting a MoO<sub>3</sub> doped TAPC layer. In addition, the increase in absorption near 703 nm as the doping concentration increases as shown in Figure 4.1 slightly affects the decrease in the red emission of the white OLEDs.

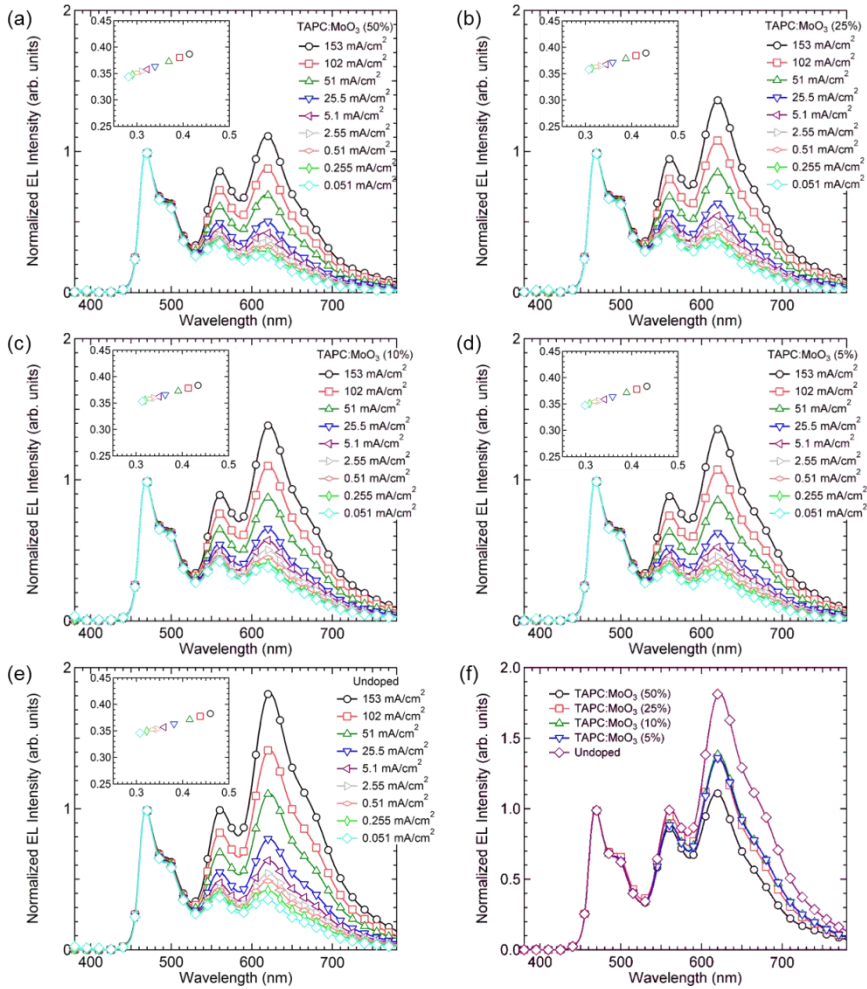


**Figure 4.6** (a)–(e) Normalized EL spectra of the white OLEDs with different current density at fixed doping concentrations and (f) normalized EL spectra of the white OLEDs with different MoO<sub>3</sub> doping concentrations at the same current density ( $J=153$  mA/cm<sup>2</sup>). Each inset shows the corresponding CIE color coordinates.

The CRI increases as the current density increases regardless of MoO<sub>3</sub> doping concentrations as shown in Figure 4.7(b). All devices show high CRI which are over 84 at  $J=153$  mA/cm<sup>2</sup> due to obvious three emissive zones and

a broad resulting spectrum. On the other hand, the CCT decreases as the current density increases because of red and orange emission increase. The ranges of CCT and CIE 1931 chromatic coordinate of the devices are from 2400 K to 3400 K and from (0.4596, 0.3826) to (0.4134, 0.3869), respectively, at  $153 \text{ mA/cm}^2$  when the  $\text{MoO}_3$  doping concentrations change from 0% to 50%. These values are comparable to the values of incandescent bulb which are 2854 K and (0.448, 0.408), respectively [92]. The higher current density than  $153 \text{ mA/cm}^2$  may cause nearly red color instead of white color.

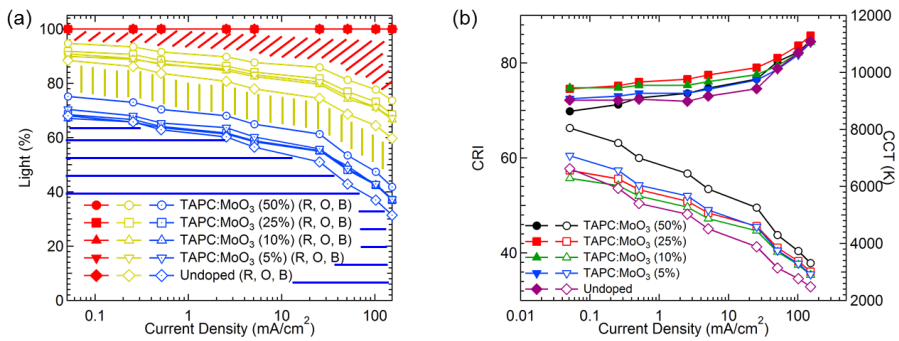


**Figure 4.7** (a) Emission ratio of red, orange, blue colors and (b) CRI and CCT of the white OLEDs with different  $\text{MoO}_3$  doping concentrations as a function of current density.

We also simulated for optimum ratio of each color for maximum CRI using typical EL spectrum of each color as shown in Figure 4.8(a) and simulation program [93]. Figure 4.8(b) shows a captured image of simulation result. The optimum ratio of blue, orange, and red is 1:1:0.8, resulting in high CRI of 85. We compared the simulated optimum EL spectrum with the

measured EL spectrum ( $J=153 \text{ mA/cm}^2$ ) of the device with 25% doping concentration which has the CRI of 86. Two EL spectra are very similar as shown in Figure 4.8(c). Moreover, simulated and measured CIE color coordinates are also similar, which are (0.4443, 0.3928) and (0.4303, 0.3893), respectively. The CCT of measure EL spectrum is slightly higher than that of the simulated EL spectrum which is 2787 K. The CIE color coordinates and CCTs of simulated and measured EL spectra are similar to those of CIE standard illuminant A [92]. These results indicate that the fabricated white OLEDs can be utilized as a good solid state lighting source.

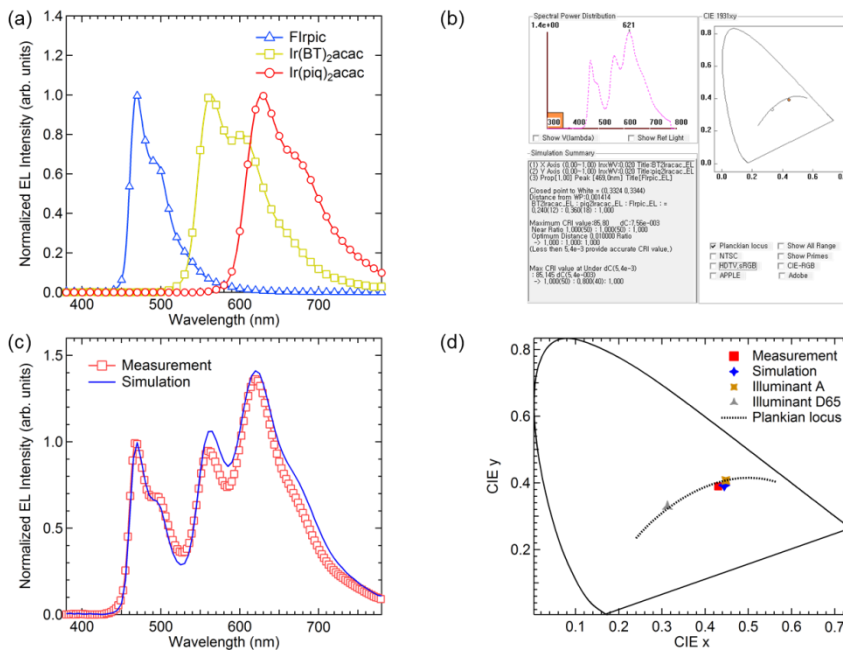


**Figure 4.8** Typical EL spectra of FIrpc, Ir(BT)<sub>2</sub>(acac), Ir(piq)<sub>2</sub>(acac), (b) captured image of the spectra simulation results, (c) EL spectra and (d) CIE color coordinates of simulated and measured white OLEDs (25% doping) and major lighting sources.

## 4.2 Inverted Bottom-Emission White OLEDs Using HTLs with Different Hole Conductivities

### 4.2.1 Control of hole conductivity by using doped HTLs

The EQE ( $\eta_{\text{ext}}$ ) of OLEDs is expressed following equation.

$$\eta_{\text{ext}} = \gamma \eta_1 \eta_2 \eta_3 \quad (4.1)$$

The  $\gamma$  is the number of excitons from the number of injected electrons and holes, the  $\eta_1$  is the number of singlet or triplet excitations from the number of created excitations, the  $\eta_2$  is the number of photons from the number of singlet or triplet excitons, and  $\eta_3$  is the number of photons emitting to air from the number of created photons inside the device. The  $\gamma$  is concerned with the electron-hole balance. In other words, OLEDs have maximum efficiency when the number of injected electrons and holes to EML are same. If the number of injected electrons or holes is larger than opposite charge carrier, the efficiency of the device decreases.

We found that the MoO<sub>3</sub> doped TAPC layer can increase the amounts of holes in OLEDs. The hole conductivity of HTL is concerned with the driving voltage and efficiency of the device. The BCP doping decreases the hole conductivity of  $\alpha$ -NPD layer [94]. To compare the hole conductivity of doped HTL, we fabricated hole-only devices with a structure of ITO/MoO<sub>3</sub> (5 nm)/HTL (100 nm)/MoO<sub>3</sub> (5 nm)/Al (100nm) as shown in the inset of Figure 4.9(a). The HTLs are TAPC doped with MoO<sub>3</sub> (10 vol%), undoped TAPC, and

TAPC doped with BCP (10 vol%). Figure 4.9(a) shows the J-V characteristics of the devices with different HTLs. The device with MoO<sub>3</sub> doped TAPC layer has much higher current density than the device with undoped TAPC, whereas the device with BCP doped TAPC layer has much lower current density than the device with undoped layer. In other words, we can increase or decrease hole current of TAPC layer by doping MoO<sub>3</sub> or BCP. We also compared the absorption spectra of MoO<sub>3</sub> doped and undoped TAPC films with a BCP doped TAPC film as shown in Figure 4.9(b). The BCP doped TAPC film has no absorption in visible spectral region like an absorption spectrum of an undoped TAPC film. The BCP doped TAPC film can be utilized as an HTL in the OLEDs for reducing hole current without emitting light loss.

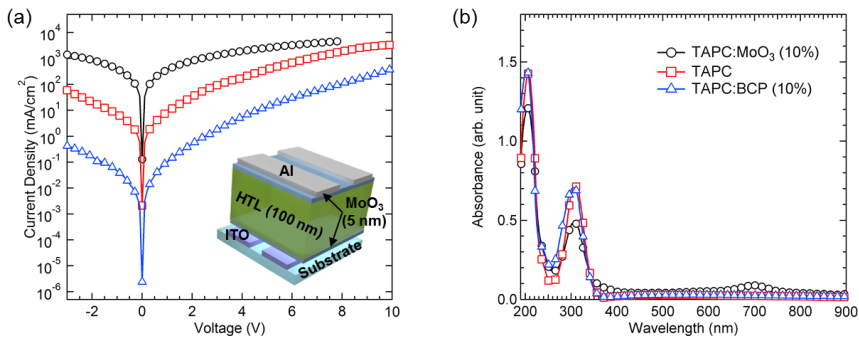


**Figure 4.9** (a) J-V characteristics of hole-only devices with different HTLs and (b) optical absorption spectra of MoO<sub>3</sub> doped, undoped, and BCP doped TAPC films. Inset in (a): structure of the hole-only device.

#### **4.2.2 Inverted bottom-emission white phosphorescent OLEDs using HTLs with different hole conductivities**

We found that ZnO NPs layer can improve electron injection from the ITO to the ETL. However, the driving voltage of the bottom-emission OLEDs is still higher than that of the conventional structure OLEDs. The MoO<sub>3</sub> doped TAPC layer can reduce the driving voltage of OLEDs due to improved hole injection and conductivity. However, only increase of hole current can cause electron-hole imbalance, resulting in low quantum efficiency.

In this part, we fabricated inverted bottom-emission white phosphorescent OLEDs using different HTLs which are MoO<sub>3</sub> doped, undoped, and BCP doped TAPC layer. Figure 4.10(a) and (b) show the device structure and schematic energy level diagram of the inverted bottom-emission white phosphorescent OLEDs, respectively. The device structure is ITO/ZnO NPs/3TPYMB (40 nm)/mCP:FIrpic (8 wt%, 4nm)/mCP:Ir(ppy)<sub>3</sub> (8 wt%, 3.5 nm)/Ir(piq)<sub>2</sub>(acac) (7 wt%, 7.5 nm)/TAPC (15 nm)/HTLs (35 nm)/MoO<sub>3</sub> (10 nm)/Al (100 nm). We can find the shift of main exciton recombination region in this device because the device has three emitting layers with different colors of red, green, and blue.

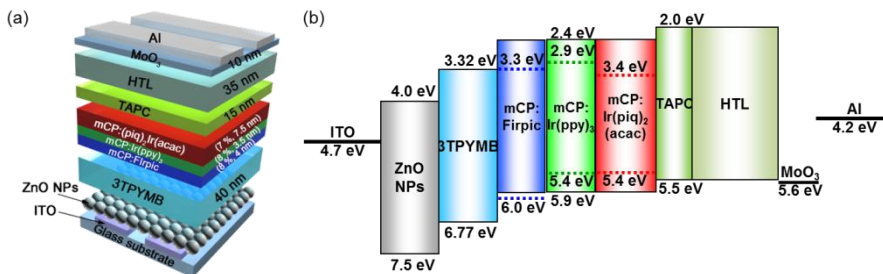


**Figure 4.10** (a) Device structure and (b) schematic energy level diagram of the inverted bottom-emission white phosphorescent OLEDs with different HTLs.

Figure 4.11(a) and (b) show the J-V characteristics and L-V characteristics of the inverted bottom-emission white phosphorescent OLEDs with different HTLs, respectively. The device with MoO<sub>3</sub> doped TAPC layer shows higher current density and luminance than the device with undoped TAPC and BCP doped TAPC layer at the same voltage. This result is same with the trend of hole-only devices and the control of hole conductivity is working well in the inverted OLEDs. The current density of the device with MoO<sub>3</sub> doped TAPC layer at 15 V is 192 mA/cm<sup>2</sup>, whereas those of the devices with undoped and BCP doped TAPC layer are 52 mA/cm<sup>2</sup> and 19 mA/cm<sup>2</sup>, respectively. The driving voltage of the device with MoO<sub>3</sub> doped TAPC layer for 1000 cd/m<sup>2</sup> is 11.4 V which is 1.3 V lower than that of the device with undoped TAPC layer. The device with BCP doped TAPC layer need 13.6 V for 1000 cd/m<sup>2</sup>. Consequently, the current density and driving voltage of the device is affected by the conductivity of HTLs.

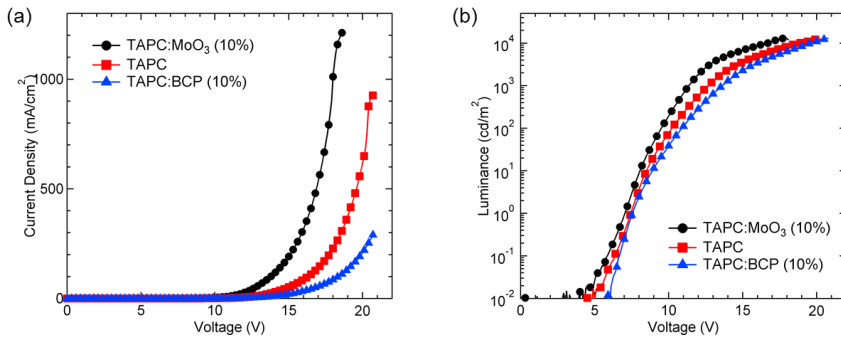


**Figure 4.11** (a) J-V and (b) L-V characteristics of the inverted bottom-emission white phosphorescent OLEDs with different HTLs.

Figure 4.12(a) shows the EQE-J characteristics of the devices with different HTLs. The tendency of the EQE-J characteristics is different from the J-V and L-V characteristics. The EQE of the device decreases as the conductivity of HTL increases. For example, the maximum EQE of the device with BCP doped TAPC layer is 8.6%, whereas those of the devices with undoped and MoO<sub>3</sub> doped TAPC layer are 6.4% and 4.1%, respectively. This value is the highest EQE without other optical light extraction techniques or *n*-type doping method in reported value of inverted white OLEDs [95–97]. The improved efficiency of the device with BCP doped TAPC layer is due to enhanced electron-hole balance. On the other hand, the device with MoO<sub>3</sub> doped TAPC layer has very low efficiency at low current density region. It indicates that the amounts of injected hole carrier is much larger than those of injected electron carrier at low voltage region. In other words, amounts of injected electrons are still lower than that of the injected holes though ZnO

NPs layer is utilized. Therefore, the device with MoO<sub>3</sub> doped TAPC layer has low EQE.

Figure 4.12(b) shows the driving voltages and LCEs at 1000 cd/m<sup>2</sup> as a function of different HTLs. The device with MoO<sub>3</sub> doped TAPC layer has low driving voltage and efficiency, whereas the device with BCP doped TAPC layer has high driving voltage and efficiency. Ultimately, improvement of electron injection is still required for high performance inverted OLEDs.

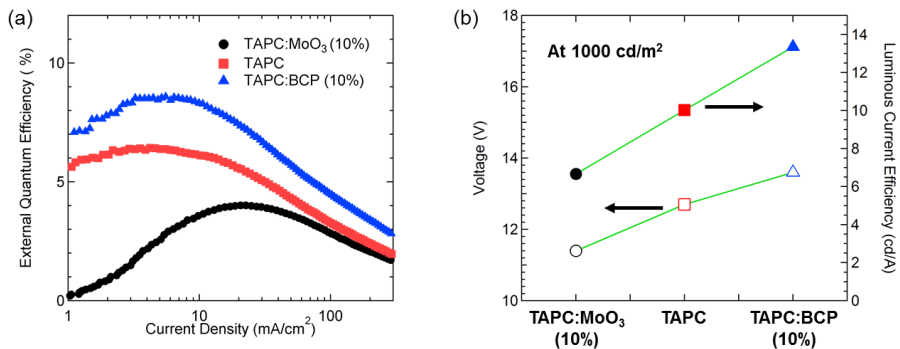


**Figure 4.12** (a) EQE-J characteristics and (b) driving voltages and LCEs at 1000 cd/m<sup>2</sup> of the inverted bottom-emission white phosphorescent OLEDs with different HTLs.

Figure 4.13(a)–(c) show the EL spectra, normalized by the main emission peak of FIrpic at ~471 nm, for the white OLEDs with different HTLs at various current densities. The red (~627 nm) emission peaks of the EL spectrum increase irrespective of HTLs but the increase of green (~504 nm) emission peak is very low as the current density increases, so the CIE 1931 chromatic coordinates move to red region. For example, the device with BCP

doped TAPC layer has a CIE color coordinate of (0.36, 0.43) at 0.51 mA/cm<sup>2</sup> but (0.43, 0.41) at 51 mA/cm<sup>2</sup>. The hole can be easily trapped in the red emitting layer due to the low HOMO level of Ir(piq)<sub>2</sub>(acac) than mCP and thick red emitting layer compared with green or blue layer. As the current density increases, the amounts of trapped hole increase in the red emitting layer, resulting in the color shift to red. We also compare the emission ratios of red, green, and blue of the devices with different HTLs as a function of current density as shown in Figure 4.13(d). The red emission ratio increases as the current density increases, whereas the green and blue emission ratio decreases as the current density increases. This result is because the main exciton recombination region changes from the ETL side to the HTL side. In other words, the electrons move to the HTL side and form excitons by recombination with trapped holes in the red dopant, resulting in increase of red emission.

The device with MoO<sub>3</sub> doped TAPC layer has large blue and green emission ratio than the device with undoped and BCP doped TAPC layer. The CIE color coordinates of the devices with MoO<sub>3</sub> doped, undoped, and BCP doped TAPC layer are (0.34, 0.32), (0.36, 0.43), and (0.38, 0.42), respectively, and their CCT are 5229 K, 4696 K, and 4220 K, respectively, at 5.1 mA/cm<sup>2</sup>. This means that the green and blue emissions increase as the conductivity of HTL increases. This result is due to the main exciton recombination region gradually moves to the cathode side as the MoO<sub>3</sub> doping concentration increases. In other words, more holes reach the ETL side by inserting a *p*-type doped TAPC layer.

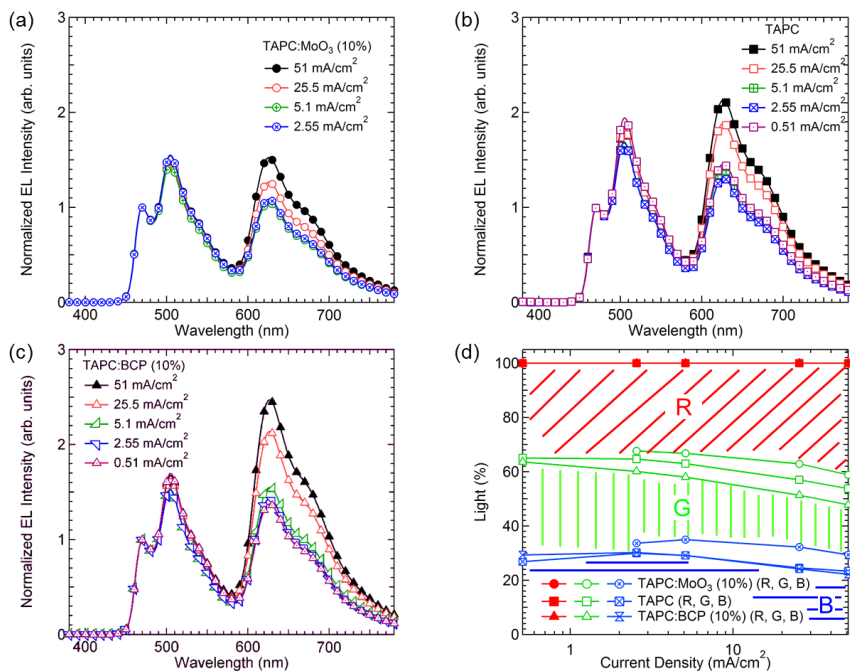


**Figure 4.13** EL spectra of the inverted bottom-emission white phosphorescent OLEDs with (a) MoO<sub>3</sub> doped TAPC, (b) undoped TAPC, and (c) BCP doped TAPC as HTLs with different current densities, (d) emission ratios of red, green, and blue of each device as a function of current density.

## Chapter 5 OLEDs with a Common Red Layer

The electron-hole balance is one of critical factors for determining the efficiency of OLEDs. In chapter 4, we found that the efficiency of OLEDs can be controlled by changing the conductivity of HTLs. To investigate the relationship between performances of OLEDs and hole current, we utilize various hole transport materials with different HOMO energy levels. These different HOMO energy levels can affect the injection of holes from anode to HTL. Furthermore, we also insert red phosphorescent dye doped HTLs to control the hole conductivity. We think that the HOMO energy level differences between the hole transport materials and the red dye have an influence on the transport of holes in HTLs.

Because the red phosphorescent dye has more advantages than other dopants, we select the red phosphorescent dye as a hole conductivity control dopant. For instance, the red phosphorescent dye generally has low HOMO energy level compared with other materials so hole traps can easily be formed in the HTLs. This means that we can simply control the hole current by changing the depth of hole trap. In addition, we can reduce one fine metal mask process when this red dye doped HTL is used in the green and blue OLEDs. Typically, a conventional full-color OLED panel consists of R, G, and B sub-pixels. Thus, three fine metal shadow masks are required for forming the R, G, and B sub-pixels, while the other functional layers can be deposited through one common mask. Since the size of the sub-pixels and the

interval between them are in the length of the micrometer scale, aligning each sub-pixel separately with the FMM is a sophisticated and time-consuming process, which increases fabrication cost. If one of the R, G, and B sub-pixels can be made by using the common mask instead of the independent FMM, the manufacturing cost will be decreased. A few years ago, Sony and Samsung demonstrated its practicability for the OLED fabrication by using a common blue layer adjacent to the ETL, maintaining the overall performances of red and green pixels [98, 99]. This common layer not only performs as the HBL, but also has advantages in microcavity effect. Chen *et al.* also reported a common blue layer on the HTL to eliminate the blue FMM, without any change in driving voltages and emission spectra of the other colors [100]. However, the efficiency of blue-emitting pixels in the papers reported so far was quite low because the common layer should be thin to suppress its emission in other color-emitting pixels. Besides, they also used blue fluorescent materials which can have 25% in terms of the IQE at the maximum, instead of phosphorescent materials of which the IQE can be 100% [9, 101]. In addition, the common blue EML generally requires a wide energy band gap material as the host, which causes inefficient hole or electron injection from adjacent layers. In particular, ultra-wide band gap host materials such as diphenyldi(*o*-tolyl)silane (UGH1) and *p*-bis(triphenylsilyl)benzene (UGH2) are required for deep-blue phosphorescence emission and their HOMO and LUMO energy levels are very low and high, respectively, resulting in very low charge carrier injection and transport properties [102]. To enhance the injection efficiency, in this case,

additional interlayer can be inserted but it leads to more complex device structure and increase of fabrication cost.

In order to improve electron-hole balance and simplify the process, in this chapter, we introduce a novel device structure using a common red layer (CRL) in the HTL side for the full-color OLEDs with high efficiency based on phosphorescent red, green, and also blue dyes.

## 5.1 Full-Color OLEDs with CRLs

Figure 5.1(a) shows the device structure of the conventional OLEDs having R, G, and B sub-pixels patterned by three FMM steps, whereas Figure 5.1(b) depicts the CRL-employed OLEDs having G and B sub-pixels using two FMM steps by skipping the FMM step for a red sub-pixel.

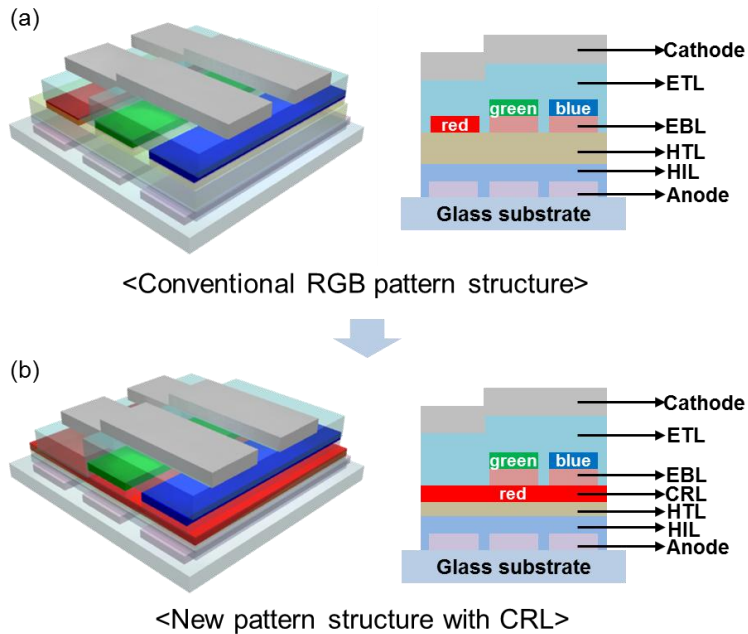


**Figure 5.1** Schematic device structures of (a) the conventional full-color OLEDs and (b) the full-color OLEDs with CRL.

For both devices, we used ITO as an anode and  $\text{MoO}_3$  as an HIL. Five organic materials possessing different HOMO energy levels, i.e., Spiro-2CBP,  $\alpha$ -NPD, TAPC, BBTC, and CBP, were used in the HTL and the host of CRL

at the same time since they have good hole mobility [91, 103–105]. The CRL consists of each host material doped with Ir(piq)<sub>2</sub>(acac) (8 wt%) with the thickness of 15 nm. For efficient green- and blue- EMLs, we used mCP as a host which has high triplet energy level of 2.9 eV doped with Ir(ppy)<sub>2</sub>(acac) and Flrpic as the green and blue phosphorescent dopants, respectively [106]. For the green and blue sub-pixels, 10 nm of TAPC layer was used next to the CRL as a triplet-exciton and electron blocking layer (EBL) since it possesses high triplet energy level as well as the low LUMO energy level. As an ETL, TmPyPB was selected owing to its high electron mobility of  $1 \times 10^{-3} \text{ cm}^2/\text{V} \cdot \text{s}$  and higher triplet energy level (2.78 eV) compared to Flrpic (2.65 eV) so that it can efficiently transport electrons and prevent excitons from being transferred to ETL [106, 107]. LiF and Al were used as an EIL and a cathode, respectively. To investigate the effect of the CRL in the OLEDs, R, G, and B devices were fabricated with following structures:

R1: ITO/MoO<sub>3</sub> (10 nm)/HTL (35 nm)/**CRL**/TmPyPB (40 nm)/  
LiF (0.5 nm)/Al (100 nm)

G1: ITO/MoO<sub>3</sub> (10 nm)/HTL (35 nm)/**CRL**/EBL (10 nm)/  
mCP:Ir(ppy)<sub>2</sub>(acac) (8 wt%, 15 nm)/TmPyPB (40 nm)/LiF (0.5 nm)/  
Al (100 nm)

G2: ITO/MoO<sub>3</sub> (10 nm)/HTL (50 nm)/EBL (10 nm)/  
mCP:Ir(ppy)<sub>2</sub>(acac) (8 wt%, 15 nm)/TmPyPB (40 nm)/LiF (0.5 nm)/  
Al (100 nm)

B1: ITO/MoO<sub>3</sub> (10 nm)/HTL (35 nm)/**CRL**/EBL (10 nm)/

mCP:FIrpic (8 wt%, 15 nm)/TmPyPB (40 nm)/LiF (0.5 nm)/Al (100 nm)

B2: ITO/MoO<sub>3</sub> (10 nm)/HTL (50 nm)/EBL (10 nm)/

mCP:FIrpic (8 wt%, 15 nm)/TmPyPB (40 nm)/LiF (0.5 nm)/Al (100 nm)

B3: ITO/MoO<sub>3</sub> (10 nm)/ HTL (35 nm)/**CRL**/

mCP:FIrpic (8 wt%, 15 nm)/TmPyPB (40 nm)/LiF (0.5 nm)/Al (100 nm)

where **CRL** means the layer of HTL:Ir(piq)<sub>2</sub>(acac) (8 wt%, 15 nm) and HTLs are Spiro-2CBP,  $\alpha$ -NPD, TAPC, BBTC, and CBP. The thickness of HTL in the device with CRL (i.e., G1 and B1) was reduced to 35 nm by adding the CRL (15 nm) to keep identical with the thickness of HTL without CRL (i.e., G2 and B2). The schematic energy level diagram for all materials is shown in Figure 5.2. Device R1 represents a red sub-pixel for OLEDs with using CRL, and devices G1 and G2 stand for green sub-pixel with and without CRL, respectively. Similarly, devices B1 and B2 denote blue sub-pixel with and without CRL, while device B3 is a control device without the TAPC layer (i.e., EBL) as compared to device B1 to show the function of the EBL in this CRL structure.

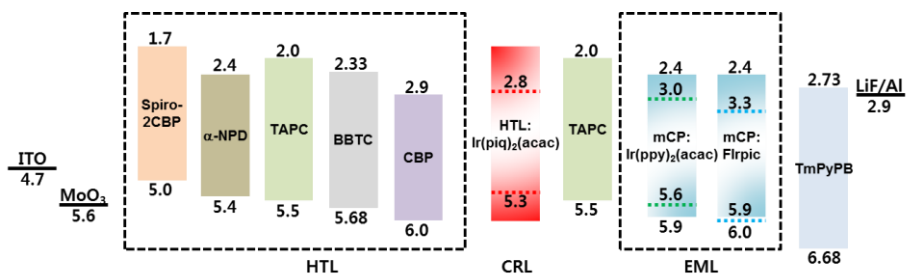


**Figure 5.2** Energy level diagram for the R, G, and B OLED devices.

### 5.1.1 Red phosphorescent OLEDs with different hosts and HTLs

As the CRL, we tested five different host materials, which are Spiro-2CBP, α-NPD, TAPC, BBTC, and CBP, doped with a typical red dopant, Ir(piq)<sub>2</sub>(acac). We also utilized these red host materials as the HTL in each device for the simple device structure.

Figure 5.3 shows the J-V and L-V characteristics of the red devices with different hosts and HTLs. The current densities of devices R1 with Spiro-2CBP, α-NPD, TAPC, and BBTC are higher than that of device R1 with CBP at the same voltage. For instance, the current densities of devices R1 with Spiro-2CBP, α-NPD, TAPC, BBTC, and CBP at 10 V are 549 mA/cm<sup>2</sup>, 407 mA/cm<sup>2</sup>, 470 mA/cm<sup>2</sup>, 492 mA/cm<sup>2</sup>, and 189 mA/cm<sup>2</sup>, respectively. The turn-on voltages of devices R1 with Spiro-2CBP, α-NPD, TAPC, BBTC, and CBP are 3.3 V, 3.2 V, 3.2 V, 3.5 V, and 3.7 V respectively, which roughly correspond to the descending order of HOMO energy levels of HTLs. The driving voltage of device R1 with Spiro-2CBP at 1000 cd/m<sup>2</sup> is 6.3 V which is the lowest value among those of other devices due to low HOMO energy level

of Spiro-2CBP. However, the driving voltage of device R1 with BBTC at  $1000 \text{ cd/m}^2$  is 6.5 V which is lower than that of devices R1 with  $\alpha$ -NPD (6.7 V), TAPC (6.8 V) and CBP (7.6 V) because BBTC is efficient host for red phosphorescence and has lower HOMO energy level than CBP. The device with TAPC shows higher luminance at low driving voltage but low luminance at high driving voltage because high hole mobility and very low electron mobility of TAPC cause accumulation of holes near the EML/ETL interface, resulting in triplet-polaron or triplet-triplet annihilation at high voltage region and resultant rapid decreases of luminance [90].

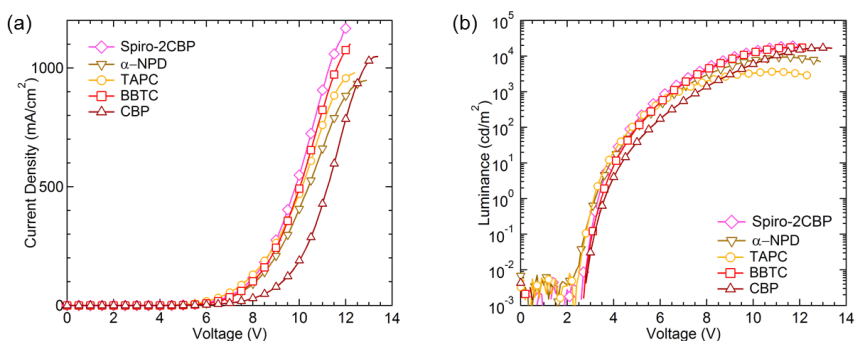


**Figure 5.3** (a) J-V and (b) L-V characteristics of the devices R1 with different hosts and HTLs.

Figure 5.4(a), (b), and (c) show EQE, LPE, and LCE versus current density characteristics of the device R1 with different hosts and HTLs. The devices R1 with Spiro-2CBP and BBTC have higher efficiencies than the devices R1 with CBP,  $\alpha$ -NPD, and TAPC. The EQEs of the devices R1 with Spiro-2CBP,  $\alpha$ -NPD, TAPC, BBTC, and CBP are 8.3%, 6.1%, 3.1%, 8.4%,

and 7.5% at 1000  $\text{cd/m}^2$ , respectively, which is not as high as the conventional red phosphorescent OLEDs since device R1 has thin HTL and no EBL. Nevertheless, devices R1 with Spiro-2CBP and BBTC exhibits the highest EQE over 10% because Spiro-2CBP and BBTC are good red phosphorescent host materials as reported in the previous papers [103, 104]. Figure 5.4(d) shows the LPE and LCE of the devices R1 at 1000  $\text{cd/m}^2$  as a function of HTLs. The device R1 with TAPC shows especially low efficiency and rapid roll-off compared with other devices. This may be due to high hole mobility and hole-dominant transport property of TAPC.

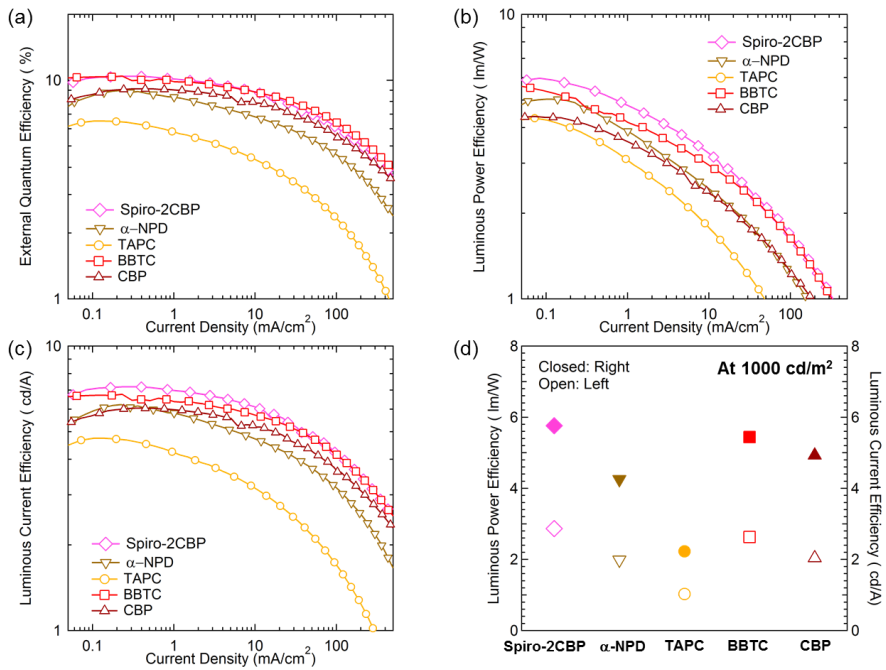


**Figure 5.4** (a) EQE, (b) LPE, (c) LCE vs J characteristics and (d) LPE and LCE at 1000  $\text{cd/m}^2$  of devices R1 with different hosts and HTLs.

Figure 5.5(a)–(e) show the normalized EL spectra of devices R1 with Spiro-2CBP,  $\alpha$ -NPD, TAPC, BBTC, and CBP, respectively, as HTLs at different driving voltages. All spectra show typical EL spectrum of Ir(piq)<sub>2</sub>(acac) with main emission peak of ~630 nm. Each device has same EL spectra regardless of driving voltage. However, the EL spectrum of device R1 with  $\alpha$ -NPD and TAPC exhibits very small additional spectrum at ~430 nm and ~425 nm, respectively, which may be emission from  $\alpha$ -NPD and TAPC not from Ir(piq)<sub>2</sub>(acac) or emission from the exciplex which is formed by hole in the  $\alpha$ -NPD or TAPC and electron in the TmPyPB due to very low electron mobility of  $\alpha$ -NPD and TAPC. Meanwhile, the CIE color coordinates of the devices R1 with Spiro-2CBP,  $\alpha$ -NPD, TAPC, BBTC, and CBP are (0.68, 0.32), (0.67, 0.31), (0.66, 0.31), (0.68, 0.31), and (0.68, 0.32), respectively, at 7 V.

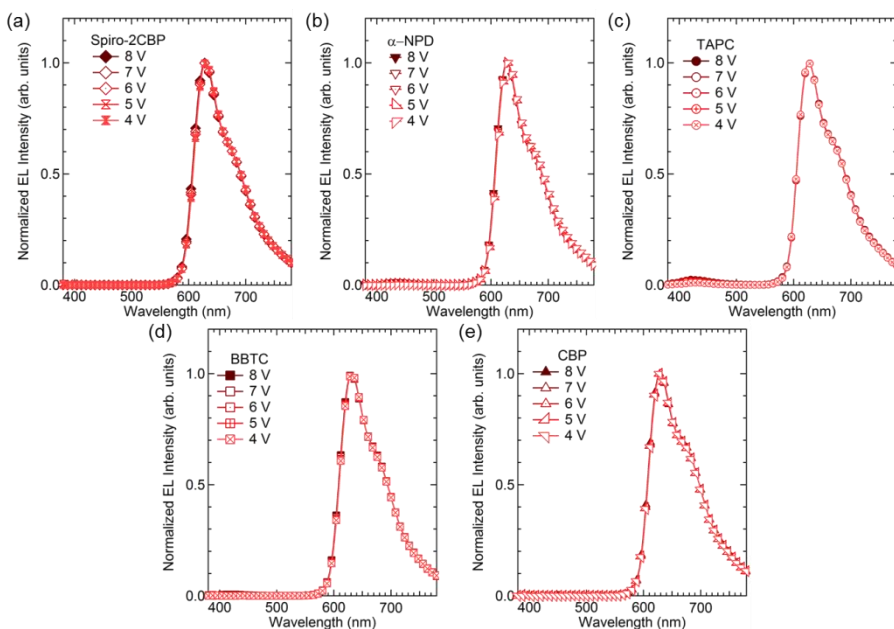


**Figure 5.5** Normalized EL spectra of devices R1 with (a) Spiro-2CBP, (b)  $\alpha$ -NPD, (c) TAPC, (d) BBTC, and (e) CBP as hosts and HTLs at different driving voltages.

### 5.1.2 Green phosphorescent OLEDs with different HTLs

We compared the device G1 (with CRLs) with the device G2 (without CRLs). Figure 5.6 shows the J-V and L-V characteristics of the green devices without and with CRLs with different hosts and HTLs. The current densities at a fixed voltage were decreases when the CRL was inserted, because the CRL doped with red dye has lower hole transporting property. However, the decrement of current density highly depends on the material we used; for instance, the current densities of the device G1- $\alpha$ -NPD and G1-TAPC are almost same with the device G2- $\alpha$ -NPD and G2-TAPC, respectively, which are 68 and 71

$\text{mA/cm}^2$ , 115 and  $112 \text{ mA/cm}^2$  at 10 V, respectively. In case of using BBTC, the current density of the device G1 ( $65 \text{ mA/cm}^2$ ) is quite lower than that of the device G2 ( $111 \text{ mA/cm}^2$ ) at 10 V. A drastic decrease of current density is observed in the devices using Spiro-2CBP and CBP as HTLs. The device G2-Spiro-2CBP and CBP exhibit  $206 \text{ mA/cm}^2$  and  $125 \text{ mA/cm}^2$  at 10 V, whereas the device G1-Spiro-2CBP and G1-CBP show  $74 \text{ mA/cm}^2$  and  $15 \text{ mA/cm}^2$  at the same voltage. These results mean that the hole trap level of CRL is a dominant factor of transport property rather than injection barrier between  $\text{MoO}_3$  and HTLs. The hole trap depth ( $\Delta E_{\text{HOMO}}$ ) can be calculated from the difference of the HOMO energy levels between the host and dopant materials. As shown in Figure 5.7(a), the hole trap depth of Spiro-2CBP,  $\alpha$ -NPD, TAPC, BBTC, and CBP are -0.3 eV, 0.1 eV, 0.2 eV, 0.38 eV, and 0.7 eV, respectively. As the trap level becomes deeper, higher energy is required for the trapped carriers to escape the site [108]. Figure 5.7(b) shows the driving voltage changes of green ( $\Delta V_G$ ) at  $1000 \text{ cd/m}^2$  by inserting the CRLs with different host materials making different hole trap levels. The increase of driving voltage is negligible in the device with  $\alpha$ -NPD ( $\Delta V_G=0.1 \text{ V}$ ), TAPC ( $\Delta V_G=0.0 \text{ V}$ ), and BBTC ( $\Delta V_G=0.3 \text{ V}$ ), but high in the device with Spiro-2CBP ( $\Delta V_G=0.6 \text{ V}$ ) and CBP ( $\Delta V_G=1.6 \text{ V}$ ) due to the deep trap energy levels. The reason for increased driving voltage of the device with Spiro-2CBP may be due to that the red dopant disturbs the transport of hole in Spiro-2CBP like the BCP in TAPC layer in chapter 4.2.

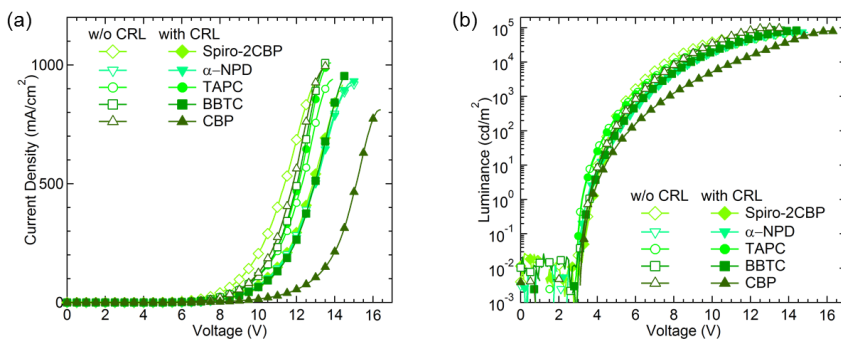


**Figure 5.6** (a) J-V and (b) L-V characteristics of the devices G1 and G2 with different HTLs.

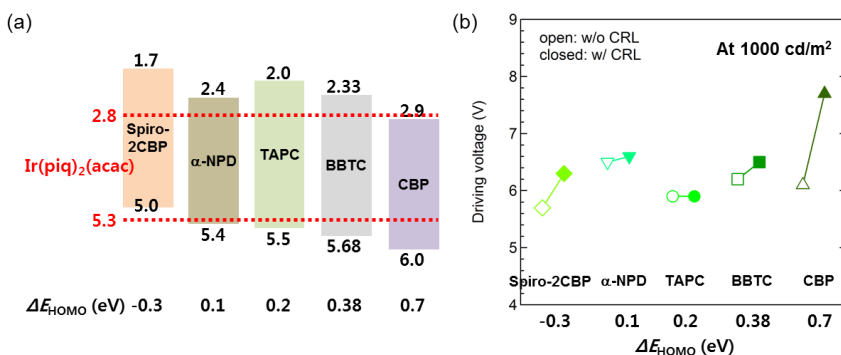


**Figure 5.7** (a) Schematic energy levels of Ir(piq)<sub>2</sub>(acac) doped Spiro-2CBP,  $\alpha$ -NPD, TAPC, BBTC, and CBP with the hole trap depth ( $\Delta E_{\text{HOMO}}$ ) calculated from the difference of the HOMO energy levels between the host and dopant materials. (b) Driving voltage changes at 1000 cd/m<sup>2</sup> with and without CRL as a function of  $\Delta E_{\text{HOMO}}$ .

The effects of the depth of trap site on hole transport properties were confirmed with hole-only devices, of which the structure is ITO/MoO<sub>3</sub> (10 nm)/HTL (100 nm) or HTL:Ir(piq)<sub>2</sub>(acac) (8 wt%, 100 nm)/MoO<sub>3</sub> (10 nm)/Al

(100 nm) with the same HTLs (i.e., Spiro-2CBP,  $\alpha$ -NPD, TAPC, BBTC, and CBP). As expected, the voltage changes by doping and the voltages for a fixed current density are high in the sequence of trap depth as shown in the J-V characteristics of the hole-only devices in Figure 5.8. Interestingly, the current of  $\alpha$ -NPD is slightly increased by doping a red dopant. This may be because the red dopant serves as hole hopping sites and helps hole transport in  $\alpha$ -NPD [109].

We also measured absorption spectra of pristine Spiro-2CBP,  $\alpha$ -NPD, TAPC, BBTC, CBP films (100 nm), and those films doped with Ir(piq)<sub>2</sub>(acac) (8 wt% , 100 nm) as shown in Figure 5.9. The absorption spectra of the undoped films are nearly same those of the doped films in visible spectral region regardless of HTLs. This means that CRL insertion rarely affects the luminance of devices.

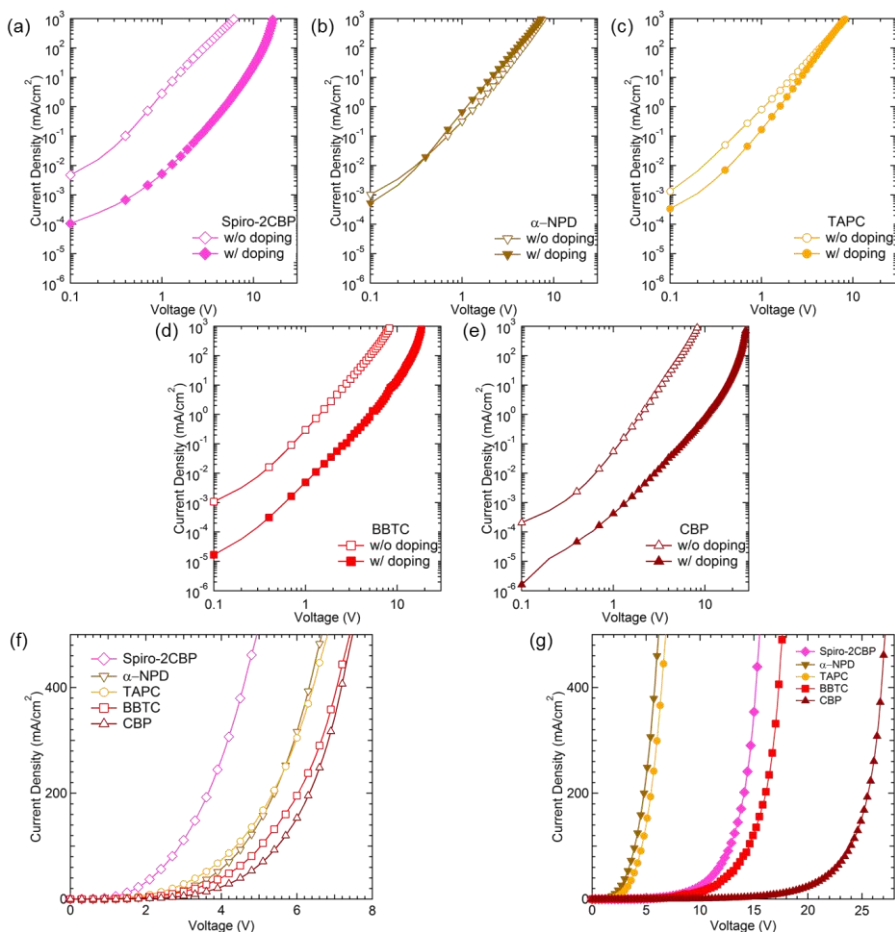


**Figure 5.8** J-V characteristics of the hole-only devices with pristine and Ir(piq)<sub>2</sub>(acac) doped Spiro-2CBP,  $\alpha$ -NPD, TAPC, BBTC, and CBP. (a)–(e) The driving voltage changes by doping at the same current density are high in the sequence of CBP, Spiro-2CBP, BBTC, TAPC, and  $\alpha$ -NPD due to the difference of trap levels. (f)–(g) Comparison of hole transport properties between Spiro-2CBP,  $\alpha$ -NPD, TAPC, BBTC, and CBP, and those of Ir(piq)<sub>2</sub>(acac) doped films.

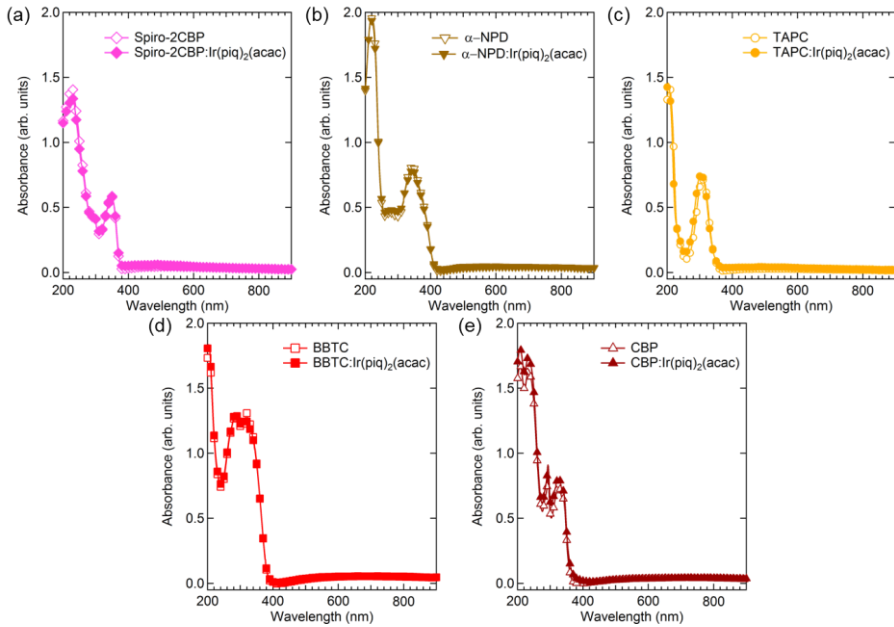


**Figure 5.9** Comparison of the absorption spectra of hole transport materials, (a) Spiro-2CBP, (b)  $\alpha$ -NPD, (c) TAPC, (d) BBTC, and (e) CBP and Ir(piq)<sub>2</sub>(acac) doped hole transport materials. No significant absorption change is observed in visible spectral region.

Figure 5.10(a), (b), and (c) show the EQE, LPE, and LCE versus current density characteristics of the devices G1 and G2 with different HTLs. All devices exhibit high EQEs based on the phosphorescent emitters and the EQEs are similar values regardless of CRLs. The EQEs of devices G1 and G2 with Spiro-2CBP,  $\alpha$ -NPD, TAPC, BBTC, and CBP are (13.0%, 13.2%), (12.8%, 12.6%), (13.0%, 13.1%), (13.2%, 12.6%), and (12.3%, 13.7%), respectively, at 1000 cd/m<sup>2</sup>. The devices with Spiro-2CBP,  $\alpha$ -NPD, and TAPC show nearly same EQEs regardless of CRL insertion. The EQE of the device

with BBTC is slightly increased by insertion CRL. In contrast, the EQE of the device with CBP is decreased by insertion CRL. Figure 5.10(d) show the LPEs and LCEs of devices G1 and G2 with different HTLs at 1000 cd/m<sup>2</sup>. The change of efficiency is small in the devices using Spiro-2CBP,  $\alpha$ -NPD, TAPC, and BBTC, but large in the device using CBP. This is because the insertion of CRL in the device G1 with CBP disturbs the transport of holes, resulting in decrease of efficiency by electron-hole imbalance.

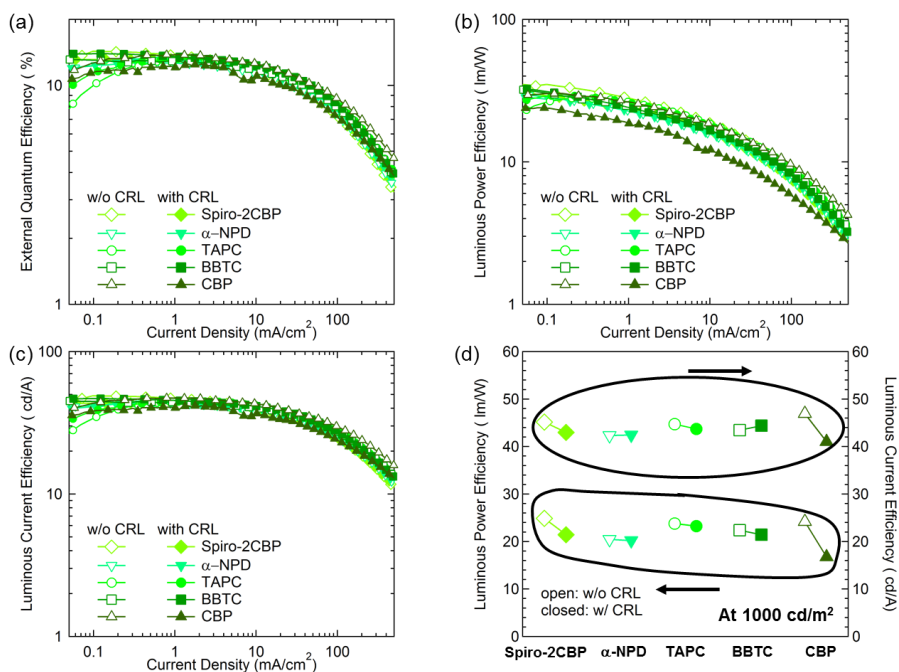


**Figure 5.10** (a) EQE, (b) LPE, (c) LCE vs J characteristics and (d) LPE and LCE at 1000 cd/m<sup>2</sup> of devices G1 and G2 with different HTLs.

Figure 5.11(a)–(e) show the normalized EL spectra of the devices G1 and G2 with Spiro-2CBP,  $\alpha$ -NPD, TAPC, BBTC, and CBP, respectively, as HTLs

at different driving voltages. All spectra show typical EL spectrum of Ir(ppy)<sub>2</sub>(acac) with main emission peak of ~520 nm. Each device has same EL spectra regardless of driving voltage. Furthermore, the insertion of CRL rarely affects the EL spectrum of green phosphorescent OLEDs irrespective of CRLs. The CIE color coordinates change ( $\Delta x$ ,  $\Delta y$ ) between G1 and G2 devices with Spiro-2CBP,  $\alpha$ -NPD, TAPC, BBTC, and CBP are small which are (0.01, 0.01), (0.01, 0.01), (0.01, 0.01), (0.01, 0.01), and (0.02, 0.01), respectively, at 7 V. These results indicate that CRL can be utilized as an HTL without distortion of EL spectra in the green phosphorescent OLEDs.

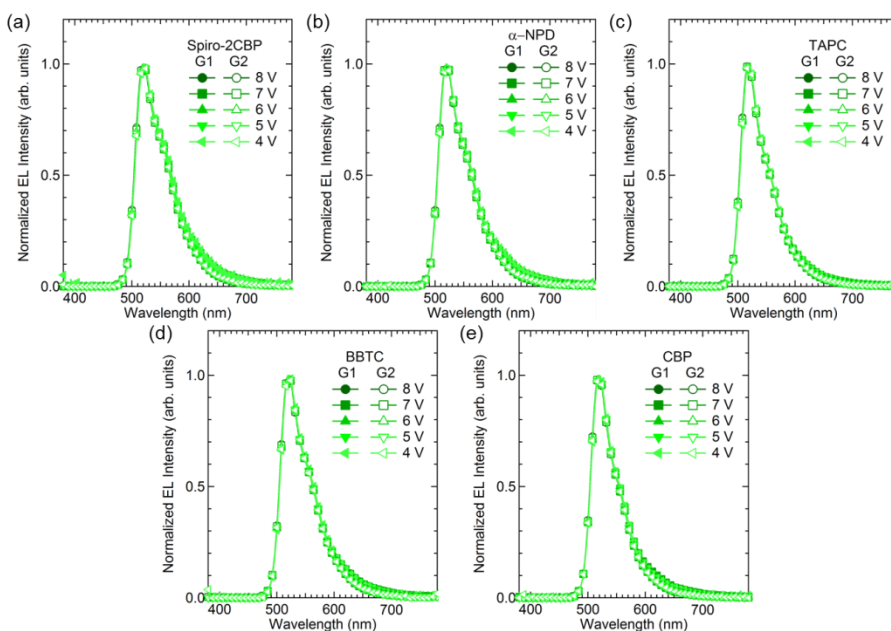


**Figure 5.11** Normalized EL spectra of the devices G1 and G2 with (a) Spiro-2CBP, (b)  $\alpha$ -NPD, (c) TAPC, (d) BBTC, and (e) CBP as HTLs at different driving voltages.

### 5.1.3 Blue phosphorescent OLEDs with different HTLs

We compared the device B1 (with CRLs) with the device B2 (without CRLs). Figure 5.12 shows the J-V and L-V characteristics of the blue devices without and with CRLs with different HTLs. The current densities at a fixed voltage were decreases when the CRL was inserted, because the CRL doped with red dye has lower hole transporting property, which is same with the case of the green device. The decrement of current density depends on the material we used; for instance, the current densities of the devices B2 with Spiro-2CBP,  $\alpha$ -NPD, TAPC, BBTC, and CBP are 223 mA/cm<sup>2</sup>, 62 mA/cm<sup>2</sup>, 112 mA/cm<sup>2</sup>, 103 mA/cm<sup>2</sup>, and 100 mA/cm<sup>2</sup> at 10 V, while those of the devices B1 with Spiro-2CBP,  $\alpha$ -NPD, TAPC, BBTC, and CBP are 67 mA/cm<sup>2</sup>, 67 mA/cm<sup>2</sup>, 124 mA/cm<sup>2</sup>, 63 mA/cm<sup>2</sup>, and 13 mA/cm<sup>2</sup>, respectively. This tendency is same with the green device case. As the trap level becomes deeper, higher energy is required for the trapped carriers to escape the site [108]. In the case of Spiro-2CBP, the red dopant just disturbs the transport of hole in the Spiro-2CBP. This is similar case of BCP doped TAPC layer as previously shown in Figure 4.11. Figure 5.13 shows the driving voltage changes of blue ( $\Delta V_B$ ) devices at 1000 cd/m<sup>2</sup> by inserting the CRLs with different host materials making different hole trap levels. The increase of driving voltage is negligible in the devices with  $\alpha$ -NPD ( $\Delta V_B=0.0$  V), TAPC ( $\Delta V_B=0.1$  V) and BBTC ( $\Delta V_B=0.3$  V), but high in the devices with Spiro-2CBP ( $\Delta V_B=0.9$  V) and CBP ( $\Delta V_B=1.7$  V) due to the scattering effect and deep trap energy level of red dopant, respectively. This tendency is also same with the green device case.

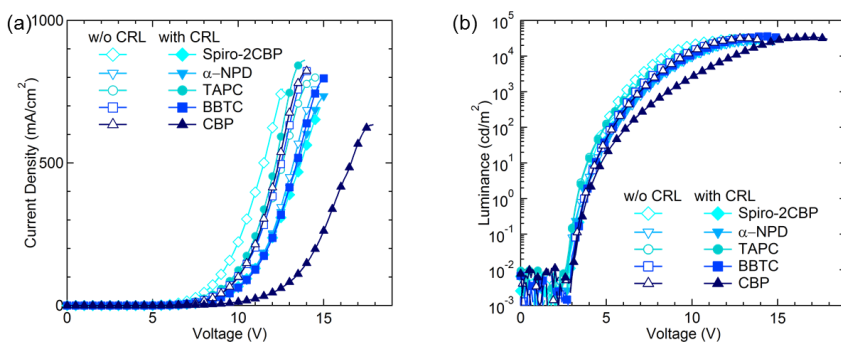


**Figure 5.12** (a) J-V and (b) L-V characteristics of the devices B1 and B2 with different HTLs.

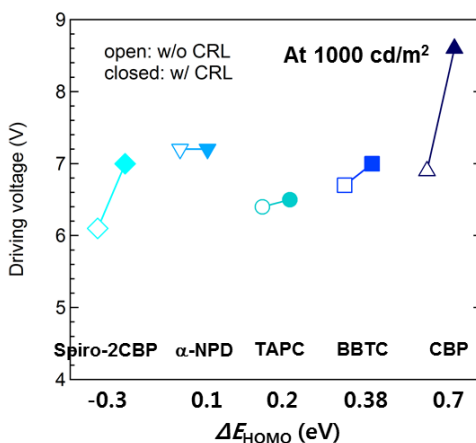


**Figure 5.13** Driving voltage changes of the blue phosphorescent devices at 1000  $\text{cd/m}^2$  with and without CRL as a function of  $\Delta E_{\text{HOMO}}$ .

Figure 5.14 shows the efficiencies of the blue devices with and without CRL with different HTLs. All devices exhibit high efficiencies based on the phosphorescent emitters; the highest EQEs of both devices B1 and B2 with

BBTC are 18.6% and 18.7% at  $\sim 0.05 \text{ mA/cm}^2$ , corresponding to 29.3 cd/A and 29.9 cd/A in LCE, respectively. Other devices show slightly lower efficiencies, but still higher than  $\sim 15\%$  in EQE. This result shows that the insertion of CRL does not severely affect the efficiency of the devices. Besides, the devices with CRL exhibit higher efficiencies compared with the devices without CRL in case of using Spiro-2CBP,  $\alpha$ -NPD, and BBTC as shown in Figure 5.14(d). We attribute this improvement with CRL to the enhanced electron-hole balance. Since the hole mobility of HTLs are generally higher than electron mobility of ETL and the electron is easily trapped in the blue EML due to the deep LUMO energy level of FIrpic compared with mCP, we can know that the hole density is higher than the electron density in the blue devices. The thin CRL slightly reduces the hole mobility in the devices due to the trap sites caused by doping the red dye as mentioned, resulting in the improved electron-hole balance and higher efficiency.

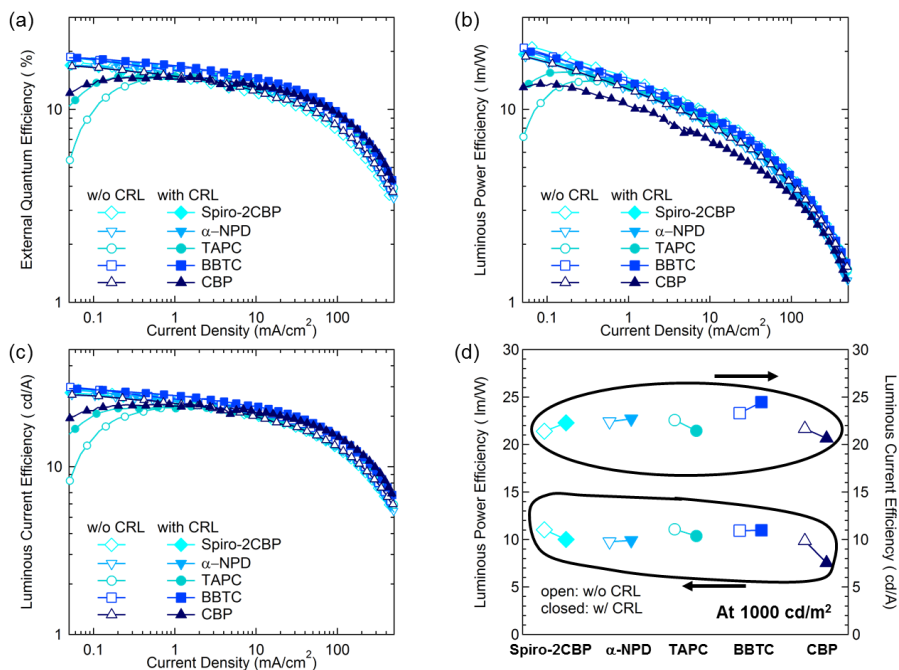


**Figure 5.14** (a) EQE, (b) LPE, (c) LCE vs J characteristics and (d) LPE and LCE at  $1000 \text{ cd}/\text{m}^2$  of the devices B1 and B2 with different HTLs.

Figure 5.15(a)–(e) show the normalized EL spectra of the devices B1 and B2 with Spiro-2CBP,  $\alpha$ -NPD, TAPC, BBTC, and CBP, respectively, as HTLs at different driving voltages. All spectra show typical EL spectrum of FIrpic with a main emission peak of  $\sim 470 \text{ nm}$ . Each device has same EL spectra regardless of driving voltage. Furthermore, the insertion of CRL rarely affects the EL spectrum of blue phosphorescent OLEDs irrespective of CRLs. The CIE color coordinates change ( $\Delta x$ ,  $\Delta y$ ) between B1 and B2 devices with Spiro-2CBP,  $\alpha$ -NPD, TAPC, BBTC, and CBP are negligible, which are (0.00, 0.00) irrespective of HTLs, at 7 V. These results indicate that the CRL can be

utilized as an HTL without distortion of EL spectra in blue phosphorescent OLEDs.

However, the EL spectra of the blue devices (B3) without EBL of TAPC layer clearly show the red peak from Ir(piq)<sub>2</sub>(acac) irrespective of HTLs, which is different from the EL spectra of device B1. This result means that the role of EBL is very important for the full-color OLEDs using CRLs without color distortion. The B3 device with TAPC host shows relatively low red emission peak compared with other devices. This result is concerned with low efficiency of R1 device with TAPC host. In other words, relatively lower red light intensity than blue light results in low red emission in the B3 device with TAPC host even though the device does not have an EBL.

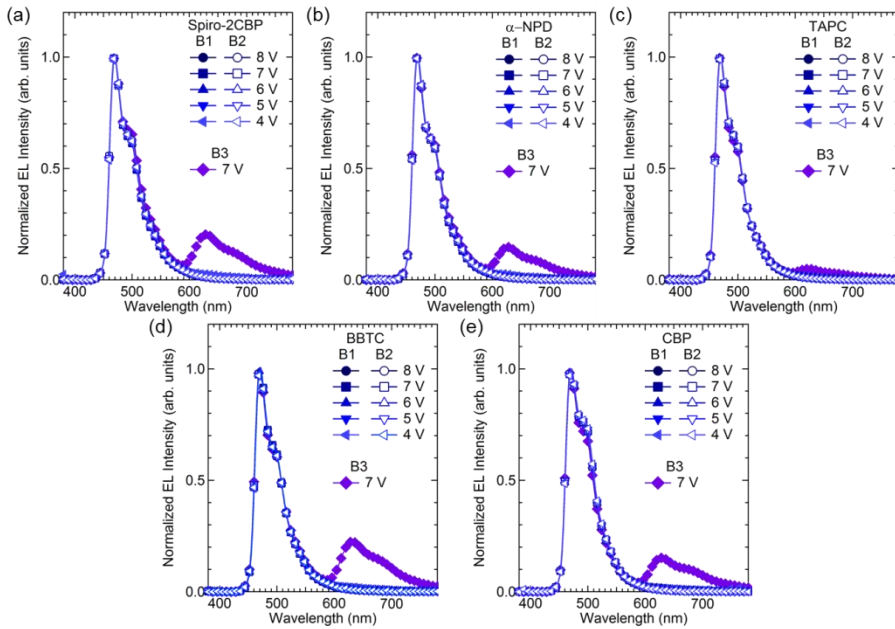


**Figure 5.15** Normalized EL spectra of the devices B1, B2, and B3 with (a) Spiro-2CBP, (b)  $\alpha$ -NPD, (c) TAPC, (d) BBTC, and (e) CBP as HTLs at different driving voltages.

The color gamut is one of significant factors for estimating quality of the full-color display. The color gamut is concerned with the number of expressing colors and the full-color device with high color gamut can display much more colors. We can generally calculate the color gamut of display using the ratio between measured triangle area from R, G, and B color coordinates and triangle area from standard color coordinates of National Television System Committee (NTSC) 1953. Figure 5.16 shows CIE1931 color coordinates of R, G, and B of each device at 8V and color gamut. The change of color coordinates is very small in the devices regardless of CRL

insertion so the change of color gamut is also negligible. For example, the area of the device with CRL using TAPC can represent 59.6% of NTSC 1953 color gamut, which is only about 1% lower than the area of the device without CRL. Therefore, we believe that the devices with CRL have enough possibility for the fabrication of full-color OLEDs.

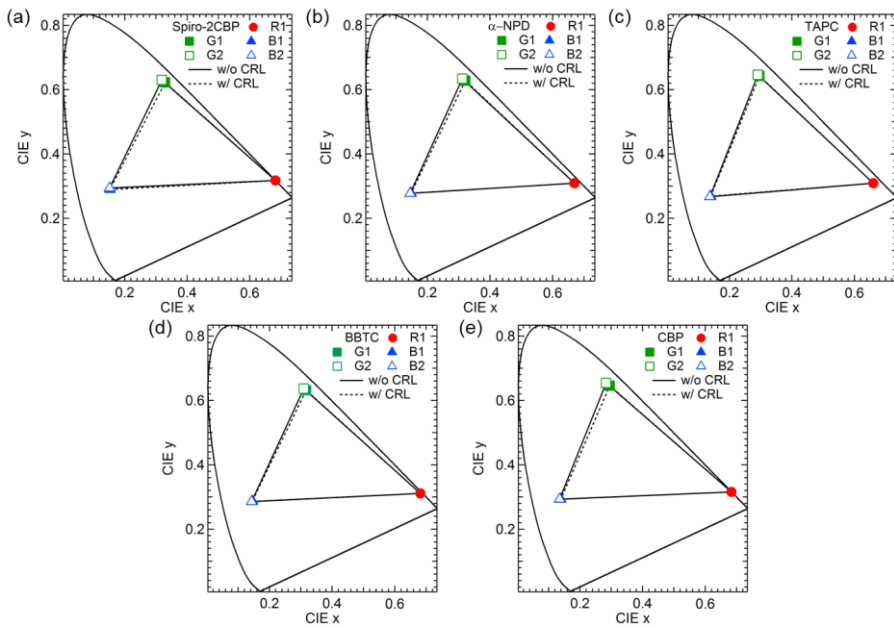


**Figure 5.16** CIE color coordinates and color gamut of the devices R1, G1, G2, B1, and B2 at 8 V with different HTLs of (a) Spiro-2CBP, (b)  $\alpha$ -NPD, (c) TAPC, (d) BBTC, and (e) CBP.

The entire performances of all devices at a practical brightness (at 1000  $\text{cd}/\text{m}^2$ ) are summarized in Table 5.1.

**Table 5.1. Performances of devices with different CRLs**

CRL Host	Device	J[a] [mA/cm <sup>2</sup> ]	Voltage[b] [V]	EQE[c] [%]	LCE[d] [cd/A]	LPE[e] [lm/W]	CIE color coordinates[f] [x, y]
Spiro-2CBP	R1	549	6.3	8.3	5.8	2.9	[0.68, 0.32]
	G1	74	6.3	13.0	43.0	21.4	[0.33, 0.63]
	G2	206	5.7	13.2	45.2	24.9	[0.32, 0.63]
	B1	67	7.0	13.7	22.3	10.0	[0.15, 0.29]
	B2	223	6.1	12.9	21.4	11.0	[0.15, 0.29]
	B3	118	6.8	11.2	16.8	78	[0.21, 0.31]
$\alpha$ -NPD	R1	407	6.7	6.1	4.3	2.0	[0.67, 0.31]
	G1	68	6.6	12.8	42.5	20.2	[0.32, 0.63]
	G2	71	6.5	12.4	42.4	20.5	[0.31, 0.63]
	B1	67	7.2	14.6	22.7	9.9	[0.15, 0.28]
	B2	62	7.2	14.2	22.4	9.8	[0.14, 0.28]
	B3	78	7.6	8.3	12.1	5.0	[0.19, 0.29]
TAPC	R1	470	6.8	3.1	2.2	1.0	[0.66, 0.61]
	G1	115	5.9	13.0	43.7	23.3	[0.30, 0.64]
	G2	112	5.9	13.1	44.7	23.8	[0.29, 0.65]
	B1	124	6.5	14.2	21.5	10.4	[0.14, 0.27]
	B2	112	6.4	14.9	22.6	11.1	[0.14, 0.27]
	B3	141	6.5	11.8	17.4	8.4	[0.16, 0.27]
BBTC	R1	492	6.5	8.4	5.4	2.6	[0.68, 0.31]
	G1	65	6.5	13.2	44.4	21.5	[0.32, 0.63]
	G2	111	6.2	12.6	43.2	21.9	[0.31, 0.64]
	B1	63	7.0	15.5	24.5	11.0	[0.14, 0.29]
	B2	103	6.7	14.6	23.3	10.9	[0.14, 0.29]
	B3	100	7.1	11.7	15.7	6.9	[0.21, 0.29]
CBP	R1	189	7.6	7.5	4.9	2.0	[0.68, 0.32]
	G1	15	7.7	12.3	41.0	16.7	[0.30, 0.65]
	G2	125	6.1	13.7	47.0	24.2	[0.28, 0.65]
	B1	13	8.6	14.0	22.5	8.1	[0.14, 0.29]
	B2	100	6.9	13.5	21.7	9.9	[0.14, 0.29]
	B3	27	8.2	11.7	16.4	6.3	[0.19, 0.29]

[a] Current density at 10 V; [b] Driving voltage for 1000 cd/m<sup>2</sup>; [c] External quantum efficiency at 1000 cd/m<sup>2</sup>; [d] Luminous current efficiency at 1000 cd/m<sup>2</sup>; [e] Luminous power efficiency at 1000 cd/m<sup>2</sup>; [f] Measured at 8 V.

## 5.2 Full-Color Inverted Bottom-Emission OLEDs with CRLs

In this part, we adapt the CRL to the inverted bottom-emission OLEDs and compare the device with CRL with the device without CRL. For both devices, we used ITO as a cathode and ZnO NPs as an EIL. Four organic materials possessing different HOMO energy levels, i.e., Spiro-2CBP, TAPC, BBTC, and CBP, were used in the HTL and the host of CRL at the same time. The CRL consists of each host material doped with Ir(piq)<sub>2</sub>(acac) (8 wt%) with the thickness of 15 nm. For efficient green- and blue- EMLs, we used CBP and mCP as a green and blue host, respectively, doped with Ir(ppy)<sub>2</sub>(acac) and Flrpic as the green and blue phosphorescent dopants, respectively. For the green and blue sub-pixels, 10 nm of TAPC layer was used next to the CRL as a triplet-exciton and electron blocking layer. As an ETL, 3TPYMB was selected owing to its proper LUMO energy level for the inverted bottom-emission OLEDs as shown in Figure 3.5 and high triplet energy level that prevents excitons from being transferred to ETL. MoO<sub>3</sub> and Al were used as the HIL and anode, respectively. To investigate the effect of the CRL in the inverted bottom-emission OLEDs, R, G, and B devices were fabricated with following structures:

R4: ITO/ZnO (~45 nm)/3TPYMB (40 nm)/**CRL**/ HTL (35 nm)/  
MoO<sub>3</sub> (10 nm)/Al (100 nm)

G4: ITO/ ZnO (~45 nm)/3TPYMB (40 nm)/

CBP:Ir(ppy)<sub>2</sub>(acac) (8 wt%, 15 nm)/EBL (10 nm)/**CRL**/ HTL (35 nm)/

MoO<sub>3</sub> (10 nm)/Al (100 nm)

G5: ITO/ ZnO (~45 nm)/3TPYMB (40 nm)/

CBP:Ir(ppy)<sub>2</sub>(acac) (8 wt%, 15 nm)/EBL (10 nm)/HTL (50 nm)/

MoO<sub>3</sub> (10 nm)/Al (100 nm)

B4: ITO/ ZnO (~45 nm)/3TPYMB (40 nm)/

mCP:FIrpic (8 wt%, 15 nm)/EBL (10 nm)/**CRL**/ HTL (35 nm)/

MoO<sub>3</sub> (10 nm)/Al (100 nm)

B5: ITO/ ZnO (~45 nm)/3TPYMB (40 nm)/

mCP:FIrpic (8 wt%, 15 nm)/EBL (10 nm)/ HTL (50 nm)/

MoO<sub>3</sub> (10 nm)/Al (100 nm)

B6: ITO/ ZnO (~45 nm)/3TPYMB (40 nm)/

mCP:FIrpic (8 wt%, 15 nm)/**CRL**/ HTL (35 nm)/MoO<sub>3</sub> (10 nm)/

Al (100 nm)

where **CRL** means the layer of HTL:Ir(piq)<sub>2</sub>(acac) (8 wt%, 15 nm) and HTLs are Spiro-2CBP, TAPC, BBTC, and CBP. The thickness of HTL in the device with CRL (i.e., G4 and B4) was reduced to 35 nm by adding the CRL (15 nm) to keep identical with the thickness of HTL without CRL (i.e., G5 and B5). The schematic energy level diagram for all materials is shown in Figure 5.17. Device R4 represents a red sub-pixel for OLEDs with using CRL, and devices

G4 and G5 stand for green sub-pixel with and without CRL, respectively. Similarly, devices B4 and B5 denote blue sub-pixel with and without CRL, while device B6 is a control device without TAPC layer (i.e., EBL) as compared to the device B4 to show the function of EBL in this CRL structure.

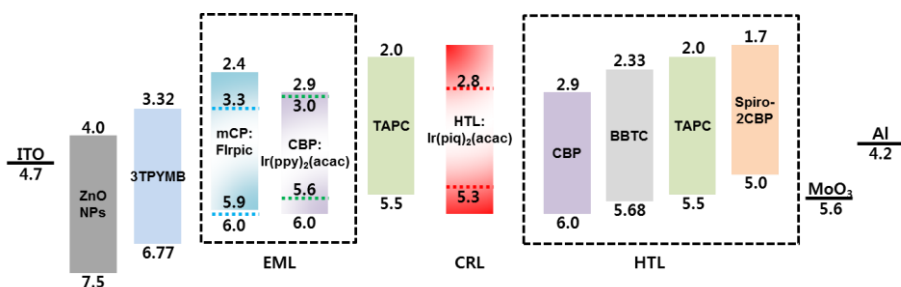


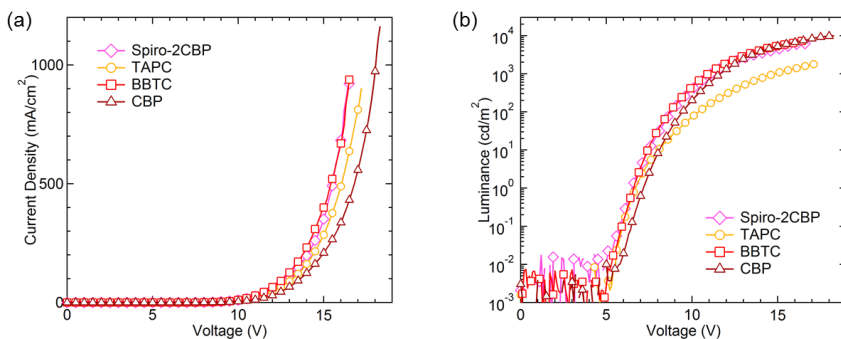
**Figure 5.17** Energy level diagram for the full-color inverted bottom-emission OLED devices.

## 5.2.1 Inverted bottom-emission red phosphorescent OLEDs with different hosts and HTLs

We tested four different host materials, which are Spiro-2CBP, TAPC, BBTC, and CBP, doped with a typical red dopant, Ir(piq)<sub>2</sub>(acac). We also utilized these red host materials as the HTL in each device for the simple device structure.

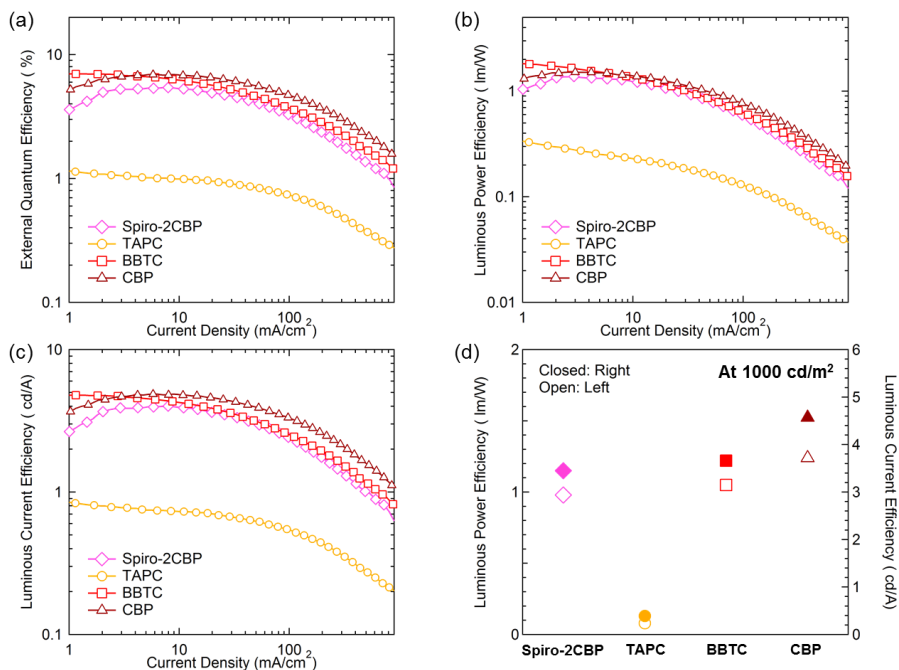
Figure 5.18 shows the J-V and L-V characteristics of the red devices with different hosts and HTLs. The devices R4 with Spiro-2CBP and BBTC show similar J-V and L-V characteristics and they have higher current density and luminance than the devices R4 with TAPC and CBP. For instance, the current

densities of the devices R4 with Spiro-2CBP, TAPC, BBTC, and CBP are 351 mA/cm<sup>2</sup>, 285 mA/cm<sup>2</sup>, 400 mA/cm<sup>2</sup>, and 209 mA/cm<sup>2</sup> at 15 V, respectively. The turn-on voltages of the devices R4 with Spiro-2CBP, TAPC, BBTC, and CBP are 6.5 V, 6.7 V, 6.6 V, and 7.2 V respectively, which roughly correspond to the descending order of HOMO energy levels of HTLs. The driving voltage of the device R4 with BBTC at 1000 cd/m<sup>2</sup> is 10.9 V which is the lowest value among those of other devices. This result is different from the case of conventional structure device. When the MoO<sub>3</sub> layer is utilized as a HIL in inverted structure, the hole injection is larger than that in conventional structure due to doping effect [66]. In other words, enhanced hole injection in the device R4 with BBTC may reduce the driving voltage of the device. The driving voltage of the device R4 with Spiro-2CBP at 1000 cd/m<sup>2</sup> is 11.1 V which is lower than that of the devices R4 with TAPC (14.8 V) and CBP (11.6 V). The device with TAPC shows comparable luminance with other devices at low driving voltage but low luminance at high driving voltage because high hole mobility and low electron mobility of TAPC and low LUMO energy level leads to accumulation of holes near the EML/ETL interface, resulting in triplet-polaron or triplet-triplet annihilation at high voltage region and resultant rapid decreases of luminance [90].



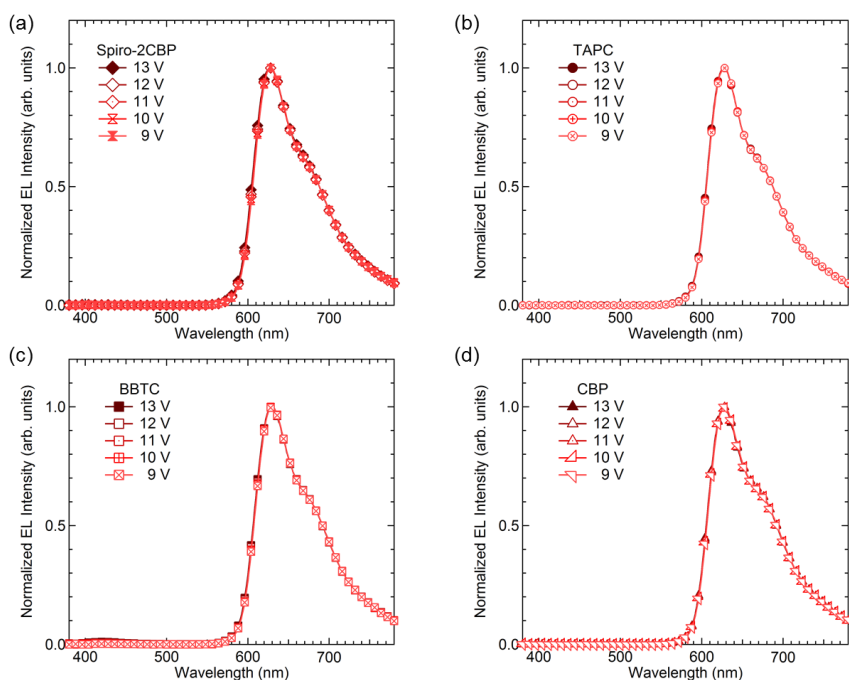
**Figure 5.18** (a) J-V and (b) L-V characteristics of the devices R4 with different hosts and HTLs.

Figure 5.19(a), (b), and (c) show the EQE, LPE, and LCE versus current density characteristics of the devices R4 with different hosts and HTLs. The devices R4 with spiro-2CBP, BBTC, and CBP have higher efficiencies than the devices R4 with TAPC. The EQEs of the devices R4 with Spiro-2CBP, TAPC, BBTC, and CBP are 4.7%, 0.5%, 5.4%, and 6.8% at 1000  $\text{cd/m}^2$ , respectively, which is not as high as the conventional structure red phosphorescent OLEDs because of low electron injection from the cathode and lower electron mobility of 3TPYMB than that of TmPyPB. Nevertheless, device R4 with BBTC and CBP exhibits the highest EQE of  $\sim 7\%$  because BBTC and CBP are good red phosphorescent host material. Figure 5.19(d) shows the LPE and LCE of the device R4 at 1000  $\text{cd/m}^2$  as a function of hosts and HTLs. The device R4 with TAPC shows especially low efficiency and rapid roll-off compared with other devices. This result is same with the case of the device R1 with TAPC.



**Figure 5.19** (a) EQE, (b) LPE, (c) LCE vs J characteristics and (d) LPE and LCE at 1000 cd/m<sup>2</sup> of the devices R4 with different hosts and HTLs.

Figure 5.20(a)–(d) show the normalized EL spectra of the devices R4 with Spiro-2CBP, TAPC, BBTC, and CBP, respectively, as hosts and HTLs at different driving voltages. All spectra show typical EL spectrum of Ir(piq)<sub>2</sub>(acac) with main emission peak of ~630 nm. Each device has same EL spectra regardless of driving voltage. The CIE color coordinates of the devices R4 with Spiro-2CBP, TAPC, BBTC, and CBP are (0.68, 0.32), (0.68, 0.32), (0.68, 0.31), and (0.68, 0.32), respectively, at 12 V, which are same with the CIE color coordinates of the devices R1 except the device R4 with TAPC. The CIE color coordinate of the device R4 with TAPC is slightly changed due to absence of parasitic peak at ~425 nm in the device R1 with TAPC.



**Figure 5.20** Normalized EL spectra of the devices R4 with (a) Spiro-2CBP, (b) TAPC, (c) BBTC, and (d) CBP as hosts and HTLs at different driving voltages.

## 5.2.2 Inverted bottom-emission green phosphorescent OLEDs with different HTLs

We compared the device G4 (with CRLs) with the device G5 (without CRLs). Figure 5.21 shows the J-V and L-V characteristics of the green devices without and with CRLs with different HTLs. The current densities at a fixed voltage were decreased when the CRL was inserted, because the CRL doped with red dye has lower hole transport property. However, the decrement of

current density highly depends on the material we used; for instance, the current density of the device G4-TAPC is almost same with the device G5-TAPC, which are 112 and 120 mA/cm<sup>2</sup> at 15 V, respectively. In case of using Spiro-2CBP, the current density of the device G4 (74 mA/cm<sup>2</sup>) is quite lower than that of the device G5 (203 mA/cm<sup>2</sup>) at 15 V. A drastic decrease of current density is observed in the devices with BBTC and CBP. The device G5-BBTC and -CBP exhibit 200 mA/cm<sup>2</sup> and 46 mA/cm<sup>2</sup> at 15 V, whereas the device G4-BBTC and CBP show 58 mA/cm<sup>2</sup> and 13 mA/cm<sup>2</sup> at the same voltage. This result means that the hole trap level of CRL is a dominant factor of transport property in inverted structure like conventional device structure. As the trap level becomes deeper, higher energy is required for the trapped carriers to escape the site. Figure 5.22 shows the driving voltage changes ( $\Delta V_G$ ) of the green devices at 1000 cd/m<sup>2</sup> by inserting the CRLs with different host materials making different hole trap levels. The increase of driving voltage is negligible in the device with TAPC ( $\Delta V_G=0.2$  V), but high in the devices with Spiro-2CBP ( $\Delta V_G=0.5$  V), BBTC ( $\Delta V_G=0.8$  V), and CBP ( $\Delta V_G=1.1$  V) due to the scattering effect and the deep trap energy levels.

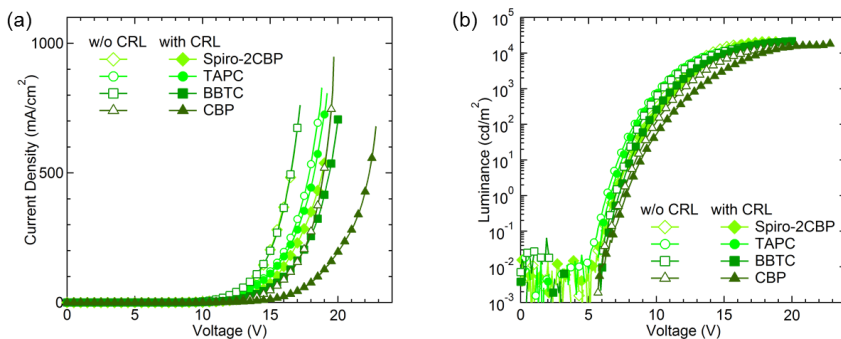


**Figure 5.21** (a) J-V and (b) L-V characteristics of the devices G4 and G5 with different HTLs.

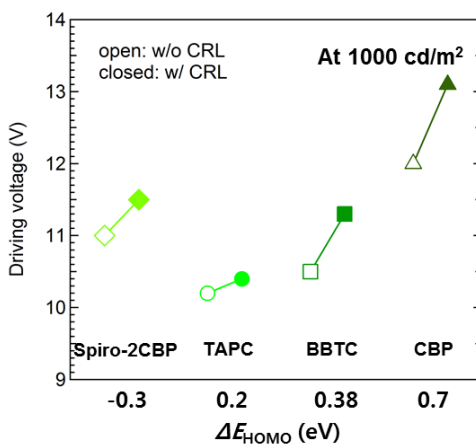


**Figure 5.22** Driving voltage changes at 1000 cd/m<sup>2</sup> with and without CRL as a function of  $\Delta E_{\text{HOMO}}$ .

Figure 5.23(a), (b), and (c) show the EQE, LPE, and LCE versus current density characteristics of the devices G4 and G5 with different HTLs. The EQEs of the devices G4 and G5 with Spiro-2CBP, TAPC, BBTC, and CBP are (5.9%, 3.5%), (7.9%, 7.6%), (7.2%, 4.4%), and (8.6%, 6.7%), respectively, at

1000 cd/m<sup>2</sup>. Overall EQEs are lower than those of the conventional structure OLEDs due to low electron injection and transport. However, all devices with CRL have higher EQEs than the devices without CRL. Most LPEs and LCEs of the devices with CRL at 1000 cd/m<sup>2</sup> are also higher than those of the devices without CRL as shown in Figure 5.23(d). This result is slightly different from a result of conventional structure device because the amounts of injected holes are higher than the amounts of injected electrons in the inverted structure OLEDs. Consequently, the insertion of CRL increases electron-hole balance from reduced hole conductivity, resulting in increases of efficiency. Since the red dopant scarcely disturbs the transport of hole in TAPC, the efficiency of the device with TAPC is almost same regardless of the insertion of CRL. From the result of efficiencies, we found that the device with CRL have an advantage of efficiency in inverted structure OLEDs.

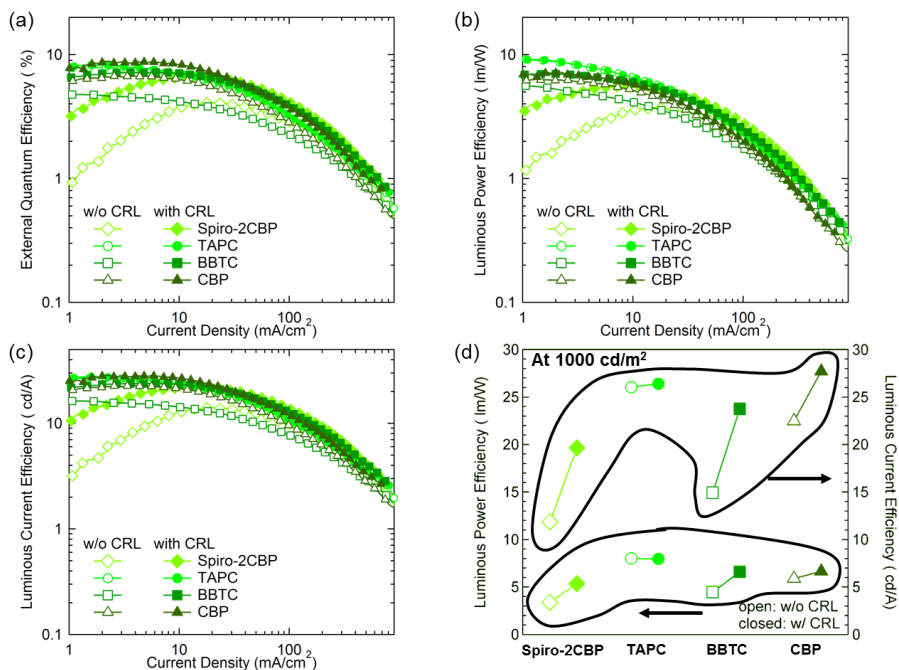


**Figure 5.23** (a) EQE, (b) LPE, (c) LCE vs J characteristics and (d) LPE and LCE at 1000 cd/m<sup>2</sup> of the devices G4 and G5 with different HTLs.

Figure 5.24(a)–(d) show the normalized EL spectra of the devices G4 and G5 with Spiro-2CBP, TAPC, BBTC, and CBP, respectively, at different driving voltages. All spectra show typical EL spectrum of Ir(ppy)<sub>2</sub>(acac) with main emission peak of ~520 nm. Each device has same EL spectra regardless of driving voltage. Moreover, the insertion of CRL rarely affects the EL spectrum of the green phosphorescent OLEDs irrespective of CRL insertion. The CIE color coordinates change ( $\Delta x$ ,  $\Delta y$ ) between the devices G4 and G5 with Spiro-2CBP, TAPC, BBTC, and CBP are negligible, which are (0.00, 0.00), (0.01, 0.01), (0.01, 0.00), and (0.00, 0.00), respectively, at 12 V. These

results indicate that CRL can be utilized as an HTL without distortion of EL spectra in the inverted bottom-emission green phosphorescent OLEDs.

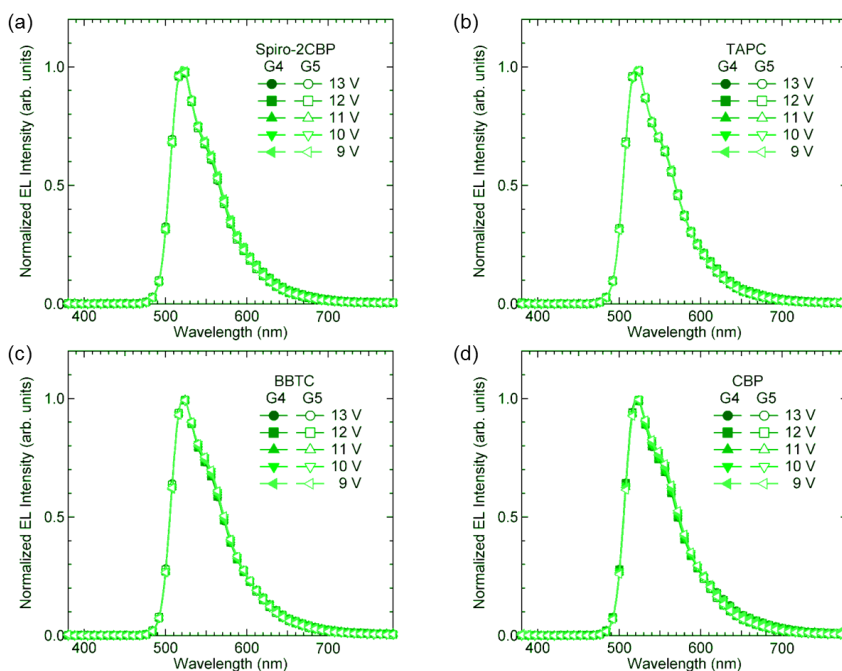


**Figure 5.24** Normalized EL spectra of the devices G4 and G5 with (a) Spiro-2CBP, (b) TAPC, (c) BBTC, and (d) CBP as HTLs at different driving voltages.

### 5.2.3 Inverted bottom-emission blue phosphorescent OLEDs with and without CRLs

We compared the device B4 (with CRLs) with the device B5 (without CRLs). Figure 5.25 shows the J-V and L-V characteristics of the blue devices without and with CRLs with different HTLs. The current densities at a fixed voltage

were decreased when the CRL was inserted, because the CRL doped with red dye has lower hole transporting property. The decrement of current density highly depends on the material we used; for instance, the current densities of the devices B5 with Spiro-2CBP, TAPC, BBTC, and CBP are 214 mA/cm<sup>2</sup>, 138 mA/cm<sup>2</sup>, 163 mA/cm<sup>2</sup>, and 61 mA/cm<sup>2</sup> at 15 V, while those of the devices B4 with Spiro-2CBP, TAPC, BBTC, and CBP are 68 mA/cm<sup>2</sup>, 119 mA/cm<sup>2</sup>, 60 mA/cm<sup>2</sup>, and 16 mA/cm<sup>2</sup>, respectively. This tendency is same with the green device case. Figure 5.26 shows the driving voltage changes ( $\Delta V_B$ ) of the blue devices at 1000 cd/m<sup>2</sup> by inserting the CRLs with different host materials making different hole trap levels. The increase of driving voltage is small in the devices with TAPC ( $\Delta V_B=0.3$  V), but high in the devices with Spiro-2CBP ( $\Delta V_B=1.2$  V), BBTC ( $\Delta V_B=1.2$  V), and CBP ( $\Delta V_B=1.2$  V) due to the scattering effect and the deep trap energy level of red dopant.

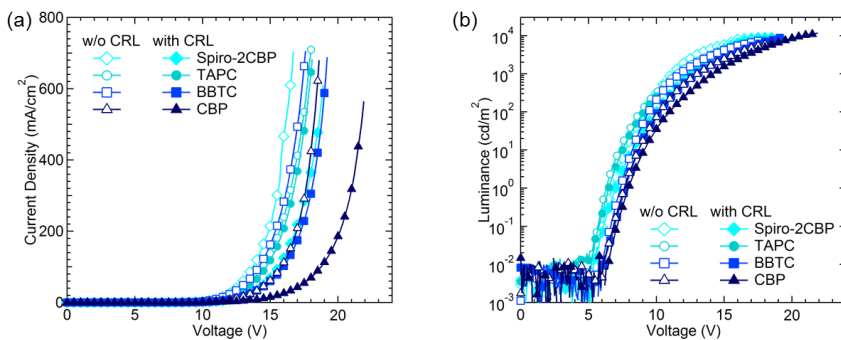


**Figure 5.25** (a) J-V and (b) L-V characteristics of the devices B4 and B5 with different HTLs.

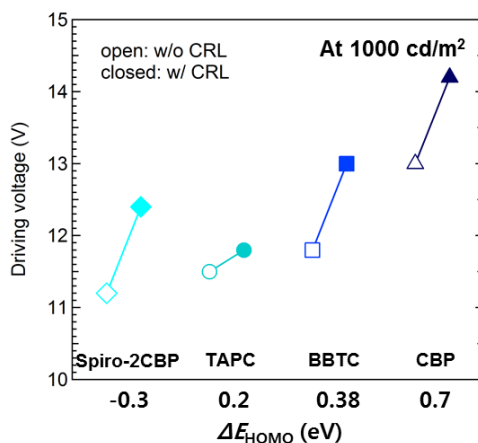


**Figure 5.26** Driving voltage changes of the devices B4 and B5 at 1000 cd/m<sup>2</sup> with and without CRL as a function of  $\Delta E_{\text{HOMO}}$ .

Figure 5.27(a), (b), and (c) show the EQE, LPE, and LCE versus current density characteristics of the devices B4 and B5 with different hosts and HTLs. The EQEs of the devices B4 and B5 with Spiro-2CBP, TAPC, BBTC, and CBP are (5.6%, 5.0%), (4.0%, 4.0%), (2.8%, 2.5%), and (5.1%, 2.7%), respectively, at 1000 cd/m<sup>2</sup>. Overall EQEs are lower than those of the conventional structure OLEDs due to low electron injection and transport. However, most devices with CRL have higher EQEs than the devices without CRL. Most LPEs and LCEs of the devices with CRL at 1000 cd/m<sup>2</sup> are also same or higher than those of the devices without CRL as shown in Figure 5.27(d). This result is similar to a result of the inverted bottom-emission green phosphorescent OLEDs because the amounts of injected holes are higher than the amounts of injected electrons in the inverted structure OLEDs. Consequently, the insertion of CRL increases electron-hole balance, resulting

in increases of efficiency. From the result of efficiencies, we found that the device with CRL also have an advantage of efficiency in the inverted structure OLEDs.

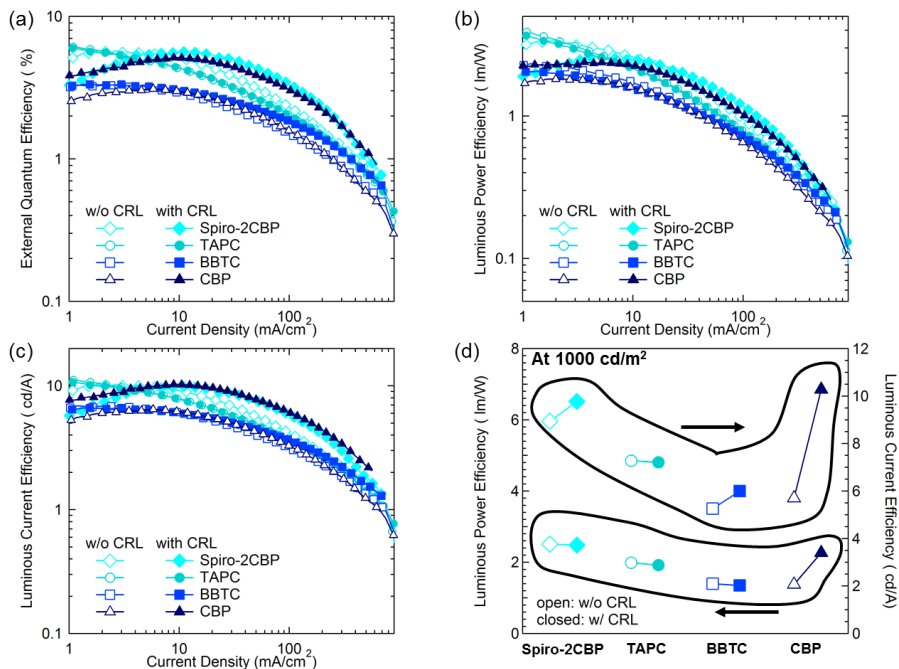


**Figure 5.27** (a) EQE, (b) LPE, (c) LCE vs J characteristics and (d) LPE and LCE at 1000 cd/m<sup>2</sup> of the devices B4 and B5 with different HTLs.

Figure 5.28(a)–(d) show the normalized EL spectra of the devices B4 and B5 with Spiro-2CBP, TAPC, BBTC, and CBP, respectively, as HTLs at different driving voltages. All spectra show typical EL spectrum of FIrpic with main emission peak of ~470 nm. Each device has same EL spectra regardless of driving voltage. However, the EL spectra of the devices with BBTC and CBP are different from those of the devices with Spiro-2CBP and TAPC. This

may be due to the fact that the devices with BBTC and CBP have different main exciton recombination regions compared with those of the devices with Spiro-2CBP and TAPC due to different charge carrier transport properties, which causes interference effect, resulting in different EL spectra. But, the insertion of CRL rarely affects the EL spectrum of the blue phosphorescent OLEDs irrespective of the CRL insertion. The CIE color coordinates change ( $\Delta x$ ,  $\Delta y$ ) between the devices B4 and B5 with Spiro-2CBP, TAPC, BBTC, and CBP are negligible which are (0.00, 0.01), (0.01, 0.00), (0.00, 0.01), and (0.00, 0.00), respectively, at 12 V. These results indicate that the CRL can be utilized as an HTL without distortion of EL spectra in the inverted bottom-emission blue phosphorescent OLEDs.

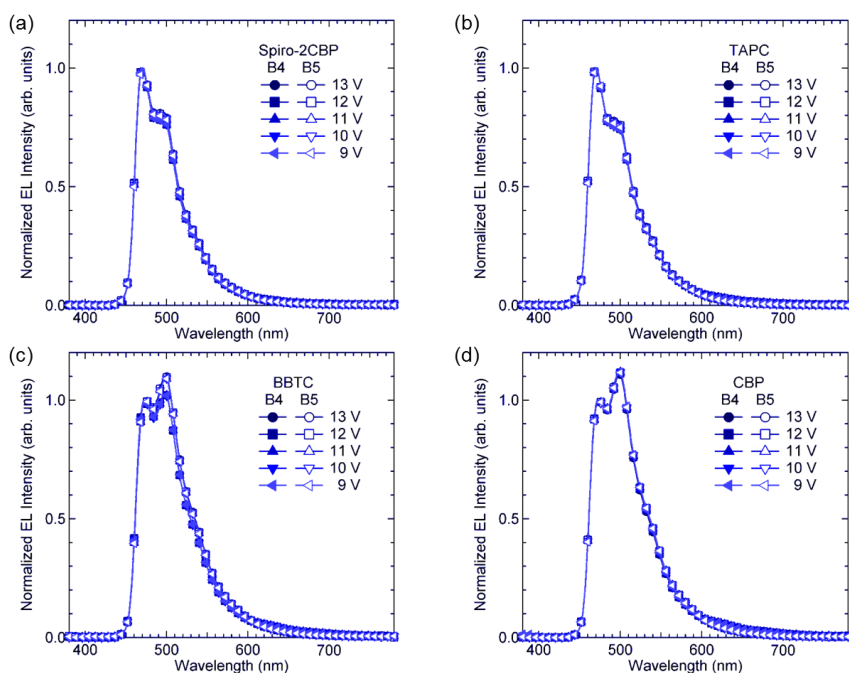


**Figure 5.28** Normalized EL spectra of the devices B4 and B5 with (a) Spiro-2CBP, (b) TAPC, (c) BBTC, and (d) CBP as HTLs at different driving voltages.

Figure 5.29 shows EL spectra of the inverted bottom-emission blue devices (B3) without the EBL of TAPC layer. The red peak from Ir(piq)<sub>2</sub>(acac) is clearly shown in the device B6 irrespective of HTLs, which is different from the EL spectra of the device B4. Therefore, the EBL is very important functional layer in the full-color inverted structure OLEDs using CRLs.

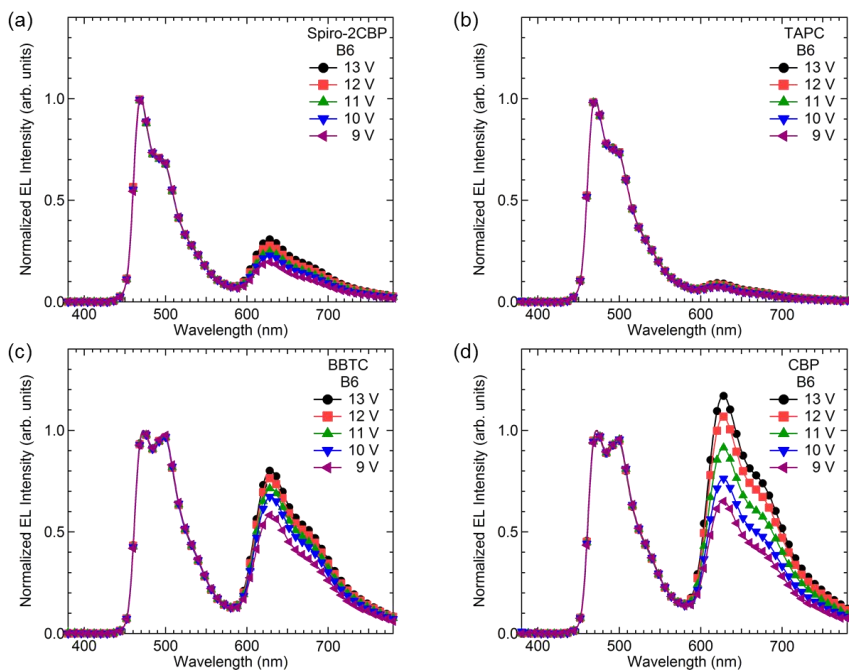


**Figure 5.29** Normalized EL spectra of the device B6 with (a) Spiro-2CBP, (b) TAPC, (c) BBTC, and (d) CBP as HTLs at different driving voltages.

Figure 5.30 shows CIE1931 color coordinates of R, G, and B of each device at 13 V and color gamut. The change of color coordinates is very small in all devices regardless of the CRL insertion so the change of color gamut is also negligible. For example, the change of NTSC 1953 color gamut of the

devices with Spiro-2CBP, TAPC, BBTC, and CBP are 0%, 0.6% (decrease), 1.6% (increase), and 0.4% (decrease), respectively. Therefore, we believe that the devices with CRL have enough possibility for the fabrication of full-color inverted structure OLEDs.

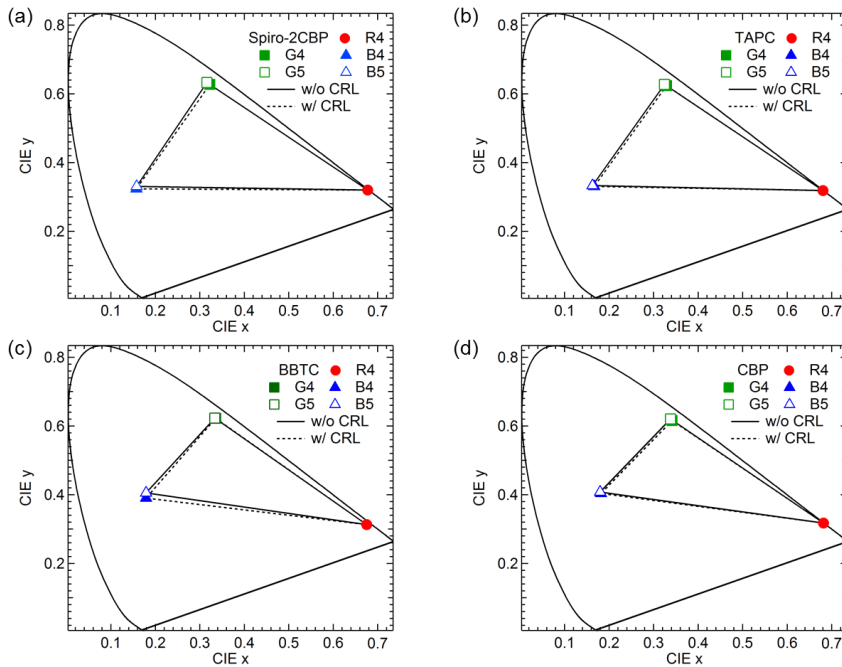


**Figure 5.30** CIE color coordinates and color gamut of the devices R4, G4, G5, B4, and B5 at 13 V with different HTLs of (a) Spiro-2CBP, (b) TAPC, (c) BBTC, and (d) CBP.

The entire performances of all devices at a practical brightness (at 1000  $\text{cd}/\text{m}^2$ ) are summarized in Table 5.2.

**Table 5.2. Performances of inverted structure devices with different CRLs**

CRL Host	Device	J[a] [mA/cm <sup>2</sup> ]	Voltage[b] [V]	EQE[c] [%]	LCE[d] [cd/A]	LPE[e] [lm/W]	CIE color coordinates[f] [x, y]
Spiro-2CBP	R4	351	11.1	4.7	3.5	1	[0.68, 0.32]
	G4	74	11.5	5.9	19.7	5.4	[0.32, 0.63]
	G5	203	11	3.5	11.9	3.4	[0.32, 0.63]
	B4	68	12.4	5.6	9.8	2.5	[0.16, 0.32]
	B5	214	11.2	5	8.9	2.5	[0.16, 0.33]
	B6	30	14.4	4.1	6	1.3	[0.25, 0.31]
TAPC	R4	285	14.8	0.5	0.4	0.1	[0.68, 0.32]
	G4	112	10.4	7.9	26.4	8	[0.33, 0.62]
	G5	120	10.2	7.6	26	8	[0.32, 0.63]
	B4	119	11.8	4	7.2	1.9	[0.17, 0.33]
	B5	138	11.5	4	7.3	2	[0.16, 0.33]
	B6	94	12.8	2.9	4.9	1.2	[0.18, 0.32]
BBTC	R4	400	10.9	5.4	3.7	1.1	[0.68, 0.31]
	G4	58	11.3	7.2	23.8	6.6	[0.34, 0.62]
	G5	200	10.5	4.4	14.9	4.5	[0.33, 0.62]
	B4	60	13	2.8	6	1.4	[0.18, 0.39]
	B5	163	11.8	2.5	5.3	1.4	[0.18, 0.41]
	B6	92	12.3	4.5	6.3	1.6	[0.33, 0.36]
CBP	R4	209	11.6	6.8	4.6	1.2	[0.68, 0.32]
	G4	13	13.1	8.6	27.7	6.7	[0.34, 0.62]
	G5	46	12	6.7	22.5	5.9	[0.34, 0.62]
	B4	16	14.2	5.1	10.3	2.3	[0.18, 0.40]
	B5	61	13	2.7	5.7	1.4	[0.18, 0.41]
	B6	32	13.5	6.2	8	1.9	[0.38, 0.35]

[a] Current density at 15 V; [b] Driving voltage for 1000 cd/m<sup>2</sup>; [c] External quantum efficiency at 1000 cd/m<sup>2</sup>; [d] Luminous current efficiency at 1000 cd/m<sup>2</sup>; [e] Luminous power efficiency at 1000 cd/m<sup>2</sup>; [f] Measured at 13 V.

## Chapter 6. Conclusion

In this thesis, inverted bottom-emission OLEDs has been studied in the view point of fabrication process and device structure. We developed and demonstrated efficient and useful inverted bottom-emission phosphorescent OLEDs using metal oxide NPs and doped HTLs.

First, the metal oxide NPs were utilized in the inverted bottom-emission OLEDs. We investigated the optical and electrical properties of ZnO NPs and SnO<sub>2</sub> NPs layers. These metal oxide NPs have many advantages for inverted bottom-emission OLEDs due to their transparency in visible spectral region, good electron transport properties, low temperature solution processibility without additional treatment, and proper energy levels for electron injection from the ITO cathode. The devices using metal oxide NPs layer as an EIL show dramatically improved performances compared with the device without metal oxide NPs layer. Furthermore, their EL spectra are nearly Lambertian emission profile. The device with ZnO NPs layer exhibits higher performance compared with the device with SnO<sub>2</sub> NPs or ZnO obtained by sol-gel method.

Next, we investigated the performance of the inverted bottom-emission OLEDs by changing the conductivity of HTLs. For that, we developed *p*-type doped HTL using MoO<sub>3</sub> doped TAPC layer. The MoO<sub>3</sub> doping increases the hole injection and conductivity of the TAPC layer and 25 vol% doping shows the highest conductivity among MoO<sub>3</sub> doped TAPC layer with various doping concentrations. We decrease driving voltage and increase power efficiency of

the white OLEDs by using this *p*-type doped HTL. When this *p*-type doped HTL is used in the inverted bottom-emission OLEDs, the driving voltage of the device reduces but efficiency decreases due to electron-hole imbalance. In contrast, the efficiency of the inverted bottom-emission OLEDs with BCP doped TAPC layer is improved because BCP doping reduces the hole conductivity of the TAPC layer. Although the BCP doped TAPC layer slightly increases driving voltage of the inverted device, we achieved the highest EQE of 8.6% without other optical light extraction techniques or *n*-type doping method in reported values of inverted white OLEDs.

Finally, we inserted red phosphorescent dye doped HTL between the undoped HTL and the EBL for controlling hole current. We investigated the performances of the devices with CRLs using five different hosts and HTLs which are Sprio-2CBP,  $\alpha$ -NPD, TAPC, BBTC, and CBP. These five materials have different HOMO energy levels so they form different trap energy levels with a red dopant. Most device characteristics depend on the trap energy level, and the driving voltage of the device is increased as the trap energy level increases. But, the changes of efficiency and color coordinates are negligible. In addition, the efficiency of the inverted device is enhanced by inserting the CRL due to improved electron-hole balance. Proper selection of materials for host of CRL can make the full-color OLEDs with CRL without driving voltage increase, efficiency degradation, and color distortion.

We believe that the device design and the fabrication method of this thesis can be helpful for simple, low-cost, and large-size full-color OLEDs displays.

## Bibliography

- [1] M. Pope, H. P. Kallmann and P. Magnante, *J. Chem. Phys.* **38**, 2042 (1963).
- [2] N. V. Vityuk and V. V. Mikho, *Sov. Phys. Semicond.* **6**, 1479 (1973).
- [3] P. S. Vincett, W. A. Barlow, R. A. Hann, and G. G. Roberts, *Thin Solid Films* **94**, 171 (1982).
- [4] R. H. Partridge, *Polymer* **24**, 748 (1983).
- [5] C. W. Tand and S. A. VanSlyke, *Appl. Phys. Lett.* **51**, 913 (1987).
- [6] C. W. Tang, S. A. VanSlyke, and C. H. Chen, *J. Appl. Phys.* **65**, 3610 (1989).
- [7] J. H. Burroughes, D. D. C. Bradley, A. R. Brown, R. N. Marks, K. Mackay, R. H. Friend, P. L. Burns, and A. B. Holmes, *Nature* **347**, 539 (1990).
- [8] J. Kido, K. Hongawa, K. Okuyama, and K. Nagai, *Appl. Phys. Lett.* **64**, 815 (1994).
- [9] M. A. Baldo, D. F. O'Brien, Y. You, A. Shoustikov, S. Sibley, M. E. Thompson, and S. R. Forrest, *Nature* **395**, 151 (1998).
- [10] J. Kido, T. Matsumoto, T. Nakada, J. Endo, K. Mori, N. Kawamura, and A. Yokoi, *SID Int. Symp. Dig. Tech. Papers* **34**, 964 (2003).
- [11] K. Walzer, B. Maenning, M. Pfeiffer, and K. Leo, *Chem. Rev.* **107**, 1233 (2007).
- [12] <http://www.idemitsu.com/products/electronic/el/performance.html>

- [13] <http://www.universaldisplay.com/default.asp?contentID=604>
- [14] B. W. D'Andrade and J. J. Brown, *Appl. Phys. Lett.* **88**, 192908 (2006).
- [15] S. Möller and S. R. Forrest, *J. Appl. Phys.* **91**, 3324 (2002).
- [16] N. Nakamura, N. Fukumoto, F. Sinapi, N. Wada, Y. Aoki, and K. Maeda, *SID Int. Symp. Dig. Tech. Papers* **40**, 603 (2009).
- [17] Y. Sun and S. R. Forrest, *Nat. Photonics* **2**, 483 (2008).
- [18] S. Reineke, F. Lindner, G. Schwartz, N. Seidler, K. Walzer, B. Lüssem, and K. Leo, *Nature* **459**, 234 (2009).
- [19] K. Yamae, H. Tsuju, V. Kittichungchit, and Y. Matsuhisa, *SID Int. Symp. Dig. Tech. Papers* **43**, 694 (2012).
- [20] C.-W. Han, K.-M. Kim, S.-J. Bae, H.-S. Choi, J.-M. Lee, T.-S. Kim, Y.-H. Tak, S.-Y. Cha, and B.-C. Ahn, *SID Int. Symp. Dig. Tech. Papers* **43**, 279 (2012).
- [21] M. Stewart, R. S. Howell, L. Pires, and M. K. Hatalis, *IEEE Trans. Electron Devices* **48**, 845 (2001).
- [22] Z. Meng, H. Chen, C. Qiu, L. Wang, H. S. Kwok, and M. Wong, *Tech. Dig. – Int. Electron Devices Meet.* **2000**, 611 (2000).
- [23] P. Servati, S. Prakash, A. Nathan, and C. Py, *J. Vac. Sci. Technol. A* **20**, 1374 (2002).
- [24] Y. He, R. Hattori, and J. Kanicki, *IEEE Trans. Electron Devices* **48**, 1322 (2001).
- [25] H.-N. Lee, J. Kyung, S. K. Kang, D. Y. Kim, M.-C. Sung, S.-J. Kim, C. N. Kim, H. G. Kim, and S. Kim, *SID Int. Symp. Dig. Tech. Papers* **38**, 1826 (2007).

- [26] H.-H. Hsieh, T.-T. Tsai, C.-Y. Chang, H.-H. Wang, J.-Y. Huang, S.-F. Hsu, Y.-C. Wu, T.-C. Tsai, C.-S. Chuang, L.-H. Chang, and Y.-H. Lin, *SID Int. Symp. Dig. Tech. Papers* **41**, 140 (2010).
- [27] K. Hong, K. Kim, and J.-L. Lee, *Appl. Phys. Lett.* **95**, 213307 (2009).
- [28] M. Thomschke, S. Hofmann, S. Olthof, M. Anderson, H. Kleemann, M. Schober, B. Lüssem, and K. Leo, *Appl. Phys. Lett.* **98**, 083304 (2011).
- [29] T. Dobbertin, M. Kroeger, D. Heithecker, D. Schneider, D. Metzdorf, H. Neuner, E. Becker, H.-H. Johannes, and W. Kowalsky, *Appl. Phys. Lett.* **82**, 284 (2003).
- [30] V. Bulović, P. Tian, P. E. Burrows, M. R. Gokhale, S. R. Forrest, and M. E. Thompson, *Appl. Phys. Lett.* **70**, 2954 (1997).
- [31] C.-W. Chen, C.-L. Lin, and C.-C. Wu, *Appl. Phys. Lett.* **85**, 2469 (2004).
- [32] H. W. Choi, S. Y. Kim, W.-K. Kim, and J.-L. Lee, *Appl. Phys. Lett.* **87**, 082102 (2005).
- [33] Q. Wang, Z. Deng, and D. Ma, *Opt. Express* **17**, 17269 (2009).
- [34] C. Yun, H. Cho, H. Kang, Y. M. Lee, Y. Park, and S. Yoo, *Appl. Phys. Lett.* **95**, 053301 (2009).
- [35] T. Dobbertin, O. Werner, J. Meyer, A. Kammoun, D. Schneider, T. Riedl, E. Becker, H.-H. Johannes, and W. Kowalsky, *Appl. Phys. Lett.* **83**, 5071 (2003).
- [36] L. S. Liao, L. S. Hung, W. C. Chan, X. M. Ding, T. K. Sham, I. Bello, C. S. Lee, and S. T. Lee, *Appl. Phys. Lett.* **75**, 1619 (1999).
- [37] L. Hou, F. Huang, W. Zeng, J. Peng, and Y. Cao, *Appl. Phys. Lett.* **87**, 153509 (2005).

- [38] S.-W. Park, J.-M. Choi, E. Kim, and S. Im, *Appl. Surf. Sci.* **244**, 439 (2005).
- [39] X. Zhu, J. Sum, H. Peng, M. Wong, and H.-S. Kwok, *SID Int. Symp. Dig. Tech. Papers* **36**, 793 (2005).
- [40] T. Miyashita, S. Naka, H. Okada, and H. Onnagawa, *Proceedings IDW'04* (2004), p. 1421.
- [41] T.-Y. Chu, S.-Y. Chen, J.-F. Chen, and C. H. Chen, *Jpn. J. Appl. Phys., Part 1* **45**, 4948 (2006).
- [42] X. Zhou, M. Pfeiffer, J. S. Huang, J. Blochwitz-Nimoth, D. S. Qin, A. Werner, J. Drechsel, B. Maenning, and K. Leo, *Appl. Phys. Lett.* **81**, 922 (2002).
- [43] T.-Y. Chu, J.-F. Chen, S.-Y. Chen, C.-J. Chen, and C. H. Chen, *Appl. Phys. Lett.* **89**, 053503 (2006).
- [44] S.-Y. Chen, T.-Y. Chu, J.-F. Chen, C.-Y. Su, and C. H. Chen, *Appl. Phys. Lett.* **89**, 053518 (2006).
- [45] T. Xiong, F. Wang, X. Qiao, and D. Ma, *Appl. Phys. Lett.* **92**, 263305 (2008).
- [46] J.-H. Lee, P.-S. Wang, H.-D. Park, C.-I. Wu, and J.-J. Kim, *Org. Electron.* **12**, 1763 (2011).
- [47] B. W. D'Andrade, S. R. Forrest, and A. B. Chwang, *Appl. Phys. Lett.* **83**, 3858 (2003).
- [48] G. Parthasarathy, C. Shen, A. Kahn, and S. R. Forrest, *J. Appl. Phys.* **89**, 4986 (2001).

- [49] J.-H. Lee, J. W. Kim, S.-Y. Kim, S.-J. Yoo, J.-H. Lee, and J.-J. Kim, *Org. Electron.* **13**, 545 (2012).
- [50] C. Zhong, S. Liu, F. Huang, H. Wu, and Y. Cao, *Chem. Mater.* **23**, 4870 (2011).
- [51] D. Kabra, L. P. Lu, M. H. Song, H. J. Snaith, and R. H. Friend, *Adv. Mater.* **22**, 3194 (2010).
- [52] J. W. Ryan, E. Palomares, and E. Martínez-Ferrero, *J. Mater. Chem.* **21**, 4774 (2011).
- [53] H. J. Bolink, E. Coronado, D. Repetto, M. Sessolo, E. M. Barea, J. Bisquert, G. Garcia-Belmonte, J. Prochazka, and L. Kavan, *Adv. Funct. Mater.* **18**, 145 (2008).
- [54] N. Tokmoldin, N. Griffiths, D. D. C. Bradley, and S. A. Haque, *Adv. Mater.* **21**, 3475 (2009).
- [55] S. K. Hau, H.-L. Yip, and A. K.-Y. Jen, *Polym. Rev.* **50**, 474 (2010).
- [56] M. Sessolo and H. J. Bolink, *Adv. Mater.* **23**, 1829 (2011).
- [57] J. S. Park, B. R. Lee, J. M. Lee, J.-S. Kim, S. O. Kim, and M. H. Song, *Appl. Phys. Lett.* **96**, 243306 (2010).
- [58] H. S. Lee, D. H. Kim, J. H. Cho, M. Hwang, Y. Jang, and K. Cho, *J. Am. Chem. Soc.* **130**, 10556 (2008).
- [59] J. Meyer, T. Winkler, S. Hamwi, S. Schmale, H.-H. Johannes, T. Weimann, P. Hinze, W. Kowlasky, and T. Riedl, *Adv. Mater.* **20**, 3839 (2008).
- [60] M. Pfeiffer, S. R. Forrest, X. Zhou, and K. Leo, *Org. Electron.* **4**, 21 (2003).

- [61] The synthesis of ZnO nanoparticles used in this thesis was conducted by *Dr. Insun Park, Jaehoon Lim, Prof. Do Yeung Yoon, Prof. Seonghoon Lee, and Prof. Kookheon Char* in Seoul National University.
- [62] C. Pacholski, A. Kornowski, and H. Weller, *Angew. Chem. Int. Ed.* **41**, 1188 (2002).
- [63] J. Y. Kim, S. Noh, D. Lee, P. K. Nayak, Y. Hong, and C. Lee, *J. Nanosci. Nanotechnol.* **11**, 5995 (2011).
- [64] H. Lee, I. Park, J. Kwak, D. Y. Yoon, and C. Lee, *Appl. Phys. Lett.* **96**, 153306 (2010).
- [65] D. Tanaka, T. Takeda, T. Chiba, S. Watanabe, and J. Kido, *Chem. Lett.* **36**, 262 (2007).
- [66] C. E. Small, S.-W. Tsang, J. Kido, S. K. So, and F. So, *Adv. Funct. Mater.* **22**, 3261 (2012).
- [67] H. Riel, S. Karg, T. Beierlein, B. Ruhstaller, and W. Rieß, *Appl. Phys. Lett.* **82**, 466 (2003).
- [68] H. Lee, J. Kwak, C. Lee, I. Park, and D. Y. Yoon, *SID Int. Symp. Dig. Tech. Papers* **41**, 1849 (2010).
- [69] J. Lee, N. Chopra, S.-H. Eom, Y. Zheng, J. Xue, F. So, and J. Shi, *Appl. Phys. Lett.* **93**, 123306 (2008).
- [70] M. A. Baldo, C. Adachi, and S. R. Forrest, *Phys. Rev. B* **62**, 10967 (2000).
- [71] S. Gubbala, V. Chakrapani, V. Kumar, and M. K. Sunkara, *Adv. Funct. Mater.* **18**, 2411 (2008).

- [72] V. Wood, M. J. Panzer, J. E. Halpert, J.-M. Caruge, M. G. Bawendi, and V. Bulović, *ACS Nano* **3**, 3581 (2009).
- [73] K. Goushi, R. Kwong, J. J. Brown, H. Sasabe, and C. Adachi, *J. Appl. Phys.* **95**, 7798 (2004).
- [74] M. Pfeiffer, K. Leo, X. Zhou, J. S. Huang, M. Hofmann, A. Werner, and J. Blochwitz-Nimoth, *Org. Electron.* **4**, 89 (2003).
- [75] X. Qiao, J. Chen, X. Li, and D. Ma, *J. Appl. Phys.* **107**, 104505 (2010).
- [76] M. Kröger, S. Hamwi, J. Meyer, T. Riedl, W. Kowalsky, and A. Kahn, *Org. Electron.* **10**, 932 (2009).
- [77] S. Hamwi, J. Meyer, T. Winkler, T. Riedl, and W. Kowalsky, *Appl. Phys. Lett.* **94**, 253307 (2009).
- [78] C.-I. Wu, C.-T. Lin, G.-R. Lee, T.-Y. Cho, C.-C. Wu, and T.-W. Pi, *J. Appl. Phys.* **105**, 033717 (2009).
- [79] J. Yun, J. Yang, Y. Hong, and C. Lee, *J. Korean Phys. Soc.* **53**, 1660 (2008).
- [80] F. Wang, X. Qiao, T. Xiong, and D. Ma, *J. Appl. Phys.* **105**, 084518 (2009).
- [81] J. Endo, T. Matsumoto, and J. Kido, *Jpn. J. Appl. Phys.* **41**, L358 (2002).
- [82] W.-J. Shin, J.-Y. Lee, J. C. Kim, T.-H. Yoon, T.-S. Kim, and O.-K. Song, *Org. Electron.* **9**, 333 (2008).
- [83] H. Lee, S. W. Cho, K. Han, P. E. Jeon, C.-N. Whang, K. Jeong, K. Cho, and Y. Yi, *Appl. Phys. Lett.* **93**, 043308 (2008).

- [84] C. Y. H. Chan, C. M. Chow, and S. K. So, *Org. Electron.* **12**, 1454 (2011).
- [85] G. He, M. Pfeiffer, K. Leo, M. Hofmann, J. Bimstock, R. Pudzich, and J. Salbeck, *Appl. Phys. Lett.* **85**, 3911 (2004).
- [86] J. Lee, J.-I. Lee, and H. Y. Chu, *Synth. Met.* **159**, 991 (2009).
- [87] P. Chen, L. Zhang, Y. Duan, W. Xie, Y. Zhao, J. Hou, S. Liu, and B. Li, *J. Phys. D: Appl. Phys.* **42**, 055115 (2009).
- [88] N. Chopra, J. Lee, Y. Zheng, S.-H. Eom, J. Xue, and F. So, *Appl. Phys. Lett.* **93**, 143307 (2008).
- [89] C.-H. Hsiao, S.-W. Liu, C.-T. Chen, and J.-H. Lee, *Org. Electron.* **11**, 1500 (2010).
- [90] S. Reineke, K. Walzer, and K. Leo, *Phys. Rev. B* **75**, 125328 (2007).
- [91] P. M. Borsenberger and H. Bässler, *J. Chem. Phys.* **95**, 5327 (1991).
- [92] B. W. D'Andrade and S. R. Forrest, *Adv. Mater.* **16**, 1585 (2004).
- [93] The spectrum simulation program was made by Ms. SuYeon Park, Hyunkoo Lee, and Prof. Changhee Lee in Seoul National University.
- [94] C. H. Lee, Y. C. Shin, D. S. Kwon, and H. K. Lee, *Proc. of SPIE* **5937**, 593719 (2005).
- [95] T.-Y. Chu, J.-F. Chen, S.-Y. Chen, and C. H. Chen, *Appl. Phys. Lett.* **89**, 113502 (2006).
- [96] M. Thomschke, R. Nitsche, M. Furno, and K. Leo, *Appl. Phys. Lett.* **94**, 083303 (2009).
- [97] Q. Wang, Z. Deng, J. Chen, and D. Ma, *Opt. Lett.* **35**, 462 (2010).

- [98] T. Matsumoto, T. Yoshinaga, T. Higo, T. Imai, T. Hirano, and T. Sasaoka, *SID Int. Symp. Dig. Tech. Papers* **42**, 924 (2011).
- [99] M. H. Kim, M. W. Song, S. T. Lee, H. D. Kim, J. S. Oh, and H. K. Chung, *SID Int. Symp. Dig. Tech. Papers* **37**, 135 (2006).
- [100] S. Chen and H.-S. Kwok, *Org. Electron.* **13**, 31 (2012).
- [101] Q. Wang, J. Ding, D. Ma, Y. Cheng, L. Wang, X. Jing, and F. Wang, *Adv. Funct. Mater.* **19**, 84 (2009).
- [102] R. J. Holmes, B. W. D'Andrade, S. R. Forrest, X. Ren, J. Li, and M. E. Thompson, *Appl. Phys. Lett.* **83**, 3818 (2003).
- [103] J.-H. Jou, S.-M. Shen, S.-H. Chen, M.-H. Wu, W.-B. Wang, H.-C. Wang, C.-R. Lin, Y.-C. Chou, P.-H. Wu, and J.-J. Shyue, *Appl. Phys. Lett.* **96**, 143306 (2010).
- [104] J. Kwak, Y.-Y. Lyu, H. Lee, B. Choi, K. Char, and C. Lee, *J. Mater. Chem.* **22**, 6351 (2012).
- [105] H. Matsushima, S. Naka, H. Okada, and H. Onnagawa, *Curr. Appl. Phys.* **5**, 305 (2005).
- [106] R. J. Holmes, S. R. Forrest, Y.-J. Tung, R. C. Kwong, J. J. Brown, S. Garon, and M. E. Thompson, *Appl. Phys. Lett.* **82**, 2422 (2003).
- [107] S.-J. Su, T. Chiba, T. Takeda, and J. Kido, *Adv. Mater.* **82**, 2422 (2003).
- [108] H. H. Fong, K. C. Lun, and S. K. So, *Chem. Phys. Lett.* **353**, 407 (2002).
- [109] Y. Lv, P. Zhou, N. Wei, K. Peng, J. Yu, B. Wei, Z. Wang, and C. Li, *Org. Electron.* **14**, 124 (2013).

## Publication

### [1] SCI(E) Journal Papers

1. **Hyunkoo Lee**, Insun Park, Jeonghun Kwak, Do Y. Yoon, and Changhee Lee, "Improvement of electron injection in inverted bottom-emission blue phosphorescent organic light emitting diodes using zinc oxide nanoparticles," *Applied Physics Letters* **96**, 153306 (2010).
2. Chan-mo Kang, Hyunduck Cho, **Hyunkoo Lee**, and Changhee Lee, "Organic Rectifier with Transfer-printed Metal as a Top Electrode," *Journal of the Korean Physical Society* **59**, 470 (2011).
3. **Hyunkoo Lee**, Jun Young Kim, and Changhee Lee, "Improvement of Power Efficiency in Phosphorescent White Organic Light-Emitting Diodes Using p-Doped Hole Transport Layer," *International Journal of Photoenergy* **2012**, 581421 (2012).
4. Jeonghun Kwak, Yi-Yeol Lyu, **Hyunkoo Lee**, Bonggoo Choi, Kookheon Char, and Changhee Lee, "New carbazole-based host material for low-voltage and highly efficient red phosphorescent organic light emitting diodes," *Journal of Materials Chemistry* **22**, 6351 (2012).
5. Jeonghun Kwak, Yi-Yeol Lyu, Seunguk Noh, **Hyunkoo Lee**, Myeongjin Park, Bonggoo Choi, Kookheon Char, Changhee Lee,

“Hole transport materials with high glass transition temperatures for highly stable organic light-emitting diodes,” *Thin Solid Films* **520**, 7157 (2012).

6. Jun Young Kim, **Hyunkoo Lee**, Jungho Park, Donggu Lee, Hyung-Jun Song, Jeonghun Kwak, Changhee Lee, “Effect of Sol-Gel-Derived ZnO Interfacial Layer on the Photovoltaic Properties of Polymer Solar Cells,” *Japanese Journal of Applied Physics* **51**, 10NE29 (2012).
7. **Hyunkoo Lee**, Hyuk Ahn, Changhee Lee, Jeonghun Kwak, “Efficient inverted bottom-emission blue phosphorescent organic light-emitting diodes with ytterbium-doped electron injection layer,” *Journal of the Korean Physical Society* **61**, 1536 (2012).
8. **Hyunkoo Lee**, Yongwon Kwon, and Changhee Lee, “Improved performances in organic and polymer light-emitting diodes using solution-processed vanadium pentoxide as a hole injection layer,” *Journal of the Society for Information Display*, online published (Dec, 2012).
9. **Hyunkoo Lee**, Chan-mo Kang, Myeongjin Park, Jeonghun Kwak, and Changhee Lee, “Improved Efficiency of Inverted Organic Light-Emitting Diodes using Tin Dioxide Nanoparticles as an Electron Injection Layer,” *ACS Applied Materials & Interfaces*, submitted.
10. **Hyunkoo Lee**, Jeonghun Kwak, Chan-Mo Kang, Yi-Yeol Lyu, Kookheon Char, and Changhee Lee, “Reduction of a red fine metal

shadow mask using common red layer for full-color organic light-emitting diodes,” *Advanced Functional Materials*, submitted.

[2] KCI Journal Papers

1. Jeonghun Kwak, Yi-Yeol Lyu, **Hyunkoo Lee**, Kookheon Char, and Changhee Lee, “Fluorescent white OLEDs with a high color-rendering index using a silicon-cored anthracene derivative as a blue host,” *Journal of Information Display* **11**, 123 (2010).
2. **Hyunkoo Lee**, Hyuk Ahn, and Changhee Lee, “Device characteristics of blue phosphorescent organic light-emitting diodes depending on the electron transport materials,” *Journal of Information Display* **12**, 219 (2011).

### [3] Conferences

1. Heume-Il Baek, Seunguk Noh, **Hyunkoo Lee**, C. K. Suman, and Changhee Lee, "Conduction Properties of Phosphorescent Emitting Layers and Their Application to Optimizing White OLEDs," *International Meeting on Information Display 2009*, p.182, Kintex, Korea, Oct 12-16 (2009).
2. **Hyunkoo Lee** and Changhee Lee, "Color stable and Efficient White Organic Light Emitting Diodes with Phosphorescent Emitters," *International Meeting on Information Display 2009*, p.84, Kintex, Korea, Oct 12-16 (2009).
3. **Hyunkoo Lee** and Changhee Lee, "Investigation of Transport Properties in Polymer/Fullerene Blends using Transient Electroluminescence Technique," *Materials Research Society 2009 Fall Meeting*, Boston, USA, Nov 30 - Dec 4 (2009).
4. **Hyunkoo Lee**, Jeonghun Kwak, Changhee Lee, Insun Park, Do Y. Yoon, "Highly Efficient Inverted Bottom-Emission OLEDs with ZnO Nanoparticles as the Electron-Injection Layer," *48th SID International Symposium, Seminar & Exhibition*, May. 23, Seattle, USA, P.160 (2010).
5. **Hyunkoo Lee**, Jeonghun Kwak, Insun Park, Sangtaek Noh, Do Y. Yoon, and Changhee Lee, "Highly Efficient Inverted Bottom-Emission White Organic Light Emitting Diodes," *International*

*Meeting on Information Display 2010*, p.212, Kintex, Korea, Oct 11-15 (Oct, 2010).

6. **Hyunkoo Lee**, Jungjin Yang, Hyuk Ahn, and Changhee Lee, “Improvement of power efficiency of phosphorescent white organic light-emitting diodes with p-doped hole transport layer,” *8th International Conference on Electroluminescence & Organic Optoelectronics (ICEL 2010)*, p.51, University of Michigan, Ann Arbor, USA, Oct.17~21 (Oct, 2010).
7. **Hyunkoo Lee**, Hyuk Ahn and Changhee Lee, “Highly Efficient Inverted Organic Light-Emitting Diodes with Tin Dioxide Nanoparticles as an Electron Injection Layer,” *The 22nd International Conference on Molecular Electronics and Devices*, Pohang, Korea, May.19~20 (May, 2011).
8. **Hyunkoo Lee**, Jeonghun Kwak, Jaehoon Lim, Kookheon Char, Seonghoon Lee and Changhee Lee, “Improvement of efficiency in inverted bottom-emission white OLEDs by doping the hole transport layer,” *69th DEVICE RESEARCH CONFERENCE*, Conference Digest p.95, UCSB, USA (Jun, 2011).
9. Myeongjin Park, Hyunduck Cho, **Hyunkoo Lee**, Jeonghun Kwak and Changhee Lee, “Characteristics of Organic Thin-Film Transistors with a Gate Dielectric Deposited with Self-Assembled Monolayer of Various Alkyl Chain Lengths,” *Nano Korea 2011*, KINTEX, Korea (Aug, 2011).

10. Donggu Lee, Seunguk Noh, Jun Young Kim, **Hyunkoo Lee**, Jeonghun Kwak, and Changhee Lee, "Temperature Dependence of Current-Voltage Characteristics of Polymer Solar Cells with MoO<sub>3</sub> and PEDOT:PSS as Hole Injection Layer," *Nano Korea 2011*, KINTEX, Korea (Aug, 2011).
11. Hyuk Ahn, Wonjun Song, **Hyunkoo Lee**, Kookheon Char, Seonghoon Lee and Changhee Lee, "Highly efficient top-emitting organic light emitting diodes with LiF/Yb bilayer as an electron injection layer," *SPIE Optics+Photonics*, San Diego, USA (Aug, 2011).
12. **Hyunkoo Lee**, Hyuk Ahn, and Changhee Lee, "Efficient inverted bottom-emission organic light-emitting diodes with ytterbium-doped electron injection layer," *The 7th International Conference on Advanced Materials and Devices*, Jeju, Korea, pp. 376 (Dec, 2011).
13. Yongwon Kwon, Myeongjin Park, **Hyunkoo Lee** and Changhee Lee, "Improvement of Efficiency of Polymer Light-Emitting Diodes using Solution-Processed Small Molecular Electron Transport Layer," *2012 MRS Spring Meeting*, Moscone West Convention Center, San Francisco, CA, J14.3 (Apr, 2012).
14. **Hyunkoo Lee**, Young Kwan Kim, and Changhee Lee, "Improved performances in phosphorescent OLEDs using solution-processed vanadium pentoxide as a hole-injection layer," *50th SID International Symposium, Seminar & Exhibition*, June. 7, Boston, USA, P.111 (Jun, 2012).

15. Hyuk Ahn, **Hyunkoo Lee**, Jungjin Yang, and Changhee Lee, “Highly efficient electron-injection layer of LiF/Yb bilayer for top-emitting OLEDs,” *50th SID International Symposium, Seminar & Exhibition*, June. 7, Boston, USA, P.112 (Jun, 2012).
16. Myeongjin Park, Hyunduck Cho, **Hyunkoo Lee**, Donggu Lee, Jaehoon Lim, Kookheon Char, Seonghun Lee, and Changhee Lee, “Efficient red, green, and blue QD-LEDs fabricated with the QD transplanting process on a common hole-transport layer,” *50th SID International Symposium, Seminar & Exhibition*, June. 7, Boston, USA, P.72 (Jun, 2012).
17. SuYeon Park, **Hyunkoo Lee**, Jungjin Yang and Changhee Lee, “Simulation of CRI and CCT for white OLEDs consisting of three different colors,” *International Conference on Science and Technology of Synthetic Metals 2012*, Atlanta, USA, July 8-13 (Jul, 2012).
18. Youngjun Ko, **Hyunkoo Lee**, Yongwon Kwon, and Changhee Lee, “Improved Efficiency of Polymer Solar Cells by Using Potassium Borohydride as an Electron Injection Layer,” *SPIE Optics+Photonics*, San Diego, USA, Aug 12-16 (Aug, 2012).
19. Yongwon Kwon, **Hyunkoo Lee** and Changhee Lee, Inverted Top-Emitting Organic Light-Emitting Diodes with MoO<sub>3</sub>/Ag/WO<sub>3</sub> Multilayer Anode, *The 12th International Meeting on Information Display*, Daegu, Korea, Aug 28-31 (Aug, 2012).

20. Youngjun Ko, **Hyunkoo Lee**, Donggu Lee, Jun Young Kim, Hyung-Jun Song, Yongwon Kwon, Jiyun Song, Ho Jung Syn, Changhee Lee, “Characteristic Analysis of Polymer Solar Cells by Using Potassium Borohydride as an Electron Injection Layer,” *Global Photovoltaic Conference 2012 (GPVC 2012) & Korea-EU International Symposium on Photovoltaics*, Nov. 19~21, 부산 벅스코, 대한민국 (Nov, 2012).
21. Donggu Lee, Jaehoon Lim, Lisa zur Borg, Myeongjin Park, **Hyunkoo Lee**, Seonghoon Lee, Kookheon Char, Rudolf Zentel and Changhee Lee, “Investigation of Hole Injection Barrier of Quantum Dot-Conducting Polymer Hybrids LEDs,” *20 회 반도체 학술대회*, 성우리조트, Korea, Feb. 4-6 (2013).
22. **Hyunkoo Lee**, Yongwon Kwon, and Changhee Lee, “Efficient and Color Stable Phosphorescent Inverted Bottom-Emission White Organic Light-Emitting Diodes,” *Sixth International Conference on Advanced Materials and Nanotechnology (AMN6)*, Auckland, New Zealand, Feb. 11-15 (2013).

## 초 록

본 논문에서, 우리는 용액공정을 이용한 산화아연 나노입자층과 이산화주석 나노입자층의 전기광학적 특성 및 이들을 전자주입층으로 사용한 역구조 배면발광 인광 유기발광다이오드의 성능에 대해 조사하였다. 이러한 금속산화물 나노입자층들은 추가적인 처리 없이 스핀코팅 방법을 사용하여 간단히 적층 할 수 있다. 그리고 이들 박막은 가시광 영역에서 투명하다. 금속산화물 나노입자층을 가진 소자는 가지고 있지 않은 소자에 비해 향상된 소자성능을 보였다. 산화아연 나노입자층을 가진 소자가 이산화주석 나노입자층 또는 sol-gel 방식으로 형성된 산화아연층을 가진 소자보다 더 좋은 성능을 보였는데, 이는 전자주입을 위한 산화아연 나노입자층의 적절한 에너지 준위와 빠른 전자이동도 때문이다. 우리는 금속산화물 나노입자층의 두께 및 전자수송층 두께에 따른 소자의 성능을 평가하고, 전자수송층 LUMO 에너지 준위에 따른 소자 성능도 비교했다. 뿐만 아니라, 우리는 소자로부터 발광되는 전계발광의 각도 의존성을 평가하고, 모든 소자가 Lambertian 발광 특성을 보임을 확인하였다.

다음으로, 우리는 삼산화 몰리브덴 ( $\text{MoO}_3$ )을 도핑한 di-[4-(N,N-ditolyl-amino)-phenyl]cyclohexane (TAPC)를 이용하여 *p* 형 도핑된 정공수송층을 개발하였다. 우리는  $\text{MoO}_3$  도핑농도에 따른 박막의

전기광학적 특성을 조사하였다. 이러한  $p$  형 도핑된 TAPC 를 백색 유기발광다이오드에 적용함으로써 우리는 소자의 구동전압을 낮추고 전력효율을 향상시켰다. 뿐만 아니라, 우리는 역구조 배면발광 유기발광다이오드에서 정공수송층의 정공 전도도와 소자 성능 사이의 관계를 연구하였다. 정공수송층의 다양한 정공 전도도를 위해  $\text{MoO}_3$  가 도핑된 TAPC (높은 정공전도도), 도핑되지 않은 TAPC (대조군), 그리고 2,9-dimethyl-4,7-diphenyl-1,10-phenanthroline (BCP)가 도핑된 TAPC 층이 사용되었다. 이러한 다양한 정공수송층을 사용하여 적색, 녹색, 그리고 청색의 삼색을 가진 역구조 배면발광 백색 유기발광다이오드를 만들었다.  $\text{MoO}_3$  가 도핑된 TAPC 층을 가진 소자는 낮은 구동전압을 보였지만, 낮은 효율을 보인 반면, BCP 가 도핑된 TAPC 층을 가진 소자는 높은 효율을 보였으나 구동전압이 증가했다. BCP 가 도핑된 TAPC 층을 가진 소자는 광학적 광추출 기술이나  $n$  형 도핑 방법 없이 역구조 백색 유기발광다이오드에 발표된 값들 중 가장 높은 외부양자효율을 보였다. 이 결과는 고효율을 위해서는 전자-정공 균형이 매우 중요하고 고성능 역구조 유기발광다이오드를 위해서는 향상된 전자 주입이 필요함을 나타낸다.

마지막으로, 우리는 공통 적색층을 가진 녹색 및 청색 유기발광다이오드의 성능을 조사하였다. 호스트 물질과 적색 색소 물질의 HOMO 에너지 준위의 차이가 소자의 성능에 영향을 주었다.

호스트와 적색 색소의 HOMO 에너지 준위 차이에 따라 공통 적색층을 삽입한 소자의 구동전압은 공통 적색층을 삽입하지 않은 소자에 비해 비슷하거나 증가했다. 그러나, 소자의 효율과 색상은 공통 적색층 삽입 여부와 상관없이 거의 변화가 없었다. 호스트와 적색 색소의 HOMO 에너지 준위 차이가 작을수록 공통 적색층 삽입에 따른 전류 및 구동전압의 변화가 작았다. 뿐만 아니라, 우리는 공통 적색층을 적용하여 녹색 및 청색 역구조 배면발광 유기발광다이오드를 만들었다. 역구조 소자의 전기광학적 특성 경향은 정구조 소자의 경우와 비슷했다. 특히, 역구조 소자에서는 공통 적색층을 삽입함으로써 전자-정공 균형이 향상되어 소자의 효율이 증가하였다.

결론적으로, 우리는 전자주입층으로써의 금속산화물 나노입자와  $p$  형 도핑된 정공수송층을 사용하여 전자와 홀 주입을 각각 향상시켰다. 향상된 전하 주입은 역구조 배면발광 유기발광다이오드의 구동전압을 낮추고 양자효율을 증가시켰다. 우리는 또한 정공수송층의 전도도 조절을 통해 전자-정공 균형을 증가시킬 수 있었고, 결론적으로 소자의 효율을 향상시킬 수 있음을 확인하였다. 우리는 공통 적색층을 사용하여 역구조 배면발광 유기발광다이오드의 외부양자효율을 증가시켰다. 뿐만 아니라, 적절한 공통 적색층의 삽입은 유기발광다이오드의 성능 변화 없이 공정 비용과 시간을 줄일 수 있다. 본 연구에서 개발된 소자 구조와

제작 방법은 효율적이고 저비용의 광전자 소자를 실현하는데 도움이 될 것으로 기대된다.

주요어: 유기발광다이오드, OLED, 역구조, 나노입자, p 형 도핑, 공통 적색층

학 번: 2009-30207